ISSN 1028-8546

Volume XXIII, Number 3
Section: En
October, 2017

Azerbaijan Journal of Physics

Fizika

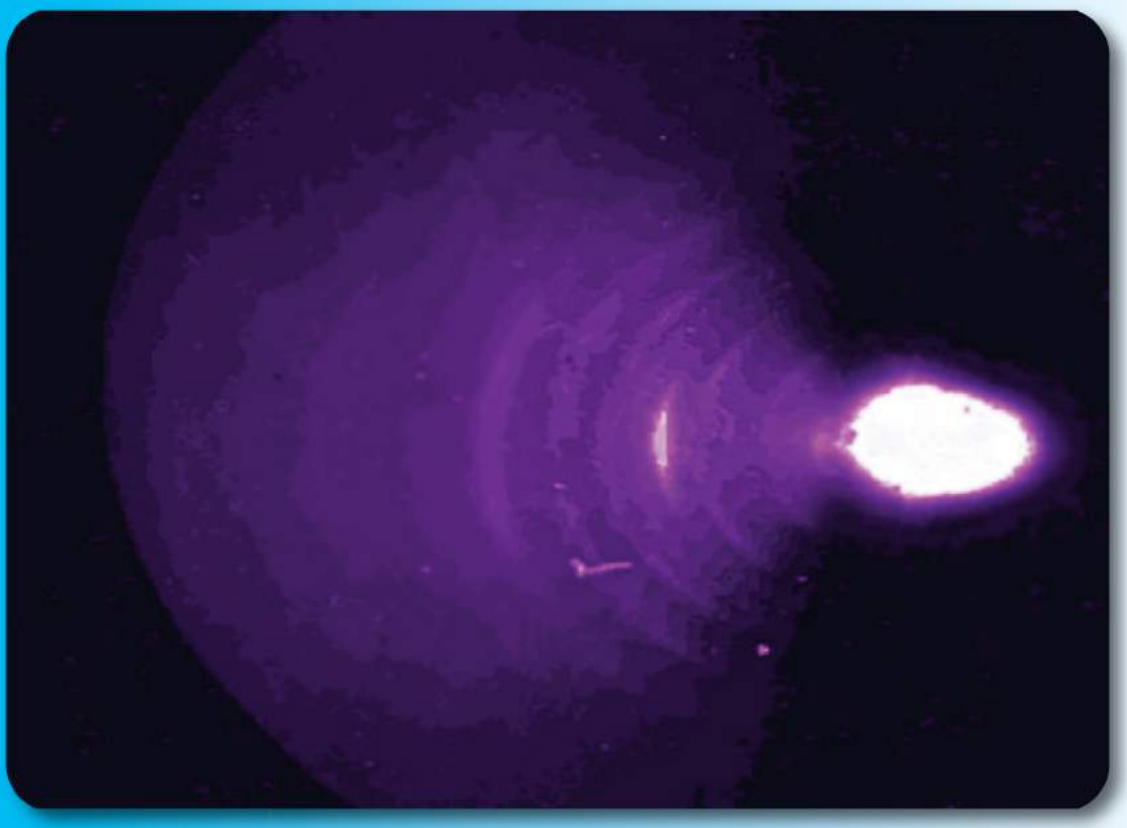

www.physics.gov.az

G.M. Abdullayev Institute of Physics
Azerbaijan National Academy of Sciences
Department of Physical, Mathematical and Technical Sciences

Published from 1995
Ministry of Press and Information
of Azerbaijan Republic,
Registration number 402, 16.04.1997

ISSN 1028-8546
vol. XXIII, Number 03, 2017
Series: En

Azerbaijan Journal of Physics

FIZIKA

G.M.Abdullayev Institute of Physics
Azerbaijan National Academy of Sciences
Department of Physical, Mathematical and Technical Sciences

PUBLISHING OFFICE

131 H.Javid ave, AZ-1143, Baku
ANAS, G.M.Abdullayev Institute of Physics

Tel.: (99412) 539-51-63, 539-32-23
Fax: (99412) 537-22-92
E-mail: jophphysics@gmail.com
Internet: www.physics.gov.az

It is authorized for printing:

Published at "**SƏRQ-QƏRB**"
17 Ashug Alessger str., Baku
Typographer : Aziz Gulaliyev

Sent for printing on: __.__. 201_
Printing approved on: __.__. 201_
Physical binding:_____
Number of copies:_____200
Order:_____

POLARIZED EFFECTS IN La DOPED $TlInS_2$ LAYERED SEMICONDUCTOR-I: DEEP LEVEL DEFECTS AND PYROCURRENTS CHARACTERIZATION

M.Yu. SEYIDOV[1, 2 *], F.A. MIKAILZADE[1, 2], A.P. ODRINSKY[3], T.G. MAMMADOV[2], V.B. ALIYEVA[2], S.S. BABAYEV[2], A.I. NAJAFOV[2]

[1]Department of Physics, Gebze Technical University, 41400, Gebze, Kocaeli, Turkey
[2] Institute of Physics of NAS of Azerbaijan, H.Javid av., 33, AZ-1143, Baku, Azerbaijan
[3] Institute of Technical Acoustics, National Academy of Sciences of Belarus, Lyudnikov av. 13, Vitebsk 210717, Belarus

Lanthanum - doped high quality $TlInS_2$ ferroelectric - semiconductors were characterized by photo - induced current transient spectroscopy (PICTS). Different impurity centers are resolved and identified. Analyses of the experimental date were performed in order to determine the characteristic parameters of the extrinsic and intrinsic defects. The energies and capturing cross section of deep traps were obtained by using the heating rate method. The observed changes of the pyroelectric response of $TlInS_2$:La crystal near the phase transition points are interpreted as a result of self - polarization of the crystal due to internal electric field of charged defects. The influence of deep level defects in pyroelectric response of $TlInS_2$:La has been revealed for the first time.

Keywords: ferroelectric phase transitions; incommensurate phase; dielectric hysteresis loops; double dielectric loops.
PACS: 77.22.-d**;**77.22. Ej;77.70.+a; 77.80.-e

*Corresponding author. Address: Department of Physics, Gebze Technical University, Gebze, 41400, Kocaeli, Turkey. Tel.: +90 262 605 1329; fax: +90 262 653 8490 , E-mail address: ***smirhasan@gyte.edu.tr*** (MH.Yu.Seyidov).

1. INTRODUCTION

Defects in semiconductor crystals significantly modify almost all physical properties of these materials. It is also well known that impurities and defects strongly influence on the ferroelectric phase transitions in crystals. The influence of defects on phase transitions is one of the hot topics in the context of modern studies of ferroelectrics. Special attention was attracted to ferroelectric - semiconductor materials, especially due to their suitability for many device applications. In ferroelectric - semiconductors, the influence of defects on material properties clearly manifests itself during external perturbation. External fields can create the own dipole moment in centrosymmetric defects or readily orientate chaotically arranged of the locally frozen dipole moment of defects in ferroelectric – semiconductors [1].

The ternary ferroelectric - semiconductor $TlInS_2$ belongs to the well - known class of $A^{III}B^{III}C_2^{VI}$ chalcogenides with layered crystal structures. At room temperature the crystal structure of $TlInS_2$ belongs to monoclinic syngony and has space symmetry group of C_{2h}^6 [2]. On cooling $TlInS_2$ undergoes successive phase transitions to incommensurate (IC) and commensurate (C) ferroelectric phases at the temperatures T_i~ 216 K and T_c~200 K, respectively [3, 4]. The phase transition from the paraelectric phase at T_i~ 216 K is a second order one and the appeared IC phase exists in the temperature range between ~ 200 and ~ 216 K, which is characterized by an incommensurately modulated displacement wave in the crystal structure of $TlInS_2$ [5 - 7].

The incommensurately modulated displacement wave in $TlInS_2$ crystal is formed due to atom displacements in the (110) symmetry plane and is directed along [001] axis. Displaced atoms don't exactly repeat themselves in neighboring elementary cells, so the three dimensional translational invariance of $TlInS_2$ crystal is broken. The IC - modulation period is near 4 unit cells of the initial crystal structure of $TlInS_2$ [2, 8].

On decreasing the temperature the IC - modulation wave vector varies continuously and locks into the commensurate value of $\frac{1}{4}\boldsymbol{c}$ at T_c [2, 8]. This corresponds to quadrupling of the unit cell volume along the direction perpendicular to the layers. The phase transition from IC to the ferroelectric phase is of the first order. At T_c, or Curie point, there is a structural change to a low temperature polar ferroelectric phase.

In the vicinity of the Curie point the IC - phase consists of a periodic arrangement of commensurate domains with constant phase and amplitudes of the modulation wave, which are separated by narrow domain walls, the so called discommensurations (DC or soliton like domains) [9 - 11]. Inside the DC's the phase of the incommensurately modulated displacement wave changes rapidly and local mechanical strains underlying crystal lattice are accompanied. Thus, DC's or soliton like domains can be considered as topological defects of the crystal lattice.

The most remarkable feature associated with DC's is that DC's can be pinned by impurities and other defects of the crystal structure. Native defects of the crystal or dopant could be strongly destroys the processes of nucleation and growth, annihilation, forward and sidewise motion of DC's [10]. Besides, topological defects can extremely affect homogeneous charge trap distribution in crystals creating an on - equilibrium internal electrical field distribution as a consequence. In this frame the synthesis and investigation of the crystals with the IC phase doped by electrically active impurities is of great importance.

This paper presents the results of investigations of the polarized effects in lanthanum - doped $TlInS_2$ ferroelectric – semiconductors caused by electrically

131 H.Javid ave, AZ-1143, Baku
ANAS, G.M.Abdullayev Institute of Physics
E-mail: jophphysics@gmail.com

active La - defects. Pyroelectric properties of $TlInS_2$:La were investigated by measuring a short circuit current through the sample on varying the temperature. Prior to the pyroelectric current measurements, $TlInS_2$:La was poled by applied electric field. It was revealed that the polarization field in $TlInS_2$:La can be concentrated among charged defects localized on the surface of the sample and its volume as well, creating surface or bulk internal electric fields originating from this intrinsic dipoles.

This fact motivated photo - induced current transient spectroscopy (PICTS) investigations of $TlInS_2$:La for the detection and identification of charged traps responsible for polarized effects in material under investigations. A clear correlation between pyroelectric properties of $TlInS_2$:La and PICTS analyses is evident from the results.

2. EXPERIMENTAL METHODS

$TlInS_2$ polycrystals were synthesized from high purity elements (at least 99.999%) taken in stoichiometric proportions. Single crystals of $TlInS_2$ were grown using Bridgman – Stockbarger method from a melt of the starting materials sealed in evacuated (10^{-5} Torr) silica tubes with a tip at the bottom, without any intentional doping. The inner wall of the ampoule was coated with a thin layer of carbon to rule out any reaction with the container. To prevent the ampoule from exploding, it was heated in a temperature gradient furnace. The doping was performed by adding the corresponding weighted portion of lanthanum to a cell with the preliminarily synthesized $TlInS_2$ compound. The resulting undoped and La - doped ingots were yellow in color showed good optical quality and were easily split along the cleavage planes with mirror like surface. No further polishing and cleaning treatments were required.

The chemical composition of the studied crystals was determined by the energy dispersive spectroscopic analysis using a scanning electron microscope. The energy dispersive X - ray analysis performed at room temperature confirmed the formula composition of the undoped and La - doped samples. This analysis also demonstrated that the doped $TlInS_2$ sample is enriched in the lanthanum impurity with a content of ~ 0.37 at %. Moreover, it was revealed that $TlInS_2$:La sample involved an insignificant percentage of background impurities, such as carbon, oxygen and silicon.

The investigated $TlInS_2$:La sample had the form of the plates with ~ 2 mm thick and ~ 20 mm^2 surface.

The sample was mounted on a cold finger placed inside Janis closed - cycle helium cryostat equipped with glass windows for optical measurements. A control sensor (diode DT - 470) and a resistive control heater were mounted under the base and used to control the temperature with an accuracy of less than ~ 0.1K by using a Lake Shore - 340 auto tuning temperature controller. All of the measurements were made in a running vacuum of the order of 10^{-3} mbar.

The dark current measurement was carried out in the temperature interval 80 – 300K during heating at a constant rate of ~1 K/min in darkness under a voltage of ~10 V. The measurements were performed using a high precision digital Keithley - 485 pico - ammeter.

The pyroelectric properties were studied by direct method in short - circuited regime under a linear temperature variation. The temperature was changed with the different hearting rates, typically between 15 and 20 K/min. High precision digital Keithley - 617 programmable electrometer was used to measure the pyrocurrent and the data were collected by a PC. The surfaces of La doped $TlInS_2$ sample were covered by silver paste to form electrodes oriented perpendicularly to the polar axis. Two thin wire terminals were used as external leads to make the sample free and to avoid any stress on it. Prior to the measurements, sample was subjected to electrical poling by cooling in darkness in the presence of the polarizing electric field ~ 5 kV/cm using high voltage power supply. The poling field was applied to sample within a certain temperature range.

PICTS measurements were carried out in the temperature range of 77 – 300K. Under the PICTS investigation the photo - excitation of the samples was carried out by monochromatic light with photon energy less than the width of forbidden gap ($h\nu < E_g$) at homogeneity excitation of crystal surface. We used the photon energies in range of $h\nu$ = 2.30 - 2.43 eV that corresponds to the maximum of the electrical response. The illumination light was perpendicular to the layers plane of the crystal. The photon flux density was $10^{14} cm^{-2} s^{-1}$ at the sample surface. The frequency of the illumination pulse was 20 Hz with light to dark duration in the ratio of $1/5$. The duration of excitation pulse was 30 ms.

The sample was mounted inside the nitrogenium cryostat with grade quartz optical window. The sample was placed on massive aluminum holder close to temperature sensor Hell - 700.

The photoresponse measurements were performed along the layers plane of the crystal. The ohmic indium contacts were soldered to the lateral sides of the samples. The measuring circuit was typical for photocurrent investigation. A bias voltage up to 50 V was applied to the sample. The experimental setup was described in detail elsewhere [12].

The registration of the photoresponse decays was performed over the temperature range of 78 – 330K in a temperature step of 1K upon slow heating of the previously cooled sample. The heating rate of the sample was 2 K / min.

The home - made data acquisition system with preliminary processing and registration of transient data on a personal computer was used [12].

Pointwise accumulation and averaging were carried out across 64 realizations of photoresponse decay containing 2000 samplings located at a fixed time interval Δt = 62 μs. Taking into account the ferroelectric nature of the crystal the photo response transient was monitored and recorded also.

A conventional DLTS technique was applied for the photoresponse transient analysis using a rectangular lock - in weighting function. The data registration allowed the characterization of relaxation times in the range from 0.2 to 20 ms with regard to the selected conditions.

3. EXPERIMENTAL RESULTS

3.1 - Photoinduced Current Transient Spectroscopy Measurements

PICTS is a suitable technique for studying the trapping levels (activation energy, capture cross section or emission coefficient) in high - resistive or semi - insulating semiconductor materials which cannot be measured with capacitance based deep level transient spectroscopy [13]. The principle of PICTS technique is based on measurements of time dependent photocurrent due to carrier emission from deep levels [14, 15]. The light excitation is used to creation of defects filling by non equilibrium charge carriers. An intrinsic light creates electron – hole pairs in a small region underneath the ohmic contacts. If a bias field is applied, electrons or holes are transported through a small distance into the bulk and trapped by empty centers. When the illumination is switched off, thermal detrapping from the deep levels occurs with a characteristic time constant that is determined by the thermal emission rate.

On investigating the semiconductors with ferroelectric properties it is important that light impulse with suitable photon energies can change the defect's charge state without significant perturbation of crystal domain structure. The last case take place under applying the conventional DLTS technique, where the defects are filled by using electrical field or current pulses that is not applicable for our study.

The temperature dependence of the thermal emission rate can be used for recognizing of a defects recharging according to:

$$e_t(T) = \sigma_t T^2 B exp\left(-{}^{E_t}/_{kT}\right), \qquad (1)$$

where σ_t is the effective capture cross - section; B is a constant for the studied material, E_t is the activation energy of the recharging defect, k is Boltzmann constant, T is the absolute temperature.

From equation (1) the activation energy E_t and capture cross-section σ_t can be extracted with applying a conventional procedures of DLTS analyze [13] to the set of registered data.

3.2. Characterization of Traps.

Fig. 1 shows typical PICTS spectra of $TlInS_2$:La crystals. The well structured part of the spectra with clearly distinguishable maxima is observed in the temperature region below the temperatures of phase transition in $TlInS_2$ crystals [16].

The shift of the temperature position of the maximum in the set of spectra corresponding to various characteristic relaxation times is good compared to the thermal activation of emission from the defects that filled under photo excitation. It should be noted that the PICTS technique gives no way of determine the sign of the carriers trapped by centers (electrons or holes). We proposed that the detected traps are of acceptor type since traps of majority carriers are mostly observed in high - resistively semiconductors with wide band gap [17].

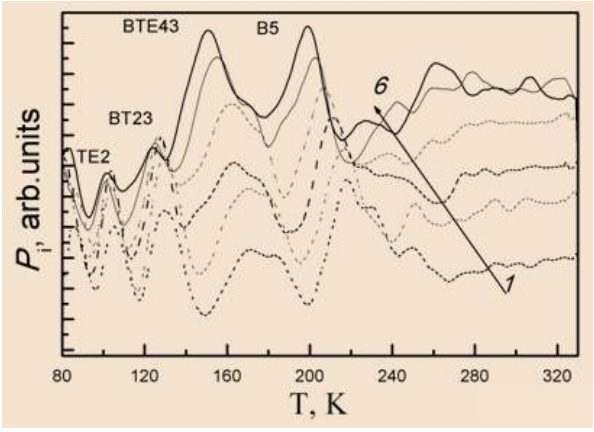

Fig. 1. - PICTS spectra of $TlInS_2$:La corresponding to the thermal emission rate: 1) 2200 s^{-1}; 2) 1350 s^{-1}; 3) 770 s^{-1}; 4) 408 s^{-1}; 5) 213 s^{-1}; 6) 108 s^{-1}; 7) 54 s^{-1}. The spectra are normalized to the height of the maximal peak and shifted along Y –axis/

The temperature dependence of the thermal emission rate for the detected traps is shown in Fig. 2.

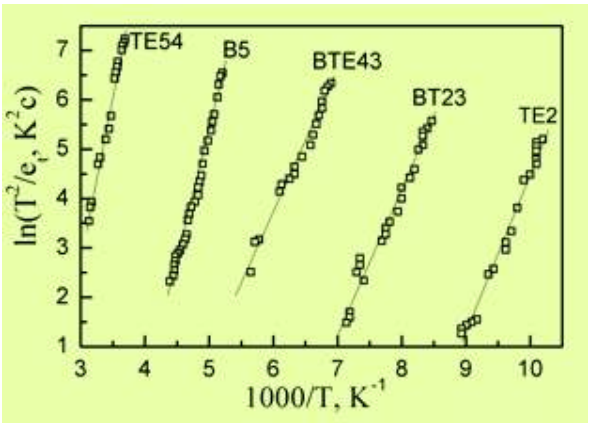

Fig. 2. - Rate of charge carrier emission from deep level traps in $TlInS_2$:La as function of temperature by taking into account T^2 correction. Solid lines represent the fitting to experimental data.

Trapping parameters of $TlInS_2$:La crystal.

Table 1.

Defect	$\Delta_0 T$ K	E_t eV	σ_t cm^2
TE2	98 - 115	0.2	2.2×10^{-14}
BT23	115 - 135	0.25	5.7×10^{-13}
BTE43	145 - 181	0.3	5.0×10^{-15}
B5	190 - 229	0.29	4.9×10^{-16}
TE54	270 - 320	0.57	1.0×10^{-13}

From the best fitting of plot of $ln({}^{e_t}/_{T^2})$ versus ${}^{10^3}/_T$, the thermal activation energies and capture cross - sections of defects were calculated. Under the σ_t evaluation the effective masses of hole was set to 0.14 m_0 according to the work [18.]. The obtained values of the thermal activation energy of the traps E_t and effective capture cross section σ_t are listed in Table 1. The

temperature ranges $\Delta_0 T$ for detected signals from traps are presented in the first column of the Table 1 also.

This observed defects recharging is well comparable with the results of preliminary studies of differently doped $TlInS_2$ crystals [19]. Thus, the same labels are used for defect notification in this investigation.

3.3. Polarization Effects in $TlInS_2$:La.

Fig. 3 (a – d) exhibits the temperature variation of pyroelectric current (I_p) in lanthanum doped $TlInS_2$ single crystal registered after sample poling under different electric fields in cooling. The pyroelectric current generated in $TlInS_2$:La was measured at various heating rates.

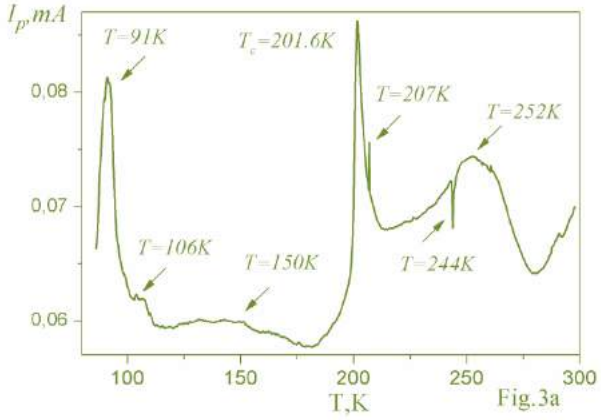

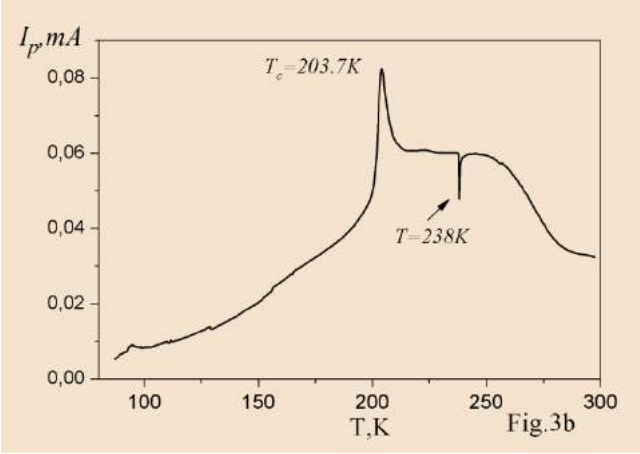

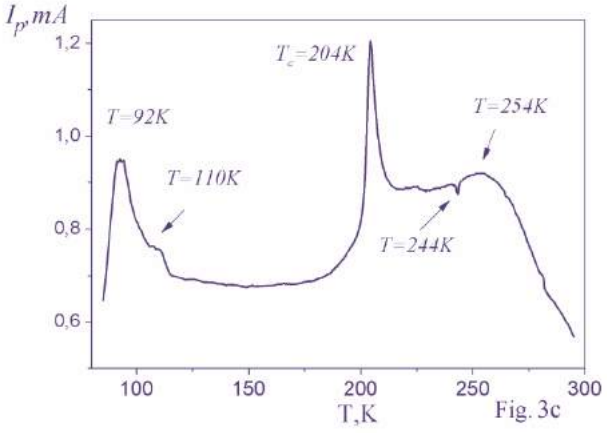

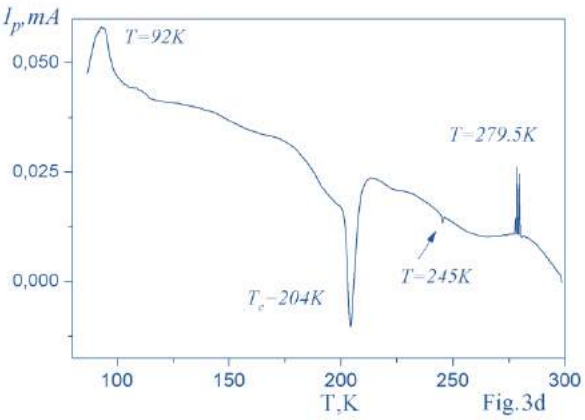

Fig. 3. - Temperature dependence of the pyroelectric current generated in $TlInS_2$:La after sample poling under different conditions.
a – The sample was polled by external electric bias field 300 V/cm in cooling from room temperature to ~ 77K. Pyroelectric current generated in $TlInS_2$:La was measured at constant heating rate 15 K / min.
b - The sample was polled by external electric bias field 300 V/cm in cooling from room temperature to ~ 77K. Pyroelectric current generated in $TlInS_2$:La was measured at constant heating rate 20 K / min.
c - The sample was polled by external electric bias field 5 kV/cm in cooling from room temperature to ~ 77K. Pyroelectric current generated in $TlInS_2$:La was measured at constant heating rate 20 K / min.
d – Same as in Fig. 3 (c), but the pyrocurrent response was measured after the short - circuit of electrodes at ~ 77K.

Fig. 1 (a) shows a shape of the pyrocurrent response of $TlInS_2$:La after poling the sample by applied dc field of about 300 V/cm. The sample was cooled from room temperature to 77K under the poling field. A constant heating rate was 15 K / min. The pyrocurrent response in Fig. 3 (a) can be divided in two parts. The low temperature part contains three peaks: one is sharp and is located around ~ 91 K; and smeared peaks in the vicinity of ~ 106 and 150K. In the high temperature part several peaks were observed at temperatures between T_c and ~250K. The sharp peak in the pyroelectric current response at T_c is connected to increase of the spontaneous polarization at Curie point of the C - phase transition. Additionally, there is remarkable peak at in the pyroelectric current response of La doped $TlInS_2$ inside the IC – phase at ~ 207 K.

According to [5, 19], the phase transition around 207K is due to intrinsic defects interacting with the IC – modulation, because defects can introduce some perturbations leading to new topological arrangement of DC's. The peaks occurring above T_i are not considered as corresponding to phase transitions. They may be due to some thermally depolarization phenomena associated with some charged defects. Note that pyroelectric current signal changes the sign at ~ 244K.

A measurement of the pyroelectric current plotted in Figs. 3 (b) and (c) was performed under the similar initial conditions but some differences were observed. The temperature dependence of I_p measured after sample poling under applied bias field ~ 300 V/cm is shown in

Fig. 3 (b). A constant heating rate was 20 K / min. It can be seen from Fig. 3 (b), that no peaks formed in the curve $I_p(T)$ in the low temperature region. The pyroelectric current maximum near Curie point is observed at T_c ~ 207.3K and sharp peak with negative sign is recorded at ~ 240K. Broad peak at ~ 250K in Fig. 3 (a) become more smeared as heating rate is increased.

Fig. 3 (c) shows the temperature dependence of pyroelectric current response of $TlInS_2$:La after sample poling under bias field ~ 5 kV/cm. The rate of temperature change was 20 K / min. It is clear that the sample previously poled under external field ~ 5 kV/cm shows significantly higher pyroelectric signal. It was revealed that the pyroelectric current values obtained from $TlInS_2$:La sample poled under ***dc*** field ~ 5 kV/cm increase by about ~ 20 times and remains qualitatively similar to that in Fig. 3 (a). One can see from the Fig. 3 (c) that the pyroelectric signal is strongly dependent on the degree of polarization state of previously poled sample.

It is known that, the pyroelectric signal in ferroelectric - semiconductors may be caused by temporary residual space charges accumulated in the trap levels in the regions directly adjacent to the electrodes (surface electric field) as well as in bulk of the crystal after initial polarization of $TlInS_2$:La in bias field [20 - 22]. An internal electric field formed in the bulk of crystal has the direction opposite to the direction of applied polarity. Using the short - circuited technique, we can separate the pyroelectric response from internal electric fields built in the bulk of $TlInS_2$:La crystal. After poling of the sample under ***dc*** electric field of ~ 5 kV/cm upon cooling from room temperature to 77K two electrodes were then short - circuited for ~ 10 min in order to eliminate the internal electric field frozen at the crystal surface. The pyroelectric current was measured on heating of crystal from 77 to 300K with the same heating rate 20 K/min. The results are plotted in Fig. 3 (d). From this figure, it can be seen that the pyroelectric signal has a maximum at about 92 K and decreases in magnitude with temperature increasing. On the approaching to the Curie point, the pyroelectric signal rapidly decreases and becomes negative forming peak at about T_c ~ 204K. Fig. 3 (d) shows reversed peak at ~ 245 K and pronounced normal peak at ~ 280K.

Fig. 4 shows the temperature dependence of the pyroelectric current for the $TlInS_2$:La specimen after poling for 10 minutes by dc electric field ~ 5 kV/cm at 78K. It is seen from Figs. 3,*a* and 4 that there is no principal difference in the temperature behavior of the pyrocurrent signal for $TlInS_2$:La sample subjected to different polarization conditions. The only difference is two normal peaks at ~ 157 and ~ 194 K. It is remarkable that similar picks on $I_p(T)$ curve was observed after crystal poling under bias electric field applied to sample in different temperature ranges. Possibly, the appearance of these additional picks is conditioned by the additional polarization induced by the crystal poling processing.

Fig. 5 demonstrates the evolution of the pyroelectric current of $TlInS_2$:La as a function of the temperature for sample poled in the temperature region ~ 210 – 300K using a ***dc*** electric field of ~ 5kV/cm. The temperatures of some peaks are indicated in this Figure. Rather unexpectedly we do not see any peaks at $T < T_c$. It can be observed that the temperature of the maximum of the pyroelectric current corresponding to T_c is a little lower in comparison with previous data.

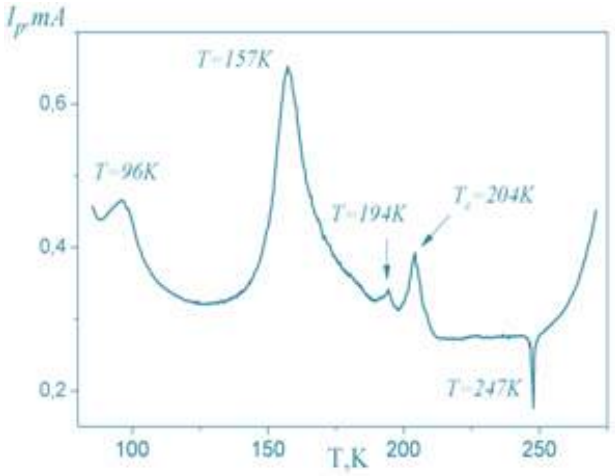

Fig. 4. - Temperature dependence of the pyroelectric current generated in $TlInS_2$:La after sample poling at ~ 77 K by dc electric field ~ 5 kV/cm. The heating rate was 20 K / min.

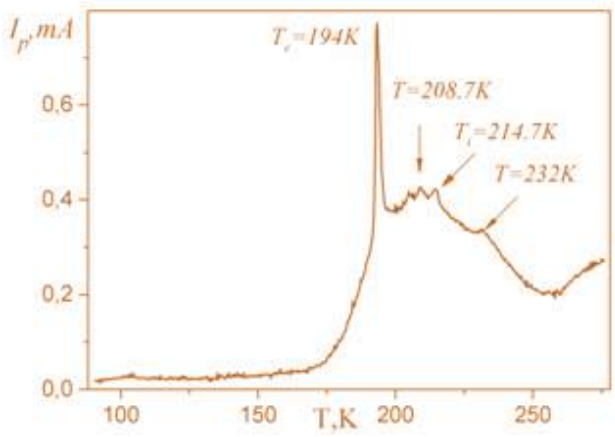

Fig. 5. - Temperature dependence of the pyrocurrent generated in $TlInS_2$:La after sample poling by dc electric field ~ 5 kV/cm in the temperature region ~ 210 – 300K in cooling . The heating rate was 20 K / min.

As indicated by the arrows in Fig. 5, small peaks are well defined at ~ 208 and ~ 215K corresponding to anomalies at T_i and inside the IC – phase [23]. However, it needs to be pointed out that average polarization inside IC – phase must be zero because the IC - phase possesses the center of inversion symmetry [10, 11]. This means that during poling process the external electric field does not induce aligned polarization inside IC – phase.

These results support the existence of coupling between a bias electric field the aligned polarization inside IC – phase. We assume that defects make major contributions in retained polarization of the IC – phase. These results will be discussed later together with other experimental results.

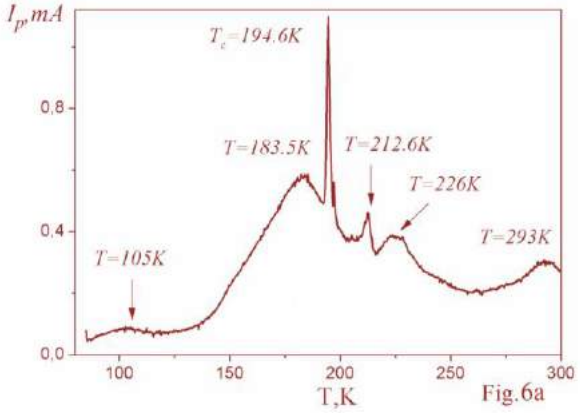

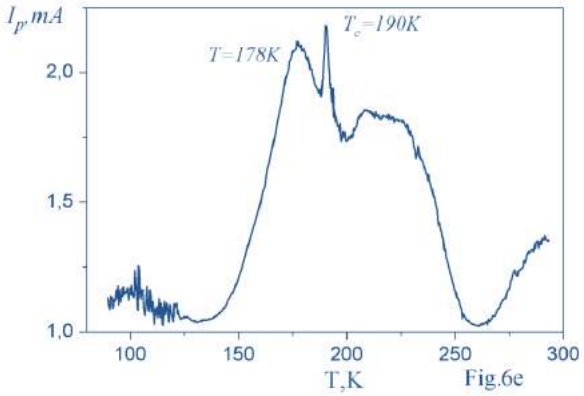

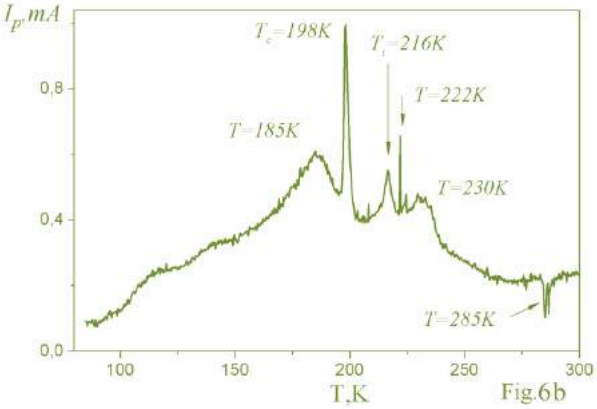

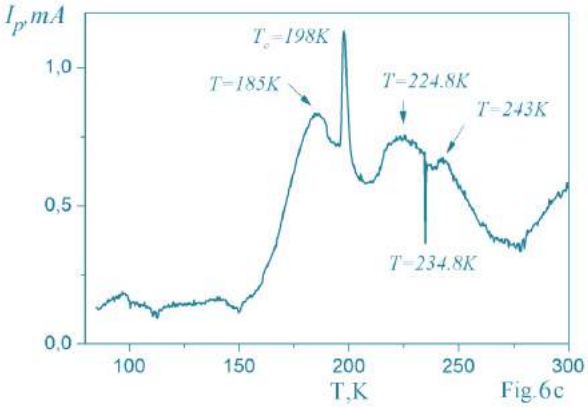

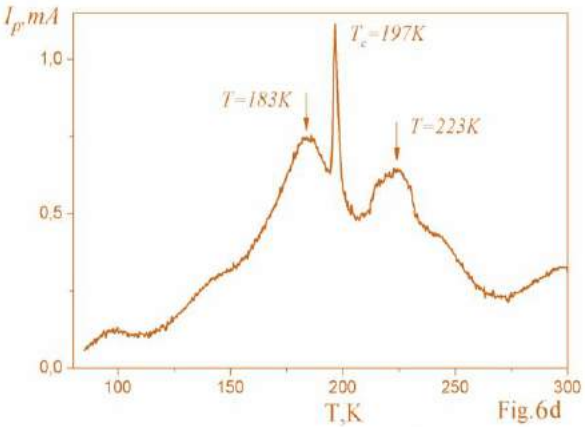

Fig. 6. - Same as Fig. 5, but the sample was polled in the temperature region: (a) –~ 180 – 300 K; (b) –~ 180 – 290 K; (c) - ~ 180 – 260 K; (d) - ~ 180 – 240 K; (e) - ~ 180 – 220 K.

Fig. 6a – Fig. 6e shows a set of typical curves of the pyroelectric current as a function of the temperature for $TlInS_2$:La recorded after sample poling in different temperature regions. The poling temperature regions were chosen in accordance with temperature intervals of traps activation TE54 and B5 (Table 1). As in previous measurements the sample was polarized by ~ 5 kV/cm electric field. The temperature was raised from liquid nitrogen to room temperature at a constant rate of ~ 20 K/min.

All curves in Fig. 6 show different features with respect to poling regimes. An anomalous maximum of $I_p(T)$ at the Curie transition point is well seen in all curves. The temperature of maxima of $I_p(T)$ at T_c is observed in the region between 190 and 198 K. The shape of $I_p(T)$ curve in Fig. 6 is significantly different. As a rule, two main peaks, a weak peak at low temperature ~ 100K and a strong one at ~ 180 K are observed in all curves. Besides, additional anomalies of $I_p(T)$ with modified shape and temperature positions are recorded in all curves in the 220 – 240K range.

Fig. 7 (a and b) demonstrates the pyroelectric current versus temperature for $TlInS_2$:La sample previously poled in the presence of dc electric field at ~ 5 kV/cm on cooling in the temperature region ~ 220 - 80K and ~ 190 - 80K, respectively. The pyroelectric current across the sample was measured at the same heating rate ~ 20 K/min. These temperature regions correlate with the range of thermal activation of deep level defects B2, BTE43, BT23 and TE2 (see Table 1).

One can see that the temperature range of the thermal activation of deep level defect B2 involves the temperature region of a sequence of structural phase transitions in $TlInS_2$:La. Therefore one must keep this in mind in dealing with influence of defects on structural phase transitions in $TlInS_2$:La. The point here is that defect B2 must get a dipole moment after poling by electric field. This brings to appearance of quasi - static internal electric field originated from charged B2 defect and existing into crystals in the temperature interval 190 – 220 K. This field, which is parallel to the poling external electric field is responsible for the polarization properties

of $TlInS_2$:La inside the IC – phase during the pyrocurrent measurement. In the presence of a strong internal electric field due to B2 defect, the pyroelectric response in Fig. 7 (a) exhibits unusual behavior at ~ 185K. A sharp peak with opposite direction was also observed at T_i. This result can be interpreted on the base of assumption that space charge accumulated by B2 defect gives rise to a strong imprint internal electric field where two opposite polarization orientations is favored regardless of the sign of the external field.

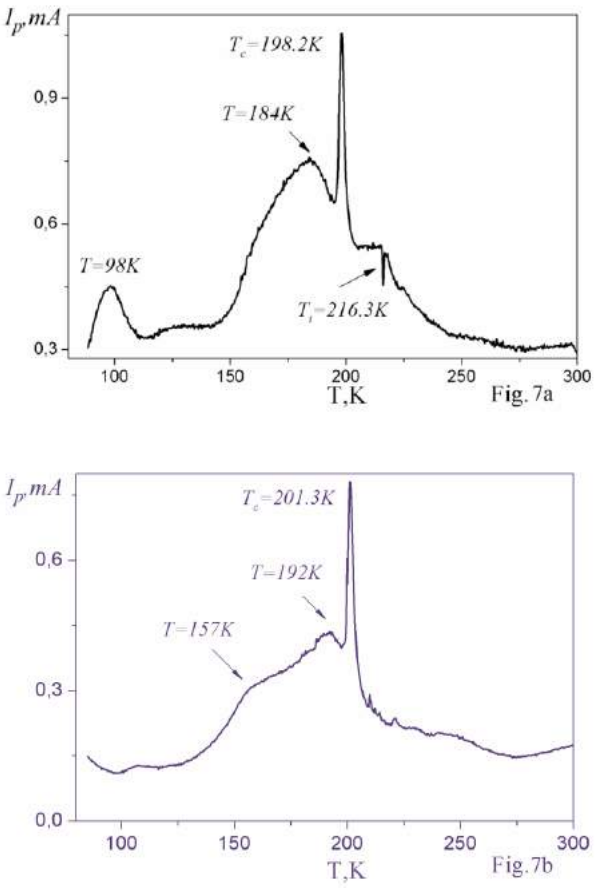

Fig. 7. - Same as Fig. 5, but the sample was polled in the temperature region: (a) – ~ 80 – 220 K; (b) – ~ 80 – 190 K.

Additionally, it is evident that, various electrically activated defects in $TlInS_2$:La lead to different internal electric fields in crystal. Such situations are illustrated in Fig. 7 (a and b). If charge carriers are captured by other trap levels, for example, BTE43, BT23 and TE2 by the crystal poling the internal electric field originated from this ionizated does not contribute to the pyrocurrent signal recorded inside the IC – phase.

The electric activation of BTE43, BT23 and TE2 defects in $TlInS_2$:La and the formation of the imprint internal electric field from charge carriers trapped by this defects should be tested by pyroelectric current measurements after sample poling in the presence of dc electric field ~ 5 kV/cm on cooling in the different temperature renges inside the commensurate ferroelectric phase ~ 170 – 80 K, ~ 140 – 80 and ~ 120 – 80 K, respectively (see Fig. 8 and Table 1). The pyroelectric current measurement in Figs.8 was performed at the same heating rate ~ 20 K/min.

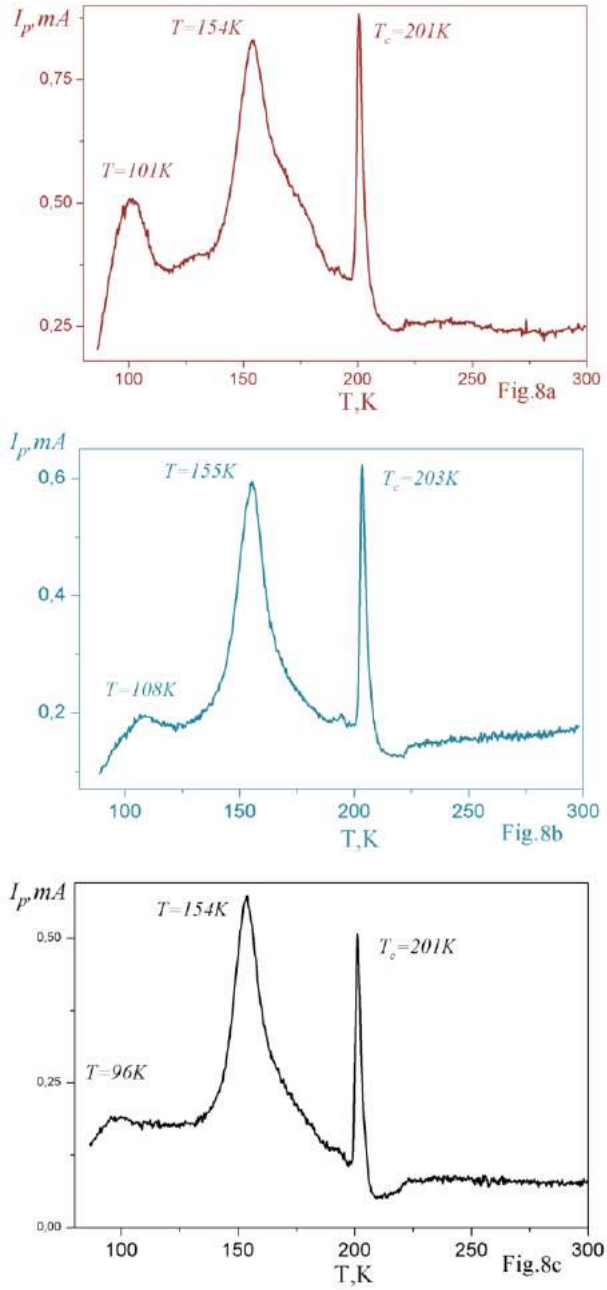

Fig. 8. - Same as Fig. 5, but the sample was polled in the temperature region: (a) – ~ 80 – 170 K; (b) – ~ 80 – 140 K; (c) - ~ 80 – 120 K.

As it can be seen from Fig. 8 similar changes of the pyroelectric current have been found. A broad maximum at ~ 155 K in $I_p(T)$ after electric polarization of $TlInS_2$:La in different temperature intervals is appeared. The magnitude of a broad peak at ~ 155 K is comparable with a sharp peak of $I_p(T)$ at the Curie temperature. Pyroelectric current around a broad anomalous at ~ 155K and near T_c has the same direction, while external field at the Curie point during the poling process has not been applied to the sample. The latter may be due to the presence of strong internal field into the sample. The origin of this internal field and a broad anomalous at ~

155K can be originated from BTE43 defects. Defects labeled as BTE43 can be activated by poling La dipoles because this type of defect is not discerned with PICTS in undoped $TlInS_2$ single crystal [16].

Experimental results in Fig. 8 demonstrate that no observable change in the pyroelectric current signal is observed at the temperatures 115 – 135K, which correspond to thermal activation of BT23 deep level defect. However, the anomalous in the pyroelectric current signal at ~ 100 K have been found in all curves of Fig. 8 and in the most curves of Figs. 3 - 7. The TE2 deep level center with a high ionization cross section (see Table 1) activated by external electric field is believed to be the source of the pyrocurrent signal observed in this material.

3.4 - Dark current measurement of $TlInS_2$:La.

From the results discussed so far one may conclude that there is a correlation between temperature ranges of the thermal activation of deep level defects revealed by using PICTS technique and polarization properties of the La doped $TlInS_2$ single crystal. These deep level traps must induce electronic states in the band gap of $TlInS_2$:La which have to alter significantly the dark current properties of $TlInS_2$:La crystal.

The results of dark current measurement in the temperature range of 77 – 300 K obtained by standard two - probe method are shown in Fig. 9. The same contacts were used to study the temperature behavior of the resistance. The measurements were performed with a heating rate of ~ 2 K/min. The dark conductivity of the $TlInS_2$:La crystal exhibits activation type temperature dependence.

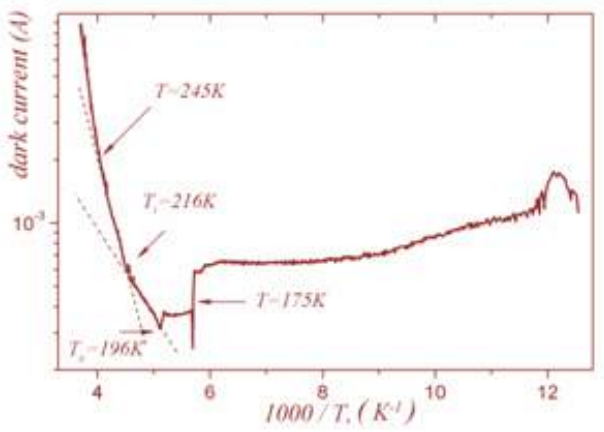

Fig. 9. - Dark current versus temperature for $TlInS_2$:La shown in the Arrhenius plot. The measurement was carried out in the direction parallel to the layer at the bias of ~ 10V. The heating rate is 2 K min^{-1}.

A large step – like thermal anomaly in the temperature dependence of dark current was observed at ~ 175K. On the other side, a small thermal anomaly was registered at Curie temperature of the phase transition at about 196 K. A characteristic feature of anomaly at ~ 175K and at Curie point is that the dark current to resemble, in general, the behaviour of the pyrocurrent observed under the action of crystal poling.

Additionally, changes of the dark current curve slope were observed at T_i and near ~ 245K. It can be interpreted by the change of the carrier activation energy at the phase transition. Three distinct temperature regions 196 – 216K, 216 – 245K and 245 – 300K with different activation energies 0.25, 0.58 and 0.72 eV, respectively, were found. The activation energies of impurities in these temperature regions were calculated from Arrhenius relationship, which are in good agreement with PICTS dates. Therefore, it can be concluded that the dark current throughout the $TlInS_2$:La sample inside the IC – phase and above the IC – phase transition point T_i is considerably controlled by B5 and TE54 intrinsic defect centers. From these results, it can safely be assumed that B5 deep level center clearly reflects the structural changes in the temperature region of the existence of an intermediate IC – phase in $TlInS_2$:La. The dark current at low temperatures is not due to excitations of carriers from TE2 and BT23 native deep levels as well as BTE43 defect center belonging to La – impurity because this process requires much larger energy of activation.

4. DISCUSSION OF EXPERIMENTAL RESULTS

Thus, trap levels labeled TE2, BT23, BTE43, B5 and TE54 have been detected in PICTS measurements in $TlInS_2$:La. Arrhenius plots of $ln\left(e_t/T^2\right)$ versus $1000/T$ allowed the determination of the activation energies of defects, Fig. 2. The trap parameters extracted from the Arrhenius plot are summarized in Table 1.

The dominant deep level trap is B5 has the activation energy of 0.3 eV from the top of the valence band. It is a native defect since it has also been observed in PICTS measurements of trapping levels in undoped $TlInS_2$ [16]. The thermal activation region of B5 - localized level (variation of charge density on this trapping level) is correlated with phase transitions region in $TlInS_2$. In the presence of an external poled electric field, random electrical fields produced by ionized deep B5 impurities are aligned in the direction opposite to the direction of the applied electric field, and very strong internal electric field is appeared in the bulk of $TlInS_2$:La. It is a reversed electrets field according to the terminology used in [24, 25]. The pyroelectric signal of $TlInS_2$:La due to polarization of crystal in the presence of reversed bulk internal electric field is shown in Fig. 3 (d). An important attribute of macroscopic polarization of $TlInS_2$:La originated from charged B5 defects localized in the bulk of crystal is the presence of negative values of the pyroelectric current appeared during heating run near the Curie point for short - circuited sample.

The origin and nature of B5 deep trapping center is not known. However, we would like briefly to discuss the microscopic properties of the B5 defect. It can be concluded from the pyroelectric studies that B5 trapping centers are deep charged defects with frozen opposite bulk polarizations. It is well known that the defect with frozen dipole polarization may be realized as an interstitial defect in a site of sufficiently low symmetry [1]. Experimental facts indicate that the electronic properties of the B5 defects are also affected by lattice distortions observed at the phase transition points in

$TlInS_2$:La. This result can be interpreted on the base of the presence of electron - lattice interaction around the crystalline environments of B5 defect locations, whose symmetry allows to linear coupling to the soft mode of structural symmetry distortion. So, it can be expected that substantial lattice distortions in $TlInS_2$:La at phase transition points will occur in trigonal prismatic voids where Tl atoms are located [26].

The presence of the structural distortion together with the giant static dielectric constant ($\varepsilon \sim 1500$) inside the IC – phase of $TlInS_2$:La [3 – 5, 19 -23] transforms the B5 defects to the charged trap. It is well known that the ionization energy of the traps is inversely proportional to the dielectric constant of the medium. Thus, in the region of intermediate IC – phase there is collective accumulation of charged B5 deep defect centers. The internal electric field induced by electrically active B5 centers in the temperature region of 190 – 230 K is the electrets field. This built – in internal electrets field is far from being completely disappear even after a long time because discharged processes have a low speed at low temperatures. Self - polarization of $TlInS_2$:La due to B5 trapping centers produce the pyrocurrent current signal that exhibit all anomalies inherent in the $TlInS_2$:La sample in the region of phase transitions as it is shown in Figs. 5, 6 and 7 (a). Note that the poling procedure for normal ferroelectrics always requires application of a strong external electric field inside the ferroelectric phase. Self - polarization of $TlInS_2$:La occurs outside the ferroelectric phase and pretreatment of crystal under high external electric fields within the ferroelectric phase can be avoided. An internal electric field appeared in $TlInS_2$:La sample above T_c due to charged B5 deep level defects is higher than the coercive field at Curie temperature.

The defect labeled BTE43 was observed only in $TlInS_2$:La. This deep level is related to La dopant. The results allowed to suppose that the peak observed on the temperature dependence of pyroelectric current near 155 K is induced by charged BTE43 deep trapping center (see Fig. 8). It was found that the direction of internal electric field due to charged BTE43 defects is collinear to the direction of the applied poling electric field. The temperature of the pyroelectric current anomaly near 155 K induced by frozen – in internal field from BTE43 charged defects is significantly lower than the Curie point. The poling electric field can be applied to $TlInS_2$:La at temperatures below ~ 170K in order to detect the pyrocurrent anomaly due to BTE43 charged defects in the vicinity of 155K. If the sample is maintained under the external field up to the temperatures above 170K, the pyroelectric current peak at ~ 150 K is disappeared. Then, one may conclude that the frozen internal field from B5 charged defects screens (or discharges) the space charge polarization from charged BTE43 deep trapping centers. The reason of this phenomenon is not clear yet.

The peak on the temperature dependence of the pyroelectric current at temperatures ~ 90 – 100K is originated from charged TE2 deep level trap. It is a native defect with unknown origin with energy 0.2 eV and activation temperature interval of 98 – 115K. In our studies we found this level in almost all pyrocurrent measurement.

Two other defects BT23 and TE54 are native defects too. They have been clearly observed by PICTS in undoped $TlInS_2$ [16]. Due to their trap parameters, particularly the high cross sections $\sim 10^{-13} cm^2$, these levels correspond an extended defects.

A deep trapping level BT23 is very similar to TE2. Therefore it is very difficult to identify it contribution in crystal polarization from pyroelectric current measurements. Perhaps, BT23 and TE2 are native strongly compensated deep levels controlling the electronic properties of $TlInS_2$ at low temperatures, providing semi – insulating properties of this material in the low temperature range. Obviously, more clear evidence of the compensation nature of these defects and their microstructure must be obtained.

The contribution of native TE54 deep level in resistivity of $TlInS_2$:La can be easily identified at room temperatures from dark current measurements. $TlInS_2$ is identified as $\boldsymbol{p}$ – type semiconductor material. Therefore, TE54 is deep level acceptor. The experimental data do not allow any conclusion to be drawn about the nature of this center because of the lack of information about the crystal defects in $TlInS_2$ material.

5. CONCLUSIONS

Thus, the polarization phenomena in La – doped $TlInS_2$ ferroelectric – semiconductor due to internal electric fields originated from charged deep level trapping centers are investigated. The $TlInS_2$:La was also characterized and studied by PITCS measurements at different temperatures. Using PITCS measurements, five deep levels in $TlInS_2$:La were observed. Four of them were identified as native defects because they have been observed in undoped $TlInS_2$ also. The trap BTE43 corresponds to the La dopant. The activation energy of all deep centers and their cross sections were determined. The contribution of each charged defect in polarized properties of $TlInS_2$:La was identified from the pyroelectric current studies. It was shown that the anomaly of the pyroelectric current detected above the Curie point is attributed to the self – polarization of $TlInS_2$:La under internal electric field formed from charged B5 native deep level. The IC – phase as a medium with giant and stable dielectric constant can be responsible for the ionization of B5 deep defect because the thermal activation region of B5 defect coincides with the temperature region of existence of the intermediate IC – phase in $TlInS_2$.

It is assumed that the anomaly of pyroelectric signal near 155K is related to BTE43 deep level. Pyroelectric signals of previously poled at $T < 170$K $TlInS_2$:La crystal could not be observed near 155K since this temperature is below enough than the Curie temperature.

ACKNOWLEDGMENTS

The authors acknowledge support through the bilateral programme RFBR (14 – 02 – 91374 CT_a) – TUBITAK (No. 213M524).

[1] *A.P. Levanyuk, A.S. Sigov*, Defects and Structural Phase Transitions (Ferroelectricity & Related Phenomena) (Gordon & Breach Science Publishers Ltd, 1988).
[2] *S. Kashida, Y. Kobayashi*, J. Phys.: Condens. Matter 11, 1027 (1999).
[3] *F.A. Mikailov, E. Başaran, T.G. Mammadov, M.Yu. Seyidov and E. Şentürk*, Physica B 334, 13 (2003).
[4] *S.S. Babaev, E. Basaran, T.G. Mammadov, F.A. Mikailov, F.M. Salehli, M.-H.Yu. Seyidov, R.A. Suleymanov*, J.Phys.: Condens. Matter 17, 1985 (2005).
[5] *R.A. Suleimanov, M.Yu. Seidov, F.M. Salaev and F. A. Mikailov*, Phys.Solid State 35, 177 (1993).
[6] *B.R. Gadzhiev, M.Yu. Seidov and V.R. Abdurakhmanov*, Phys. Solid State, 38, 1 (1996).
[7] *B.R. Gadzhiev, M.Yu. Seidov and V.R. Abdurakhmanov*, Low Temp. Physics 21, 950 (1995).
[8] *S.B. Vakhrushev, V.V. Zhdanov, B.E. Kvyatkovskii, N.M. Okuneva, K.R. Allakhverdiev, R.A. Aliev and R.M. Sardarly*, JETP Lett. 39, 291 (1984).
[9] *H.Z. Cummins*, Physics Reports 185, 211 (1990).
[10] Incommensurate Phases in Dielectrics, Part 1, Fundamentals, edited by *R. Blinc and A.P. Levanyuk* (North-Holland, Amsterdam, 1986).
[11] Incommensurate Phases in Dielectrics, Part II, Materials, edited by *R. Blinc and A P. Levanyuk* (North-Holland, Amsterdam, 1986).
[12] *A.P. Odrinskii*, Semiconductors 38, 298 (2004).
[13] *D. V. Lang*, J. Appl. Phys. 45, 3023 (1974).
[14] *Ch. Hurter, M. Boilou, A. Mitonneau and D. Bois*, Appl. Phys. Lett. 32, 821 (1978).
[15] *O. Yoshie, and M. Kamihara*, Jap. J. Appl. Phys. 22, 621 (1983).
[16] *M.-H.Yu. Seyidov, R.A. Suleymanov, A.P. Odrinsky, A.I. Nadjafov, T.G. Mammadov, and E.G. Samadli*, Jap. J. Appl. Phys. 50, 05FC08 (2011).
[17] *J.C. Balland, J.P. Zielinger, C. Noguet, and M. Tapiero*, J. Phys. D 19, 57 (1986).
[18] *A.F. Qasrawi, N.M. Gasanly*, Cryst. Res. Technol. 39, 439 (2004).
[19] *K.R. Allakhverdiev, N.D. Akhmed-zade, T.G. Mamedov, T.S. Mamedov, M.Yu. Seidov*, Low Temperature Physics 26, 56 (2000).
[20] *M.-H.Yu. Seyidov, R.A. Suleymanov, S.S. Babayev, T.G. Mammadov, A.I. Nadjafov, and G.M. Sharifov*, Phys. Solid State 51, 264 (2009).
[21] *M.-H. Yu. Seyidov, R. A. Suleymanov, S. S. Babaev, T. G. Mammadov, and G. M. Sharifov*, Phys. Solid State 51, 568 (2008).
[22] *M.-H.Yu. Seyidov, R.A. Suleymanov, and F. Salehli*, JAP 108, 024111 (2010).
[23] *M.-H.Yu. Seyidov, R. A. Suleymanov, and F. Salehli*, Phys. Solid State 51, 2513 (2009).
[24] *V.M. Fridkin*, Ferroelectrics – Semiconductors (Consultants Bureau, New York, 1980).
[25] *V.M. Fridkin*, Photoferroelectrics (Springer, Berlin, 1979).
[26] *W. Henkel, H.D. Hochheimer, C. Carlone, A. Werner, S. Ves, and H.G. v. Schnering.* Phys. Rev. B 26, 3211 (1982).

Recevied: 12.06.2017

POLARIZED EFFECTS IN La DOPED $TlInS_2$ LAYERED SEMICONDUCTOR-II: POLARIZATION SWITCHING IN UNDOPED AND La - DOPED $TlInS_2$ FERROELECTRIC - SEMICONDUCTORS

M.Yu. SEYIDOV[1, 2], F.A. MIKAILZADE[1, 2], V.B. ALIYEVA[2], T.G. MAMMADOV[2], G.M. SHARIFOV[2], V.P. ALIYEV[2]

[1] *Department of Physics, Gebze Technical University, 41400, Gebze, Kocaeli, Turkey*
[2] *Institute of Physics Azerbaijan National Academy of Sciences, AZ - 1143 Baku, Azerbaijan*

Dielectric hysteresis loops of pure and lanthanum doped $TlInS_2$ ferroelectric – semiconductors were studied at the frequency 50 Hz for different temperatures below the Curie temperature (T_c). It has been revealed that, without any poling procedure, pure $TlInS_2$ exhibits normal single hysteresis loops at $T < T_c$. After electric field - cooled treatment of $TlInS_2$ the shape of hysteresis loops was strongly affected by corresponding charged deep level defects which were previously activated during the poling process. As a result, an additional defect polarization state from space charges accumulated on the intrinsic deep level defects has been revealed in pure $TlInS_2$ at the temperatures belowT_c. Besides, unusual multiple hysteresis loops were observed in La doped $TlInS_2$ at $T < T_c$ after application of different external perturbations (electric field, exposition and memory effect) to the sample. Measurements of the hysteresis loops in $TlInS_2$:La revealed the slim single, double and even triple polarization – electric field ($P – E$) hysteresis loops. This intriguing phenomenon is attributed to the domain pinning by photo – and electrically active La – impurity centers. The temperature variation of double - hysteresis loop was also investigated. Due to the heat elimination of the random local defect polar moments, the double – hysteresis loops were transformed into a normal single hysteresis loops on increasing the temperature.

Keywords: ferroelectric phase transitions; incommensurate phase; dielectric hysteresis loops; double dielectric loops.
PACS: 77.22.-d**;**77.22. Ej;77.70.+a; 77.80.-e

*Corresponding author. Address: Department of Physics, Gebze Technical University, Gebze, 41400, Kocaeli, Turkey. Tel.: +90 262 605 1329; fax: +90 262 653 8490
E-mail address: ***smirhasan@gtu.edu.tr*** (M-H.Yu.Seyidov).

1. INTRODUCTION

In a broad family of ferroelectric crystals, which possess spontaneous polarization reoriented by the electric field [1, 2], there is one which has played an especially important role in the physics of ferroelectricity in general. It is the ternary thallium indium disulphide - $TlInS_2$, the ferroelectric – semiconductor crystal with layered structure with monoclinic space group C_{2h}^6 at room temperature. The intensive research of various physical properties of this crystal during the past recent 40 years has led to an understanding of the mechanism of structural phase transitions in the materials which contain ferroelectric and semiconductor properties simultaneously as well as to new ideas related with the combination of the two branches: semiconductor physics and ferroelectricity (see Ref. [3 - 8] and references therein).

$TlInS_2$ is a well-known $\boldsymbol{p}$ - type semiconductor crystal [9, 10]. Its indirect and direct band gaps at 300K are: ~ 2.26 eV and ~ 2.34 eV correspondingly [11]. It has a high photoconductivity [12] in the visible range of light. The semiconductor characteristics of $TlInS_2$ single crystals studied by using optical and electrical measurements have been explained details in the literature. Additionally, the results of thermally stimulated current, photoluminescence and thermoluminescence investigations of $TlInS_2$ have been also presented recently in numerous works [13].

It has been revealed that, on cooling $TlInS_2$ undergoes structural phase transition (PT) from a paraelectric phase to incommensurably modulated phase at the temperature T_i ~ 216K. On further cooling, the wave vector of the incommensurate modulation changes until it locks into a commensurate wave vector at the Curie temperature T_c ~ 200K, and the structure transforms to a commensurate ferroelectric one [3 - 8]. In spite of a great number of studies, generally there isn't a clear picture for understanding the structure and origin of ferroelectricity in $TlInS_2$ at the temperatures below T_c.

Generally, ferroelectrics are known as insulating materials. The switchable electric polarization of these materials generally arises from a polar structural distortion of a high - symmetry reference structure. The ternary thallium chalcogenides $TlInS_2$ and $TlGaSe_2$ are ferroelectric - semiconductors with the same layered structure which undergoes phase transitions on decreasing the temperature from a high - temperature paraelectric phase to a low - temperature ferroelectric phase passing through an intermediate incommensurate phase. These ferroelectric – semiconductors have optical band - gap in the visible range and therefore have advantages of over other conventional ferroelectric materials. The possibility of electric field control of optical and electronic properties of $TlInS_2$ and $TlGaSe_2$ via the switchable polarization is of particular interest. For example, in a doped $TlInS_2$ ferroelectric - semiconductor, the polarization originated from a polar structural distortion can couple with internal electric field of charged deep – level defects. So, application of the electric field can be used directly to manipulate the electric polarization of $TlInS_2$ ferroelectric – semiconductor and thus control any semiconductor properties of $TlInS_2$ that are coupled to the polarization. This can give rise to multiple polarization states, switchable diode effect and bulk photovoltaic effect in which absorption of light by $TlInS_2$ material generates an asymmetric carrier distribution resulting in photocurrent.

131 H.Javid ave, AZ-1143, Baku
ANAS, G.M.Abdullayev Institute of Physics
E-mail: jophphysics@gmail.com

All these effects can lead to further technological applications of $TlInS_2$ improper ferroelectric – semiconductor in nonvolatile information storage, energy conversion and optoelectronics.

In recent years, several investigations have been performed for studying the relationship between ferroelectric domain walls and charged deep level defects in ferroelectric – semiconductors [5, 14 - 19]. It has been suggested that the polarization switching in ferroelectrics – semiconductors is strongly affected by the presence of charged deep level defects. Intrinsic defects in $TlInS_2$ have been the subject of intense investigation recently. In [16 - 20] photo - induced current transient spectroscopy (PICTS) has been applied to get more insight into spectra of intrinsic defects in high - resistive undoped $TlInS_2$ and La doped $TlInS_2$ crystals. Several deep level traps in wide band gap of undoped $TlInS_2$ and $TlInS_2$:La were obtained from transient properties of charge induced by photo – excitations [16 - 20]. In this paper, the important role of native charged deep level defects on the polarization switching properties of undoped $TlInS_2$ and $TlInS_2$: La was investigated through ferroelectric hysteresis loops measurements.

Lanthanum has been known as a kind of the photo - and electrically - active type of rare earth impurity center in semiconductor materials. Depending on the experimental conditions, La – dopant can be spontaneously ionized. In our previous works the change of dielectric properties of $TlInS_2$ induced by lanthanum dopant has been extensively studied [5, 14, 21]. Strong variations of the dielectric permittivity (ε) of $TlInS_2$: La within incommensurate (INC) phase has been found from measurements under external perturbations: the bias electric field and photoactive illumination. It has been obtained that the shape of the $\Delta\varepsilon(T)/\varepsilon(T)$ curves (here $\Delta\varepsilon$ is the difference between dielectric permittivity values measured under an external bias electric field and without it, and $\varepsilon(T)$ is the reference curve for $TlInS_2$: La without external perturbations) looks like the deviations of dielectric permittivity related with the memory effects observed inside INC - phase of undoped $TlInS_2$ crystal [5, 14, 21].

Note that the memory effect (ME) - "memorizing" the prehistory of a sample is the main characteristic of the INC - modulated systems A memory effect in incommensurate phases has been investigated in insulating materials and some charge – density wave compounds [22 - 26]. It has been revealed that after annealing for several hours at an annealing temperature T_{ann} within the INC - phase, the sample exhibits different physical properties from those in a non - annealed sample. The most remarkable property of the memory effect is that an incommensurate wave vector is unchangeable in several degrees around T_{ann} in heating and subsequent cooling processes.

Generally, this effect is caused by formation of defect density wave (DDW) as a result of rearranging of mobile defects on annealing of the crystal within INC - phase. The interaction between mobile defects included in a sample and INC - modulation gives rise to an ordered pattern of defects that is the frozen DDW. When the defects are mobile and the modulation is static, the diffusion of the defects occurs. The frozen DDW can seriously pin the INC – modulation of structure [22 - 26]. When the modulation is pinned by defects which are randomly distributed along its direction, the formation of metastable states as well as the existence of plateaus in the temperature dependence of the modulation wave vector and some other physical parameters can be revealed.

ME appears as a kink in the temperature dependence of the permittivity when the crystal is kept at the temperature within the INC phase during several hours. The usual temperature behavior of the permittivity is recovered on heating away from the annealing temperature. An inflection point of the kink is centered at an annealing temperature in the permittivity curve. Since the relaxation time of the mobile defects determined by their diffusion mobility considerably exceeds the time required for the measurements, it is possible to "conserve" the DDW in the temperature region outside the INC phase. If the sample is cooled below T_{ann} the DDW is pinned to the modulation wave on subsequent heating at T_{ann}, and this effect is called ME.

However, it is no unambiguous theoretical description of ME phenomenon existing in $TlInS_2$ in the frame of the general model. Recently we extended the DDW model and proposed a more complex model of charged intrinsic impurities interacting with INC wave in $TlInS_2$ [5, 14, 21]. In other words, the self - polarized DDW in $TlInS_2$ (and in $TlGaSe_2$ also) is created by charged defects leading to the internal bias field that can affect the all physical properties of crystal greatly [5, 14, 21].

Thus, another purpose of this work was to investigate the presence of the ME on ferroelectric hysteresis loops in $TlInS_2$:La. Additionally, we report the effect of the illumination of crystal by photoactive light with various wavelengths on P - E dependences in $TlInS_2$: La. A further was to study the influence of preliminary application of ***dc*** electric field to the crystal during cooling at different temperature ranges on P - E dependence of $TlInS_2$: La was also the aim of this work.

2. EXPERIMENTAL PROCEDURE

The technology of $TlInS_2$ crystals is presently developed well enough and its application does not possess great difficulties [9, 10]. The crystals of best quality are produced when combining crystal synthesis and growth processes within a single technological cycle. Polycrystalline $TlInS_2$ was synthesized from high purity (at least 99.999%) elements taken in stoichiometric proportions by chemical reaction in quartz ampoules. Normally, the synthesis of ~ 40 gr. of $TlInS_2$ compound takes place during 6 – 8 hours. Single crystals of $TlInS_2$ were grown using Bridgman – Stockbarger method from the melt of the starting materials sealed in evacuated ~ 10^{-5} Torr silica tubes with a tip at the bottom without any intentional doping. Single crystal growing was realized by slow melt crystallization technique using directional motion of sharp temperature gradient with the amount of 15K per millimetre in the vertical resistance furnace. Silica - glass tube with polycrystalline $TlInS_2$ was annealed above the melting point (~ 1035K) of the $TlInS_2$ compounds at about 5 – 10K and held at this

temperature for 2 - 3 days. The melt is mixed by vibration to gain homogeneity and intensify reacting parent substances. After this treatment the melt was moved from the hot side of zone furnace at ~ 1035K to the cold side at ~ 673K at the speed of 0.1 mm/h. In the cold zone, the crystal cooled down slowly within 2 – 3 weeks. The obtained crystal has a layered structure with glossy orange color and was easily split along the cleavage plane with a smooth - mirror surface.

The doping was performed by adding the corresponding weighted portion of lanthanum to the cell with the preliminarily synthesized $TlInS_2$ compound. The resulting La - doped ingot was yellow in color, showed good optical quality and its freshly cleaved surfaces were mirror like. The chemical composition of the crystals was determined by energy dispersive analysis using a scanning electron microscope. This analysis demonstrated that the doped $TlInS_2$ sample is enriched by the lanthanum impurity with a content of ~ 0.37 at. %.

Sample for the electrical measurements was cut from the single crystal ingot parallel to [010] axis. The active area and thickness of the sample were about 4.5 mm^2 and 2.5 mm respectively. Methyl alcohol solution was used as cleaner for crystal faces. High - purity silver paste was coated on two opposite faces of the sample as electrodes. A thin copper wire was attached to the electrodes by silver paste drop for the measuring circuit. The sample was placed inside a close - cycle helium optical cryostat equipped with a temperature stabilization system with an accuracy of ~ 0.05K. The temperature was measured and controlled by a Lake Shore - 340 model temperature controller. The temperature was measured by a DT - 470 silicon diode sensor. The experimental setup was fully computer controlled.

The ferroelectric hysteresis loops property of the $TlInS_2$: La capacitor was investigated by using computer controlled modified Sawyer - Tower circuit with voltage pulse of triangular wave type and with phase compensation of the linear part of the polarization and leakage. The polarization of the sample was derived from the charges of a capacitor connected in series with the sample. The electric field was applied to a sample by a high - voltage ***ac*** amplifier with the input sinusoidal signal with a frequency of 50 Hz from a signal generator. A computer program was used for displaying hysteresis loop traces from the monitor of the digital high resolution multi - channel oscilloscope at fixed temperatures.

A 100 W power halogen lamp with different filters was used for optical illumination of the sample in the P - E hysteresis loop measurements under illumination. With the purpose of achieving the greatest possible orientation of the polar La impurities the ***dc*** electric field about 20 kV/cm was applied to the sample in a direction parallel to the ***b*** – axis (the ***b*** – axis lies in the plane of layers). The sample was preliminarily cooled under dc electrical field from the room temperature down to ~ 13 K, and then the high voltage was removed from the sample and P - E hysteresis loop measurements at different temperatures were performed.

The measurements of ME were performed according to the following procedure. Firstly, the sample was cooled down to ~ 13K and then it was heated and annealed at T_{ann} ~ 210K within the INC - phase for ~ 5 hours. Then the sample was cooled again to ~ 80K and the P - E hysteresis loops at different temperatures were registered on the heating regime.

3. EXPERIMENTAL RESULTS

3.1. P - E hysteresis loops measurements in undoped $TlInS_2$

Fig.1 illustrates the typical bipolar ferroelectric P – E hysteresis loops for undoped $TlInS_2$ sample measured at 170K which is far below T_c. Hysteresis loops were plotted up to 40 kV/cm and with 50 Hz frequency. A clear reverse polarization hysteresis loops behavior was observed. The normal single hysteresis loop at $T \leq T_c$ provides additional evidence for the conclusion about the presence of the ferroelectric phase in $TlInS_2$ below the Curie temperature. The area inside the loop clearly increases with temperature decreasing indicating that the existence of the loop is due to the stable polarization.

As it is seen from the figure, the observed P – E hysteresis curve is slightly asymmetric both along the field and polarization axes. It has been observed that the negative coercive field is slightly higher than the positive one. There could be more than one contributor causing this asymmetry in the hysteresis behavior. We do not consider the reasons associated with different electrode materials of different work functions or different densities of interface states [27, 28], because of the same silver paste electrodes were deposited into opposite parallel cleavage planes for electrical measurements. The asymmetric shape of the hysteresis loop could also be attributed to the space charge layer near the one of the electrodes [27, 28], which decreases the electric field within the ferroelectrics. The width of space charge layer varies with the direction of polarization and therefore different near different electrodes. Hence the hysteresis loop is slightly asymmetric in shape [27, 28]. Additionally, a small discrepancy between the positive and negative values of remnant polarization (P_r) was observed.

The reason for choosing of the temperature 170 K as the reference point for study of ferroelectric switching in $TlInS_2$ is intentional. A change of shape in the hysteresis loops in the vicinity of phase transitions at T_i and T_c has been demonstrated in our previous work [3, 4, 6]. The P - E hysteresis loops of $TlInS_2$ modified from a single loops to a triple - like loops when the temperature increase above 170K up to T_c ~ 200K. The polarization - electric field hysteresis loops measurements were still possible above T_c at the temperatures up to ~ 204K. The triple - like P – E hysteresis loops have been gradually transformed to the double hysteresis loops in this temperature region. $TlInS_2$ possessed the normal single square – like hysteresis loops only at $T \leq$ 170K. The mechanism of such abnormal temperature transformation of the shape of ferroelectric hysteresis loops near the PT – points in $TlInS_2$ was discussed in [3, 4, 6].

The origin of the asymmetric hysteresis behavior in P – E plots of $TlInS_2$ is still not clear. However, it is known that asymmetric character of the hysteresis loops in ferroic materials originates from the internal fields [29]. It is also known that $TlInS_2$ is p - type semiconductor in which the acceptor impurities create deep - trapped levels with high relaxation time constants

[15 - 21]. The space charges trapped in these deep – levels generate the so-called built-in polarization, which is almost not sensitive to ferroelectric phase transition and ferroelectric (switchable) polarization that becomes spontaneous below the phase transition temperature T_c.

On the other hand, the second origin of the asymmetric $P – E$ hysteresis loops is an asymmetric space - charge distributions in metal - $TlInS_2$ interfaces. The ferroelectric hysteresis loop is also affected by the presence of these space charge regions so that $P – E$ hysteresis loops may be asymmetrically changed as in the case of built - in polarization from charged deep level traps.

The space charge effect on the ferroelectric hysteresis loops can be understood by the presence of a displacement current (I_d). When an external voltage in the form of triangular wave type is applied to the ferroelectric the I_d dynamics is given as [30, 31]:

$$I_d = \frac{d(CV)}{dt} = V(t)\frac{dC(t)}{dt} + C(t)\frac{dV(t)}{dt}, \qquad (1)$$

where C – is the capacitance of the metal – ferroelectric - semiconductor crystal interface(s) and $V(t)$– is added to the contact external voltage. For semiconductor - ferroelectric crystals the contribution of capacitance variation $V(dC/dt)$ on the displacement current is much stronger than that due to the voltage variation$C(dV/dt)$. Therefore, $I_d \approx V(dC/dt)$. The capacitance can vary due to the formation of space charges at the metal - ferroelectric - semiconductor interface(s). Moreover, the space – charge densities at metal – ferroelectric - semiconductor interface(s) is dependent of the external voltage amplitude.

3.2. Native deep defect levels in undoped $TlInS_2$ and $TlInS_2$: La

Sub – band gap PICTS analysis of the deep trap levels in undoped $TlInS_2$ revealed the existence of five major traps. In the PICTS spectra a deep defect level labeled as TE2 at $E_t = 0.16$ eV was detected. TE2 is activated in the temperature region $\Delta T = 93 – 110$K and has the capture cross – section $\sigma = 6.9 \times 10^{-15} cm^2$ [15-21]. A similar trap was found with PICTS measurements of $TlInS_2$: La ($E_t = 0.17\ eV,\ \Delta T = 96 - 108\ K,\ \sigma = 2.2 \times 10^{-14} cm^2$) [15 - 21]. It is worth noting that the PICTS method does not determine the trap sign i.e., it is a majority or minority carrier trap. Therefore, it is hard to state if the measured activation energy E_t has to be calculated from the valence or the conduction band. To properly identify the level, one has to relate the PICTS results to other trap characterization methods. This is why we do not specify either the native deep acceptors or donors which are related to deep level defects detected using the PICTS – method in $TlInS_2$.

The other deep level defect determined by PICTS experiments in undoped $TlInS_2$ (labeled as BT23) is located at $E_t = 0.25\ eV$. BT23 and activated in the temperature region $\Delta T = 115 – 135$K having the capture cross – section of $\sigma = 2.9 \times 10^{-16} cm^2$ [15 - 21]. A similar trap was also found with PICTS measurements of $TlInS_2$:La($E_t = 0.20\ eV,\ \Delta T = 113 - 135\ K,\ \sigma = 5.8 \times 10^{-13} cm^2$) [15 - 21].

The B5 deep level defect at $E_t = 0.3$ eV is the major trap which was detected in PICTS studies of undoped $TlInS_2$. The temperature of activation and the capture cross – section of this native deep level defects are $\Delta T = 190 - 240K$and $\sigma = 1.8 \times 10^{-16} cm^2$ respectively. It is worth noting that the active state of B5 - deep trap coincides with the temperature region of PT in $TlInS_2$ ternary compound [15 - 21]. A similar trap has, in fact, been found in PICTS measurements of $TlInS_2$: La ($\Delta T = 192 - 234\ K$, with the same activation energy and carrier capture – cross section as in undoped $TlInS_2$). The deep level centers marked as B7 and D_0 in undoped $TlInS_2$ [15 - 21] and TE54 in $TlInS_2$: La are responsible for the charge emission at the temperature ranges of $\Delta T = 240 - 300\ K, 316 - 330\ K$ and $268 - 307\ K$ respectively that is much above the Curie temperature. We focused our attention on the study of the native deep level centers in undoped $TlInS_2$ and $TlInS_2$: La which are ionized in the vicinity of PT and thus dramatically affected the shape of the ferroelectric hysteresis loops at the temperatures lower thanT_c. Therefore, the native deep level centers B7 and D_0 in undoped $TlInS_2$ and TE54 in $TlInS_2$: La crystals are not considered here.

PICTS measurements on $TlInS_2$: La sample showed the presence of so - called BTE43 deep level traps at $E_t = 0.29\ eV$ ($\sigma = 2.2 \times 10^{-14} cm^2$) [15 - 21]. This defect has a thermal emission interval below the Curie temperature ($\Delta T = 156 - 176\ K$). This defect is registered in $TlInS_2$: La only. It must be mentioned that, the experimental data presented in [15 - 21] do not clearly allow any conclusion about the origin of deep level center in $TlInS_2$: La observed by PICTS – method. We believe that BTE43 deep level defect is related to La – dopant.

3.3 The *P - E* hysteresis loops in electro – thermally poled $TlInS_2$

In order to investigate the contribution of each charged native deep level defect to polarization properties of $TlInS_2$ crystal we studied changes of the ferroelectric $P – E$ hysteresis loops shape after electro - thermal poling of crystal. During the electro – thermal poling process, a static external electric field of intensity ~ 20 kV/cm was applied on the samples at the temperature range where the corresponding deep level defect is thermally activated.

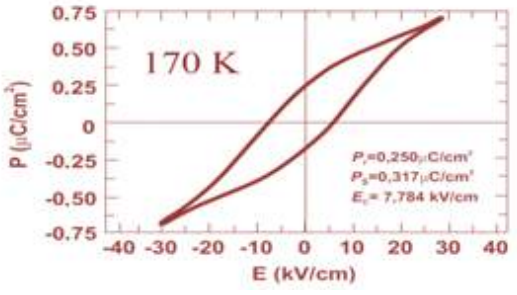

Fig. 1 - Polarization - electric field (*P - E*) hysteresis loop of unpoled $TlInS_2$ measured at a frequency of 50 Hz and at 170K. The inset shows the values of remanent polarization (P_r), saturated polarization (P_s) and a coercive field (E_c).

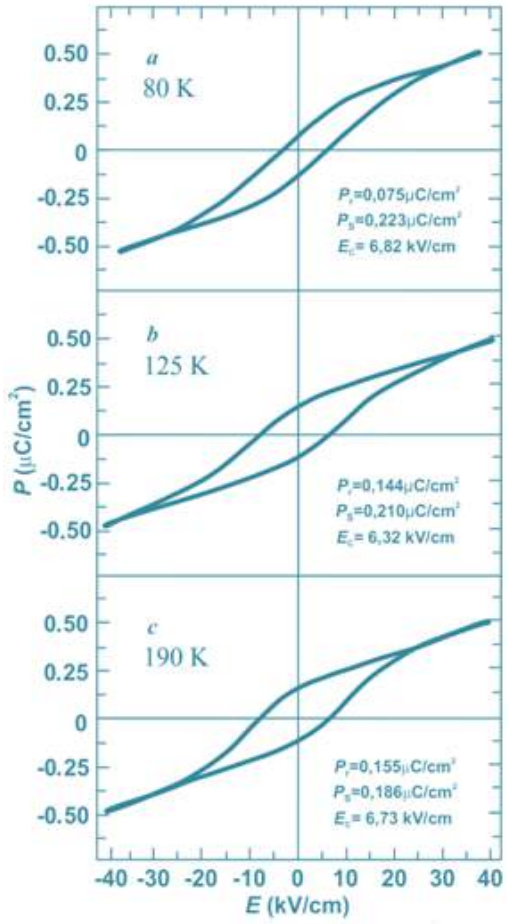

Fig. 2. Polarization versus electric field hysteresis loops of unpoled $TlInS_2$ measured at different temperatures: a) 80, b) 125, and c) 170 K after crystal polling procedure under external electric field of intensity ~20 kV/cm applied to the samples at the temperature range ~190 – 240 K, where the B5 deep level defects are thermally activated. The inset shows the values of remanent polarization (P_r), saturated polarization (P_s) and a coercive field (E_c).

A poling voltage of 1 kV is applied for a period of typically 20 ~ 30 minutes. After the poling process the applied voltage was removed. Finally, the sample is cooled down to 80K. Thus, at low temperatures the charged defects and the defect dipoles remain in their original orientation during the P - E loop measurement, and may induce the ferroelectric loops shape changing. In order to investigate the effect of poling voltage on the P – E hysteresis loops, electro – thermally poled $TlInS_2$ sample was studied at 80, 125, and 170K.

The hysteresis loops of the $TlInS_2$ with activated so – called B5 deep level defects are indicated in Fig. 2. It is seen that two P - E loops shown in Fig. 1 and 2 (a) are obviously different. The sample with charged B5 deep level defects exhibits well - defined normal single hysteresis loops with data of remnant polarization (the remnant polarization (P_r) is a non - zero polarization observed at zero electric field), saturated polarization (the saturate polarization (P_s) is equal to the polarization in the linear fit of P versus E extrapolated at zero electric field) and a coercive field (the coercive field (E_c) is a non - zero electric field observed at zero polarization) which is relatively smaller than that in Fig. 1. Accordingly, the P - E loops of $TlInS_2$ with activated B5 defects becomes more saturated on decreasing the temperature, as shown in Fig. 2 (b and c).

It is well known that hysteresis behavior of the polarization mainly originates from the ferroelectric domain switching under an external electric field. Usually, the switching process of domain in ferroelectrics suffers a certain resistance or viscous drag force [1, 32]. The resistance of viscous drag force generally increases with increasing mobile free charges, vacancies and other ion defects. If these charged defects cannot follow the applied electric field the polarization decreases [1, 32].

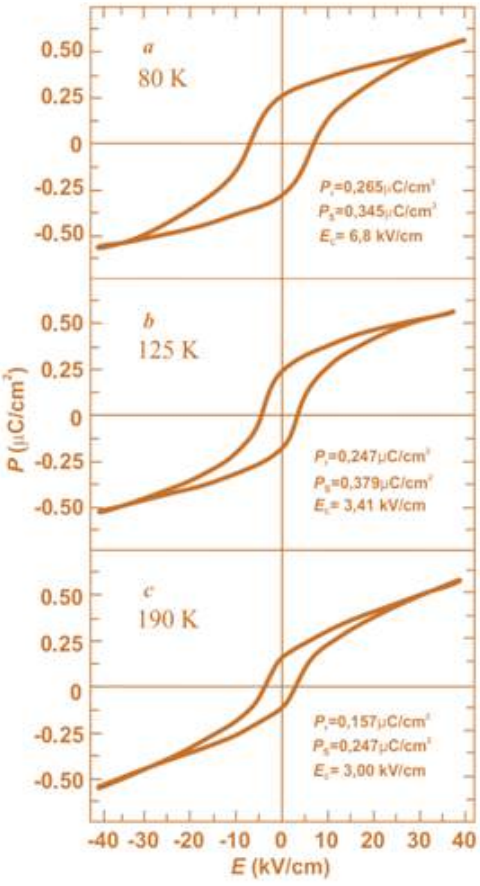

Fig. 3. Same as Fig. 2, but the sample was polled in the temperature region ~ 120 – 135 K, where the BT23 deep level defects are thermally activated. The inset shows the values of remanent polarization (P_r), saturated polarization (P_s) and a coercive field (E_c).

Figure 3 shows the polarization versus applied field response of the undoped $TlInS_2$ sample with activated BT23 native deep defects measured at 80, 125 and 170K. $TlInS_2$ exhibits rather well developed, symmetric and saturated hysteresis loop with sharp ends. Additionally, the temperature behavior of the hysteresis loops revealed that both the remanent polarization and coercive field decrease on increasing the temperature. It can be supposed that the internal electric field originated from charged BT23 native deep defects could be the reason of domain pinning which brings to reduce of P_r. The increasing domain pinning of defects implied by the decreasing E_c. The diminishing fraction of domains which

can be switched as distinct from frozen ones located in the regions where an internal electric field originated from ionized BT23 native deep level centers are imprinted might be a dominant factor of total ferroelectric polarization reduction.

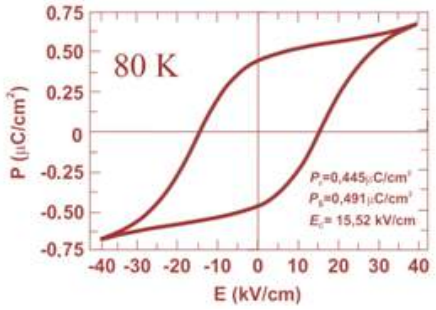

Fig. 4. $P - E$ hysteresis loop of unpoled $TlInS_2$ measured at 80 K after crystal polling under external electric field of intensity ~ 20 kV/cm applied to the samples at the temperature region ~ 95 - 110 K, where the TE2 deep level defects are thermally activated. The inset shows the values of remanent polarization (P_r), saturated polarization (P_s) and a coercive field (E_c).

Fig. 4 shows a remarkable ferroelectric P - E hysteresis loop in terms of its shape and area evolution measured at 80K after electro – thermally poling of undoped $TlInS_2$ sample inside the temperature region where TE2 deep level traps are activated. The hysteresis loops are saturated, and exhibit clear nonlinear character without loss contribution. The shape of P - E curve in the terms of geometric configuration is Single Square – like with a rectangular factor of ~ 0.15. The value of saturation polarization (P_s) and remanent polarization are provided in Fig. 4. It is noted that the shape of $P - E$ hysteresis loops shown in Fig. 4 is typical for ferroelectric materials where no apparent pinning phenomenon exists, indicating that crystal structure defects are less.

It is well known that the ferroelectric phase is essentially the cooperative phenomena, which is stabilized by the long range coulomb interaction of electric dipole moments that appears spontaneously in each cell. Hence, there are several factors which are responsible for energy loss in dielectric materials. Crystal defects, inhomogeneity's, domain boundaries, and pores are the internal sources for energy losses. In defective ferroelectric crystal with charged deep level centers, more and more ferroelectric domains are constrained by the applied stress and cannot be re - oriented by the electric field so as to participate in the polarization reversal. Furthermore, it is noted that electric field cloud surrounding each ionized deep level defects could be reduce the sample volume (due to the growth of the frozen domains fraction) involved into polarization reversal processes.

The energy density of the dielectric materials can be calculated using the integral $\oint EdD$, where E is the applied electric field on the materials, $D(T) = \varepsilon_0 E + P(T)$ is the temperature evolution of electric displacement and $P(T)$ is the total polarization that is a sum of induced and spontaneous polarization of material. In ferroelectric materials, $D(T)$ is approximately equal to $P(T)$. Generally, the spontaneous polarization gives the main contribution in temperature dependence of $P(T)$. Geometrically, the integral the integral $\oint EdD$ means the area enclosed by P - E curve [33 - 36].

On the other hand, the temperature dependence of spontaneous polarization (P_{spon}) of improper ferroelectrics below of the phase transition temperature T_c has the form [33 - 36]:

$$P_{spon} = \Upsilon \cdot (T_c - T)^2, \qquad (2)$$

where Υ is constant composed from the Landau thermodynamic potential coefficients. It is obviously, that the area of ferroelectric P - E hysteresis loop should increase with a decrease in temperature.

Physically, the integral $\oint EdP$ indicates the polarization dissipation energy subjected to one full cycle of electric field application, and the loop area is therefore directly related to the crystal volume involved in the switching process during the application of the electric field. In other words, the area enclosed by the P - E curve and polarization axis represents the ratio of non - polar phase regions contained in the volume of sample to polarized ones.

To understand at least qualitatively the experimental results related to the contribution of each of charged native deep level defects in polarized properties of $TlInS_2$ ferroelectric - semiconductor, one needs to consider the following statements. Electro - active materials, which are able to retain electric polarization over a long period of time and create an internal static electric field, are known as electrets [37 - 40]. It is well known that electret behavior of semiconductor materials arises from both the dipole orientation and the charge storage. The internal electric field in semiconductor materials submitted to an external electric field may originate from hetero – and homo - charges [37- 40]. An internal electric field is created by space charges accumulated in the trap levels in the regions directly adjacent to the electrodes (homo - charge) as well as in the bulk region of the crystal (hetero - charge) [37 - 40]. The internal electric field created by homo - charges has the same direction as the field applied to the sample. The field created by hetero - charges formed in the bulk region of crystal and originated from ionized native deep level defects has the direction opposite of the direction of applied field.

When the native deep level defects B7, B5 and BT23 are activated by previously electrothermal poling of crystal, the internal electric field inside the crystal from charged deep level centers has the direction opposite to the direction of an external poling field [14, 16 – 20, 22 – 28, and 37 - 41]. This imprinted internal field tends to keep the ferroelectric domains aligned away from the direction of the applied electric field preventing reorientation of the domains along the external applied field direction resulting in a lower value of saturated polarization (Figs. 2 and 3). When the applied (Sawyer – Tower) electric field is reduced to zero and then changes the direction, the domain unable to rotate back away due to the frozen internal electric field. This leads to a reduction of remnant polarization in comparison with ones measured on $TlInS_2$ crystals with non - activated

deep level defects (Fig. 1). The decrease of the integral $\oint EdP$ area in Fig. 4 indicates that more and more ferroelectric domains are involved in polarization switching process and can be reoriented by the applied electric field. Thus, in undoped $TlInS_2$ sample with non – activated deep level defects or in the same sample with activated B7, B5 and BT23 deep level centers not the whole $TlInS_2$ ferroelectric crystal volume is involved in the polarization reversal process.

3.4 The *P* - *E* hysteresis loops of $TlInS_2$: La poled under different external fields

In order to gain further insight into the role of La doping, hysteresis loops of $TlInS_2$ with ~ 0.3 mol % La were measured at several temperatures on heating. Typical for $TlInS_2$: La sample *P* - *E* hysteresis loops measured at 80 K have been plotted in Fig. 5 (a). It can be observed that these loops do not saturate even under an applied field of 40 kV/cm. With temperature increase the shape of hysteresis loops shrinks from sharp - tip rhombic to very slim. The dielectric loop pattern in $TlInS_2$: La was observed at temperature below ~ 150 K only.

It is known that La doping induces the formation a lattice distortion in crystalline structure $TlInS_2$. This can be explained by saying that the ion radius of La^{3+} 0.187 nm) cation is larger than ones for Tl^{+} (0.149 nm) and In^{3+} (0.092 nm). The internal stress is due to by La additions can be considered as polar micro – domains. Obviously, the ferroelectric macro - domain state in $TlInS_2$ became more and more unstable at the temperature range where BTE43 deep level traps related to La dopant are active ($\Delta T = 156 – 176K$).

A double *P* - *E* hysteresis loops is observed in the same $TlInS_2$: La sample at T ≤ 150K after thermally poling of sample by an external electric field in the temperature region where BTE43 deep level traps are activated and under the illumination, as shown in fig.5(b). To investigate the origin of the double *P* - *E* loops in $TlInS_2$: La possible influences of light with different wavelength that can affect the *P* - *E* hysteresis loops of $TlInS_2$: La sample were checked. The function of the background illumination is to excite electrons from the valence band of $TlInS_2$: La into deep level traps, thus keeping the traps full with electrons, and leave holes in the valence band. To do this, the xenon lamp with set of different optical filters was used. Various excitation wavelengths of more than ~ 540 nm (the wavelength corresponding to the forbidden gap of $TlInS_2$) can be used as background illumination. According to the results of our experiment, ~ 700 nm is the best wavelength for the background. Stable and pronounced double *P* - *E* hysteresis loops under the background illumination of ~ 700 nm with red filter were observed. Despite extensive efforts, the physical origin of the double *P* - *E* hysteresis loops in $TlInS_2$ layered semiconductor with La additions remain were unclear. We can only assume that BTE43 deep level traps related to La dopant can be electrically activated on thermal poling of $TlInS_2$: La sample by an external electric field and under the illumination. The ionized BTE43 defects can lead to the release of free carriers either in the conduction band or in the valence band and transform to defect dipole. These defect dipoles can pin the ferroelectric domains irreversibly and induce the double *P* - *E* hysteresis loops.

Rather unexpected change of the shape of *P* - *E* hysteresis loops of the same $TlInS_2$: La sample was observed after annealing of the crystal for 5 h within the INC – phase at 210 K. A triple – like hysteresis loop at low temperatures as manifestation of a memory effect was detected in $TlInS_2$: La crystal. This triple hysteresis loops consists of three loops in which two of them are the inversions of each other about the origin and one is central loop, as seen in Fig. 5 (c). Note that, the presence of the central loop means the appearance of a new component in the crystal polarization at low temperatures [42, 43]. One may deduce that the triple *P* - *E* hysteresis loop behavior is related to the interaction of BTE43 defects with DDW. It should be noted that neither double – like nor triple hysteresis loops were observed in undoped $TlInS_2$ under similar experimental conditions.

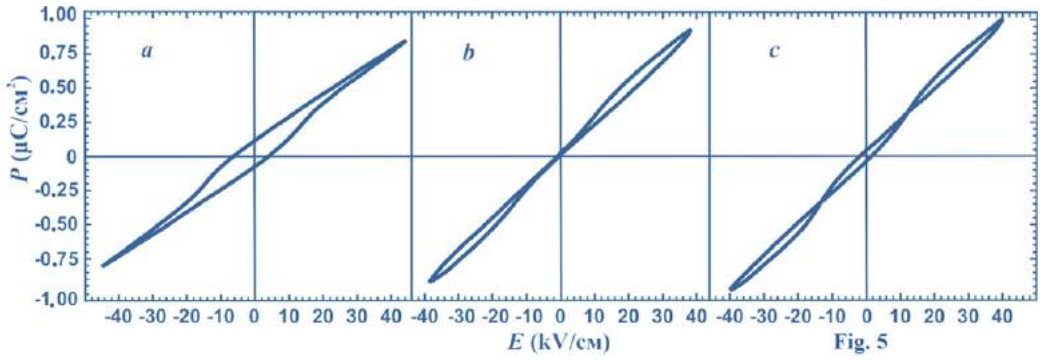

Fig. 5

Fig. 5. Multipolar *P* – *E* hysteresis loops of La doped $TlInS_2$ sample measured at 80 K; a) under normal conditions; b) after sample poling by an external electric field and after the illumination of crystal by visible light of ~ 700 nm wavelength in the temperature region ~ 155 – 175 K, where BTE43 deep level traps are thermally activated; c) after crystal annealing for 5 h inside the INC – phase.

In summary, five types of native deep trap levels in undoped and La – doped $TlInS_2$ ferroelectric semiconductor have been identified in our previous work [14 - 21]. These traps act as charge storage centers and can be served as origin of the internal electric fields inside the material. It was found, that BTE43 deep level defect is related to La – dopant because of its absence in undoped $TlInS_2$. In this study, the effect of each activated deep level defect on the polarization properties of $TlInS_2$ and $TlInS_2$:La was investigated by using *P* - *E* ferroelectric

hysteresis loop measurements. Deep level defects in both samples were activated at different temperatures by an external electric field, light illumination and long-time thermal annealing procedure inside the INC - phase in the memory effect regime. Special attention is given to BTE43 deep level defect. As a result, multiple *P* - *E* hysteresis loops in $TlInS_2$:La were found depending on the activation way of this type of defect. Finally, observations presented in this paper are consistent with earlier investigations of the effect of native deep level defects in $TlInS_2$ and $TlInS_2$:La on their electric, ultrasonic, pyroelectric and thermally depolarization properties recently published in literature [14 - 21].

5. DISCUSSION

Firstly, we note that the analogy between domain walls movements in ferroelectric crystals and damped mechanical oscillator model gives good results for the study of switching of crystal polarization under the electric field. We can obtain a perfect fit between measured ferroelectric hysteresis loop curves and the simplest model of friction - induced vibrations consisting of a spring - mass - damper system. It has been demonstrated here that the universal nonlinear oscillator behavior may be identified by studying of *P* - *E* hysteresis loops phenomena. The understanding and modelling of *P* - *E* hysteresis loops in undoped $TlInS_2$ and $TlInS_2$: La under external excitations will allow to establish the mechanical analog of deep level defects and physically the mechanical analogies of ME.

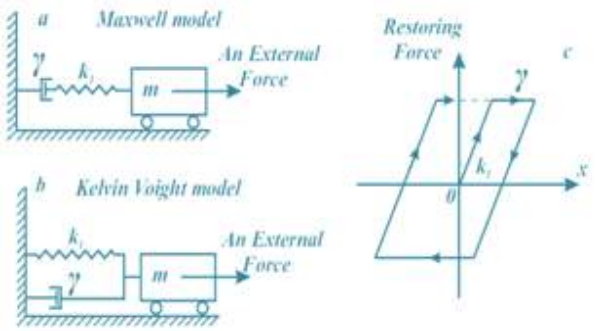

Fig. 6. Schematic diagram of Maxwell (a) and Kelvin - Voigt (b) oscillatory model; c) A typical hysteresis cycle of restoring force vs. displacement for Maxwell and Kelvin - Voigt models under a sinusoidal external excitation.

We consider an oscillator system with a single degree of freedom consisting of a mass, a Hookean elastic spring, and a Newtonian damper (or dashpot). The mass is moving on a smooth surface without friction. The Maxwell oscillatory model called a model when the elastic spring and the dashpot element are connected in series as it is shown in Fig. 6 (a). The Kelvin – Voigt model is shown in Fig. 6 (b) where the spring element and dashpot are connected in parallel [44 - 50]. The constitutive equation of motion for such mechanical systems is described by the ordinary differential equation:

$$m\frac{d^2x}{dt^2}+\gamma\frac{dx}{dt}+k_1x=f_0\cos(\omega t), \qquad (3)$$

where x is the displacement, m is the oscillator mass, γ is the dissipation or damping coefficient, k_1 is the linear spring constant, $f_0\,cos(\omega t)$ denotes a periodic force applied to the system and f_0 is the force amplitude. To compare with our data, $f_0\cos(\omega t)=|e|E(\omega_{ST}t)$, where $|e|$ is the electron charge and $E(\omega_{ST}t)$ is the electric field pulse in a triangular wave type with the Sawyer - Tower circuit frequency $\omega_{ST}=50$ Hz.

We orient the system along the x - axis, and let $x=x(t)$ denote the horizontal displacement of the attached mass m from the static equilibrium position $x=0$ of the spring. For the case of simplicity we assume that the periodic external force has the form of a sine – wave ($eE_{max}\sin\omega_{ST}t$) or even a rectangular wave with the frequency ω_{ST}. Also one assumes that the material is completely rigid.

The differential equation (1) describes the behavior of the linear oscillator with eigenfrequency $\omega_0=\sqrt{k_1/m}$. Typical restoring force (normalized by the mass of the oscillator) vs. displacement relationship for Maxwell / Kelvin – Voigt model for illustration purposes is depicted in Fig. 6. The idea of this model is as follows: When the displacement increases or decreases continuously, the gain between the force and the displacement changes piecewise linearly.

Let us suppose that the motion is started from the rest by moving the mass m to the right under an external force. An external force in the beginning will deform an elastic spring.

The mechanical energy stored in the elongated elastic spring (for smaller elongation in magnitude) will take to overcome the friction force in the damper. The extra positive displacement will be in oscillatory system even when the external force changes direction.

The mechanical restoring force - displacement hysteresis loops will take place in Maxwell or Kelvin – Voigt oscillatory systems. Obviously that the area overlapping by hysteresis loop curve will depend on its internal parameters; the damping coefficient (γ) and elastic spring constant (k_1).

From visual inspection of the hysteresis loops shown in Figs. 1 – 3 and 6 one can assume that thermally – electro activation of B7, B5 and BT23 deep level defects in $TlInS_2$ is equivalent to changing of the mechanical parameters γ and k_1 in Maxwell or Kelvin – Voigt oscillatory models.

The double restoring force – displacement hysteresis loops is observed for nonlinear oscillatory system when a nonlinear spring (Voigt element) is added in series with damper element, as it is shown in Fig. 7.

The nonlinearities of the spring are taken into account by adding the term of k_3x^3 – a cubic restoring force in the equations of motion (3). Here k_3 is the cubic stiffness parameter. For $k_3>0$ the spring hardens with increasing displacement (spring hardening), for $k_3<0$ the spring softens with increasing displacement (spring softening).

Figure 7 (b) shows a schematic representation of the double restoring force – displacement hysteresis loops.

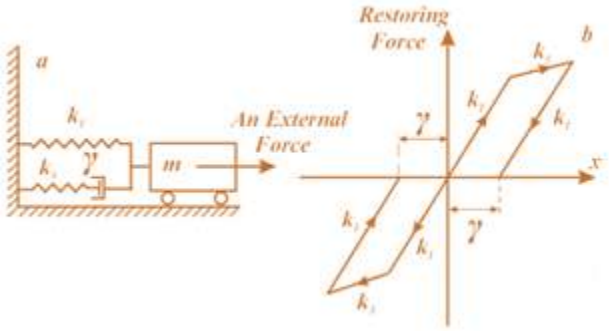

Fig. 7. a) Schematic set - up for single degree of freedom non – linear damper oscillatory model. b) Restoring force versus displacement double hysteresis loop for non - linear damper oscillatory model.

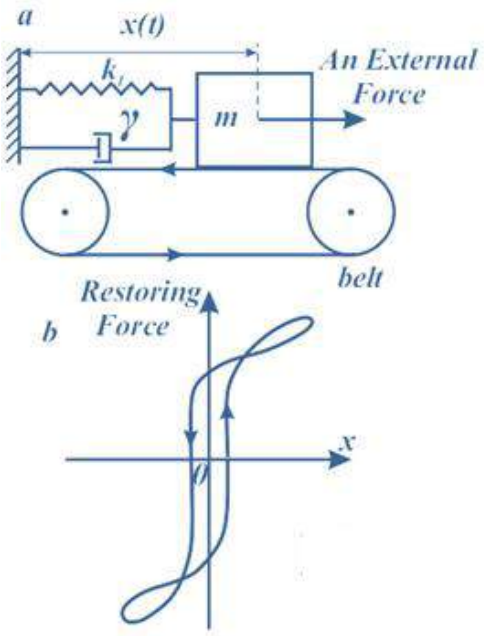

Fig. 8. a) A schematic plot of the damped harmonic oscillator on a moving belt as a model of harmonic oscillator damped by Coulomb friction; b) Triple hysteresis loop characteristics of the restoring force as a function of the displacement for such model.

Finally, let's consider a single degree of freedom spring - mass - damper oscillator model in which the mass resting on a moving belt. The physical system is shown in Fig. 8. The equation governing the motion of the oscillator shown in Fig. 8 is given by:

$$m\frac{d^2x}{dt^2} + \gamma\frac{dx}{dt} + k_1 x + F_{friction} = f_0\cos(\omega t), \quad (4)$$

We added the friction to the system, since the mass – spring - damper is contacted with moved belt that causes friction. We describe it with the Coulomb law of dry friction, in which the friction resistance force is $F_{friction} = -\mu mg \cdot sgn(v_r)$. Here, μ is the coefficient of friction and g is the gravitational acceleration; $v_r = v_{belt} - \dot{x}$ is the relative velocity. The friction resistance force is opposite to the direction of motion, represented by the function $sig(v)$, which is given by [44 - 51]:

$$sgn(v) = \begin{cases} 1, & if\ v > 0 \\ 0, & if\ v = 0 \\ -1, & if\ v < 0 \end{cases}$$

In (4) for simplicity we assume that the periodical potential friction is sinusoidal and k_3 is zero.

The evolution of the oscillator state is described by the differential equation (4). This state can be in different acceleration and deceleration phases depending on the sign of the relative velocity giving different contributions to the friction forces. Hence, the restoring force – displacement curve follows different paths for acceleration and deceleration phases resulting in triple – type hysteresis loops form which is due to non - reversible friction.

The relation between the displacement of the oscillator and the restoring force is depicted schematically in Fig. 8 (b). It should be noted that a spring - mass - damper oscillator model with the Coulomb dry - friction have be used for modelling of triple – type $I - V$ hysteresis loops in the charge – density wave solids [52, 53].

By visual inspection of the shape of hysteresis loops shown in Fig. 4 and in Figs. 7 and 8 one can conclude that the mechanical prototype of charged BTE43 deep level defects is a nonlinear spring attached in series with damper. Activation of BTE43 deep level defects by the external electric field or by photo – excitation causes the energy dissipation in ferroelectric material due to the spatially inhomogeneous polarization initiated by BTE43 deep level defects, which role is similar to that of the nonlinear spring in an oscillator model.

Mobile defects and their spatial long range ordering (DDW) are often invoked as the microscopic explanation of some experimental observations inside the intermediate INC - phase of ferroelectric crystals such as thermal hysteresis effects and specific ME. In $TlInS_2$ as well as $TlGaSe_2$ it has been hypothesized that DDW - modulation interacts with the incommensurate modulation resulting in many intriguing properties at low temperatures which are still not explained [5, 8, 14 - 21]. DDW is a periodic distortion of the crystal lattice due to by periodic displacements of the atoms from their normal positions. Lattices deformed in this way initiate the micromechanical inelastic stress and strain fields inside the crystal [52, 54, 55]. The mechanical analogy of DDW is internal friction which characterizes energy dissipations at mechanical loading. Thus spring - mass - damper oscillator moving in the presence of the Coulomb friction is the mechanical prototype of the ME in $TlInS_2$: La. Charged BTE43 deep level defects interacting with domain wells in a "electrically viscous" surrounding is the origin of triple – type $P - E$ hysteresis loops in $TlInS_2$: La.

4. CONCLUSIONS

Thus, the experimental investigation of the effect of deep level defects on ferroelectric hysteretic loops in undoped $TlInS_2$ and $TlInS_2$:La has been performed. The $P - E$ hysteresis loops were studied as a function of temperature inside the ferroelectric phase at various external electric field intensities. It has been revealed that

in undoped $TlInS_2$ sample the activated B7, B5, BT23 and TE2 deep level centers greatly affect the geometrical shape (saturated and unsaturated loops) and parameters (coercive field, remnant and saturated polarization) of dielectric hysteresis loops.

The effect of deep level defects on *P - E* hysteretic loops in $TlInS_2$: La sample is fully different from undoped $TlInS_2$. The double – type hysteresis loops have been detected in $TlInS_2$: La at all temperatures below ~ 190K after activation of BTE43 deep level defects by external electric field poling procedure. Furthermore, the double – type hysteresis loops were revealed in $TlInS_2$: La under activation of BTE43 deep level centers by background illumination. Unexpectedly, triple – type dielectric hysteresis loops were observed in $TlInS_2$:La at $T < 190$K after annealing of the sample during 5 hours within the INC – phase. It has been assumed that BTE43 deep level traps are corresponded to La – dopant. Different type spring - mass - damper oscillator models are involved in order to qualitatively understand the mechanical analogues of observed phenomena. The dramatic increase in the internal friction in $TlInS_2$ as a result of ME is the main result of the present investigation.

ACKNOWLEDGEMENTS

MS and FM acknowledge support from The Scientific & Technological Research Council of Turkey (TÜBİTAK) through the bilateral program RFBR (14-02-91374 CT_a) – TUBITAK (No. 213M524).

[1] *M.E. Lines, A.M. Glass.* Principles and Applications of Ferroelectrics and Related Materials (Oxford Clarendon, 1977).
[2] *B.A. Strukov, A.P. Levanyuk.* Ferroelectric Phenomena in Crystals (Springer, 1998).
[3] *R .A. Suleimanov, M. Yu. Seidov, F.M. Salaev and F. A. Mikailov.* Phys. Solid State 35, 177 (1993).
[4] *K.R. Allakhverdiev, N.D. Akhmed-zade, T.G. Mamedov, T.S. Mamedov, M.Yu. Seidov.* Low Temperature Physics 26, 56 (2000).
[5] *M-H. Yu. Seyidov, R. A. Suleymanov, S. S. Babayev, T.G. Mammadov, A.I. Nadjafov, and G.M. Sharifov.* Phys. Solid State 51, 264 (2009).
[6] *F.M. Salaev, K. R. Allakhverdiev and F. A. Mikailov.* Ferroelectrics 131, 163 (1992).
[7] *F.A. Mikailov, E. Başaran, T.G. Mammadov, M.Yu. Seyidov, E. Şentürk.* Physica B, 334 13 (2003).
[8] *S.S. Babaev, E. Basaran, T.G. Mammadov, F. A. Mikailov, F. M. Salehli, M-H. Yu. Seyidov, R.A. Suleymanov.* J. Phys.: Condens. Matter, 17 1985 (2005).
[9] *H. Hahn, B. Wellman.* Naturwissenschaften B. 4, 42 (1967).
[10] *T.J. Isaacs, T.D. Feichtner.* J. Solid State Chem. 14, 260 (1975).
[11] *S. Ozdemir, M. Bucurgat.* Current Applied Physics 13, 1948 (2013).
[12] *M.M. El - Nahass, M.M. Sallam, A. H. S. Abd Al – Wahab.* Current Applied Physics 9, 311 (2009).
[13] *O.V. Korolik, S.A.D. Kaabi, K. Gulbinas, N.V. Mazanik, N.A. Drozdov, V. Grivickas.* J. Luminescence, 187, 507 (2017).
[14] *M-H. Yu. Seyidov, R. A. Suleymanov, F. Salehli.* J. Appl. Phys. 108 024111 (2010).
[15] *M-H. Yu. Seyidov, R. A. Suleymanov, A. P. Odrinsky, A. I. Nadjafov, T. G. Mammadov, E. G. Samadli.* Jap. J. Appl. Phys. 50, 05FC08 (2011).
[16] *A. P. Odrinsky, T. G. Mammadov, MirHasan Yu. Seyidov, V. B. Aliyeva.* Physics of the Solid State 56 1605 (2014).
[17] *MirHasan Yu. Seyidov, A.P. Odrinsy, RA. Suleymanov, E. Acar, T. G. Mammadov, V. B. Aliyeva.* Physics of the Solid State 56, 2028 (2014).
[18] *MirHasan Yu. Seyidov, R. A. Suleymanov, E. Acar, A. P. Odrinsky, T. G. Mammadov, A. I. Nadjafov, V. B. Aliyeva.* Low Temperature Physics 40, 830 (2014).
[19] *MirHasan Yu. Seyidov, R. A. Suleymanov, F. A. Mikailzade, E. Orhan Kargın, A. P. Odrinsky.* Japan Appl. Phys. 117, 224104 (2015).
[20] *MirHasan Yu. Seyidov, R. A. Suleymanov, C. Kırbaş, A.P. Odrinsky*. Physica B. Cond. Mat. 497, 86 (2016).
[21] *MirHasan Yu .Seyidov, R. A. Suleymanov, F. Salehli, S. S. Babayev, A. I. Nadjafov, T. G. Mammadov, G. M. Sharifov.* Physics of the Solid State 51, 568 (2009).
[22] *J.P. Jamet, and P. Lederer.* J. Phys. (Paris) Lett. 44, L-257(1983).
[23] *J.P. Jamet, and P. Lederer.* Ferroelectric Lett. 1, 139 (1984).
[24] *P. Lederer, G. Montambaux and J. P. Jamet.* J.Phys.(Paris) Lett. 48, L-627(1984).
[25] *P. Lederer, G. Montambaux and J. P. Jamet.* Mol. Cryst. Liq. Cryst. 121, 99 (1985).
[26] *P. Lederer, J.P. Jamet, and G. Montambaux.* Ferroelectrics 66, 25 (1986).
[27] *J. Lee, C. H. Choi, B. H. Park, T. W. Noah and J. K. Lee.* Appl. Phys. Lett. 72, 3380 (1998).
[28] *K. Abe, S. Komatsu, N. Yanase, K. Sano and T. Kawakubo.* Japan. J. Appl. Phys. 36, 5846 (1997).
[29] *M. Alguero, J.M. Gregg, and L. Mitoseriu.* Nanoscale Ferroelectrics and Multiferroics, vol.1 (John Wiley & Sons Ltd, 2016)
[30] *A.G. Milnes.* Deep Impurities in Semiconductors (Jonh Wiley&Sons, New York, London, Sydney, Toronto, 1973)
[31] *M.A. Lampert and P. Mark.* Current Injection in Solids (Academic Press, New York, London, 1970)
[32] *A.S. Sidorkin.* Domain Structure in Ferroelectrics and Related Materials (Cambridge International Science Publishing, 2006)
[33] *K. Uchino.* Ferroelectric Devices (CRC Press, Taylor & Francis Group, 2010)
[34] *Y. Xu.* Ferroelectric Materials and their Applications (Elsevier Science Publishers B.V., 1991)
[35] *H.D. Megaw.* Ferroelectricity in Crystals (London: Methuen, 1957)

[36] *S.B. Lang, and H.L.W. Chan.* Frontiers of Ferroelectricity (Springer Science+Business Media LLC, 2007)
[37] *G.M. Sessler.* Journal of Electrostatics 51 – 52 (2001) 137 – 145.
[38] *G.M. Sessler* (ed.) Electrets. Topics in Applied Physics v. 33 (Springer, 1987)
[39] *V. M. Fridkin.* Ferroelectrics - Semiconductors (New York Consultants Bureau, 1980)
[40] *V.M. Fridkin.* Photoferroelectrics (Berlin Springer, 1979)
[41] *MirHasan Yu. Seyidov, R. A. Suleymanov, R. Khamoev.* Phys. Solid State 48 (2006) 1346 – 1350.
[42] *M.E. Lines, A.M. Glass.* Principles and Applications of Ferroelectrics and Related Materials (Oxford Clarendon, 1977)
[43] *B.A. Strukov, A.P. Levanyuk.* Ferroelectric Phenomena in Crystals (Springer, 1998)
[44] *F.C. Moon, Chaotic Vibrations.* An Introduction for Applied Scientists and Engineers (John Wiley & Sons, Inc., 2004)
[45] *L. Meirovitch.* Fundamentals of Vibrations (McGraw-Hill Book Co. Singapore, 2001) and Elements of Vibration Analysis (McGraw-Hill, Boston, Massachusetts 1986).
[46] *G.T. Houlsby and A.M. Puzrin.* Principles of Hyperplasticity. An Approach to Plasticity Theory Based on Thermodynamic Principles (Springer-Verlag London Limited 2006).
[47] *A.H. Nayfeh, and D.T. Mook.* Nonlinear Oscillations (Wiley Classics Library Edition Published 1995)
[48] *S.H.H. Kachapi, and D.D. Ganji.* Dynamics and Vibrations. Progress in Nonlinear Analysis (Springer Science Business Media B.V. 2014)
[49] *M. Lalanne, P. Berthier, J. Der Hagopian.* Mechanical Vibrations for Engineers (John Wiley and Sons, Chichester, New York, Brisbane, Toronto, Singapore 1984).
[50] *C.W. de Silva, Vibration and Shock Handbook.* (Taylor & Francis Group, Boca Raton, London, New York, Singapore, 2005).
[51] *E.J. Vernon - Carter, G. Avila de la Rosa, H. Carrillo Navas, Y. Carrera, J. Alvarez – Ramirez.* J. Food Engin.69, 18 (2016).
[52] *L.P. Gor'kov, and George Grüner (ed.).* Charge Density Waves in Solids (Modern Problems in Condenced Matter Sciences, vol. 25, Elsevier Science Publishers B.V., Amsterdam, Oxford, New York, Tokyo, 1989)
[53] *G.X. Tessema and N.P. Ong.* Phys. Rev. B. 31, 1055 (1985); Phys. Rev. B. 27, 1417 (1983).
[54] *R. Blinc, and A. P. Levanyuk (ed.).* Incommensurate Phases in Dielectrics, Part 1, Fundamentals; Incommensurate Phases in Dielectrics, Part II, Materials (Amsterdam North-Holland, 1986).
[55] *H.Z. Cummins.* Phys. Reports 185, 409 (1990).

Recevied: 12.06.2017

THE INFLUENCE OF SYNTHESIS REGIME ON SUPERCONDUCTING PROPERTIES OF $Bi_2Sr_2Ca_1Cu_2O_X$

S.S. RAGIMOV, G.I. AGAYEVA
Institute of Physics of Azerbaijan National Academy of Sciences
H.Javid ave., 131, AZ-1143, Baku, Azerbaijan
e-mail: sadiyar@mail.ru

It was investigated the temperature dependence of specific resistivity, thermal power and excess conductivity of $Bi_2Sr_2Ca_1Cu_2O_X$ in 77-300K temperature region. A superconducting transition was observed at 78K. It was analyzed the influence of fluctuations on the conductivity in the superconducting transition region. The 2D-3D crossover temperature T_{cr} was determined. The microscopic parameters such as dimensional crossover temperature (T_{cr}), interlayer coupling strength (J), and zero temperature coherence length along c axis (ξ_0) are estimated.

Keywords: superconducting material, specific resistivity, thermal power, excess conductivity, coherence length, temperature dependence.
PACS:74.62.Bf; 74.25.F; 74.40.-n

INTRODUCTION

Bi-based superconductors (BSCCO- Bismuth Strontium Calcium Copper Oxide) are the first high temperature superconductors, which did not contain a rare earth element. It is a cuprate superconductor, which shares a two-dimensional layered Perovskite structure with the superconducting copper oxide plane. It has general formula Bi_2Sr_2Can-1CunO2n+4+x with specific transition temperature ranging from T_c=20K (n=1, (2201) phase), 85K (n=2, (2212) phase), 110K (n=3, (2223) phase) and 104K (n=4, (2224) phase) [1].

It is well known that the superconducting properties of Bi-based compounds are very sensitive to the hole concentration, which depends on the atomic displacement. Substitutions into the BSCCO system affect strongly the carrier concentration and therefore lead to significant changes both on the electronic and superconducting properties [2-4].

The method of superconductor preparation and the sintering conditions greatly influence it. The electrical transport properties of HTSC are very sensitive to the chemical compositions, sintering temperature, sintering time, type and amount of substitutions [2-5].

The present work is devoted to study the transport properties of $Bi_2Sr_2Ca_1Cu_2O_X$ polycrystalline. It was investigated the influence of synthesis regime on the specific resistivity, thermal power and exsess conductivity of $Bi_2Sr_2CaCu_2O_X$ in the 77-300K temperature interval.

EXPERIMENTAL RESULTS AND DISCUSSION

The samples have been prepared by the solid state method by taking $CaCO_3$, $SrCO_3$,Bi_2O_3 and CuO as starting precursors and mixed in appropriate amount with a Bi:Sr:Ca:Cu cation ratio of 2:2:1:2. These materials were pressed and then sintered in air at 840^0C for 5 hours (sample-1) and 10 hours (sample-2) then quenched to room temperature.

The phase purity of the obtained samples was investigated by X-ray diffraction. The XRD analysis was performed using a Brucker -D8 advance diffractometer at room temperature with scanning mode with a step size $\Delta(2\theta)=0.05^0$ and $5^0 \leq 2\theta \leq 80^0$. From the XRD data, various structural characteristics (such as, lattice parameter: *a*=5.39790A; *c*=30,68500A, system-tetragonal, space group (P4(75)), and grain size (465,7A) were deduced.

The resistivity and thermal power were measured using standard four-point probe technique with a 6-1/2-digit precision multimeter (8846A-Fluke). For taking the measurement, the sample is mounted in cryostat, and then four probes are electrically connected to the sample by indium.

The thermal power was measured by applying a longitudinal heat flux with a constant power released in the heater. The temperature gradient in the sample between probes varied from 0.5 to 2K. The thermal power of the sample was measured relative to copper. The thermal power sign is negative over the entire measured temperature range. This behavior indicates that the electron carriers are dominant. Thermal power value increases almost linearly with temperature decreasing. The temperature dependence of thermal power goes through a maximum *T*~117K then rapidly falls to zero below T_c for both $Bi_2Sr_2Ca_1Cu_2O_X$. The temperature dependence of thermal power is linear in the normal state of both investigated samples, and similar to that of the high-T_c cuprates. To interpret the measured data on thermal power, we take into consideration that this compound exhibits multiband superconductivity. Detail discussion is made elsewhere [5].

During the measurement, an interesting fact was revealed that the sign of the thermal power of both samples, unlike the other HTSCs, was negative. The reason for this is still difficult to explain, because the thermoelectric power sign of Bi-based HTSC is positive, especially if the critical temperature is above 50K [1,3,5].

The temperature dependences of the resistivity of $Bi_2Sr_2CaCu_2O_X$ samples are plotted on fiq.1. As can be seen, the ρ *(T)* dependences of samples have a metallic behavior above the T_c. The phase transition from normal metallic state to superconducting state happens at temperature T_c=78K, and T_c=78.5K respectively for samples-1 and sample-2 and calculated from the first order derivative plot.

131 H.Javid ave, AZ-1143, Baku
ANAS, G.M.Abdullayev Institute of Physics
E-mail: jophphysics@gmail.com

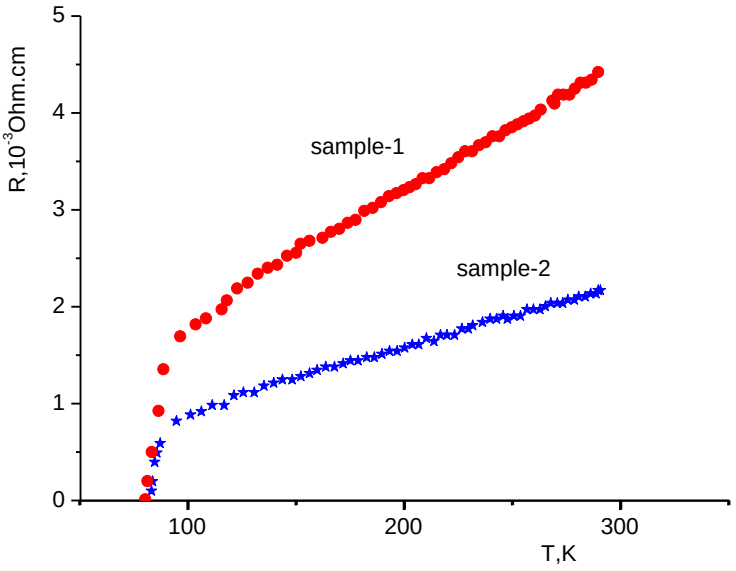

Fiq.1. The temperature dependencies of specific resistivity of $Bi_2Sr_2CaCu_2O_X$.

The temperature dependence of these samples is almost identical. However, the values of the resistivity of these samples differ by two times. Their annealing times are two times different also. As can be seen, the longer the annealing time reduce to the lower of their resistance.

The temperature dependence of the resistance deviates from linearity at 117K (sample-1) and 112K (sample-2). The deviation from the linearity of the temperature dependence of the resistivity is a common characteristic of HTSC materials. Starting from a certain temperature T^*, the resistance decreases more rapidly with decreasing temperature than at high temperatures. A sharper decrease in the resistance of the sample below T^* is a consequence of the formation of superconducting cooper pairs at these temperatures [6].

The phase diagram of high-temperature and low-temperature superconductors is very different. If in the low-temperature superconductors only the Meissner and normal parts take place, then in HTSC the picture becomes a little more complicated, there arises, in addition to everything else, an area with strong fluctuations. The reason for this is primarily due to the fact that the longitudinal and transverse coherence lengths in HTSC materials are very small. And this, in turn, leads to a rather small amount of coherence, where only a few Cooper pairs are contained.

As is well known, in the region of the phase transition (PT), the conductivity is significantly affected by superconducting fluctuations [6.7]. The resistivity $\rho(T)$ is affected by superconducting fluctuations resulting in noticeable deviation of $\rho(T)$ down from its linear dependence at higher temperatures and its analysis is one of the experimentally accessible methods just shedding light on the normal state transport properties of HTSC [6]. The Aslamasov and Larkin (AL) [8] and Lawrence and Doniach (LD) [9] models are used for description of fluctuations in intergrain and intragrain regions of HTSC cuprates. The excess conductivity is generally analyzed by using these two models. According to the LD model, the excess conductivity $\Delta\sigma$ due to superconducting fluctuations are expressed by [6]

$$\Delta\sigma = \left(\frac{e^2}{16\hbar d}\right)\left(\frac{T}{T_c}-1\right)^{-1}\left[1+J\left(\frac{T}{T_c}-1\right)^{-1}\right]^{-1/2} \qquad (1)$$

where $J = (2\xi_c(0)/d)^2$ is interlayer coupling strength, $\xi_c(0)$ is zero temperature coherence length along c axis, and d-distance between layers.

The physical reason for the appearance of excess conductivity is that, as a result of thermal fluctuations, Cooper pairs appear at a temperature above T_c, which creates an additional channel for the electric current.

As is seen from (1) at high temperatures $T>>T_c$ (where $J<<\varepsilon$; $\varepsilon = \left(\frac{T}{T_c}-1\right)$, $\Delta\sigma$ is proportional ε^{-1} (2D – conductivity), and nearly to transition temperature T_c (where $J>>\varepsilon$), $\Delta\sigma$ is change as $\varepsilon^{-1/2}$ (3D – conductivity).

The 2D–3D crossover temperature T_{cr} was determined according to expression $\varepsilon = 4\gamma$; where $\varepsilon = (T-T_c)/T_c$ and $\gamma = (\xi_c(0)/d)^2$:

$$T_{cr} = T_c\{1 + 4(\xi_c(0)/d)^2\} \qquad (2)$$

Fig.2 shows the dependence of $\ln\Delta\sigma/\sigma$ versus $\ln (T-T_c)/T_c$ for the investigated samples.

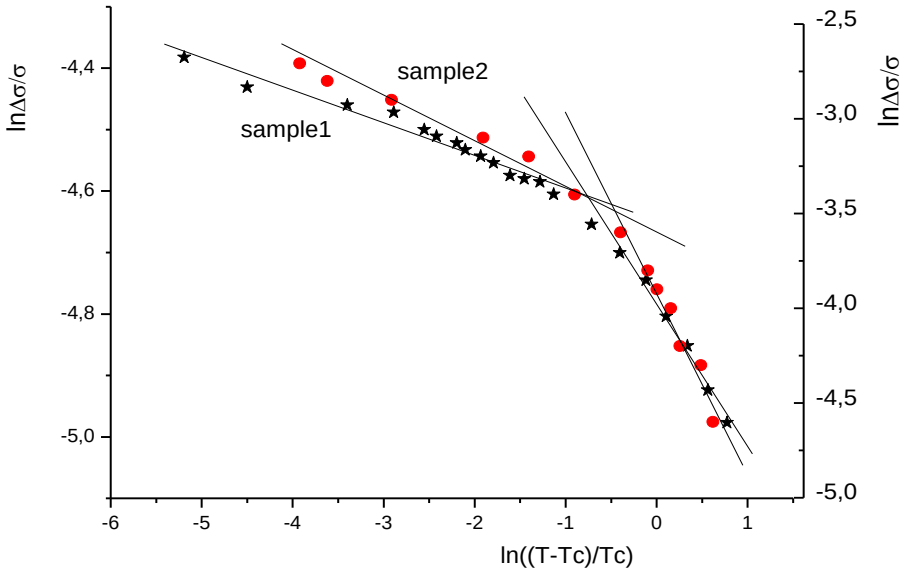

Fiq.2. The dependence of $ln\Delta\sigma/\sigma$ versus $ln\ (T\text{-}T_c)/T_c$

Using experimental data (fig.2) and according to (2), the dimensional crossover temperature-the transition temperature of the 2D-3D fluctuation conductivity was calculated for the studied samples (T_{cr}(sample-1) =88K; and T_{cr} (sample-2) = 90K). The microscopic parameters such as interlayer coupling strength J (sample-1)=0,054; J(sample-2)=0,056, and zero temperature coherence length along c axis ξ_0(sample-1)=4Å; ξ_0(sample-2)=3,8Å are estimated. The value of J is characterized the degree of anisotropy of the system. The high values of J mean that the system is less anisotropic. It is known that Bi-based superconductors have a quasi-layered structure with CuO_2 planes in the unit cell [1.6] On the other hand Bi-based superconductors are quasi-two-dimensional superconductors with a weak interaction between copper-oxygen planes and strong anisotropy of resistance. The strong anisotropy of electronic properties is due to the weakening of the bond between the double CuO_2 layers.

CONCLUSIONS

The excess conductivity of two $Bi_2Sr_2CaCu_2O_X$ with different annealing times in the region of the superconducting phase transition is analyzed. It is obtained that an increase of the annealing time leads to an increase of microscopic parameters such as 2D-3D dimensional crossover temperature (T_{cr}), interlayer coupling strength (J) and decrease of resistivity.

[1] *I. Askerzade.* Unconventional Superconductors: Anisotropy and Multiband Effects, Springer, Berlin, Heidelberg, 2012.

[2] *D. Sykorova, O. Smrčkova, K. Rubešova, K. Knížek.* Physica B, 321, 295-297, 2002.

[3] *P. Mandal, A. Podder and S. Das.* J. Phys. Condens. Matter, v. 6, p.5689-5696, 1994.

[4] *I. Karaca, S. Celebi, A. Varilci, A.I. Malik.* Superconductor Science and Technology, 16,100-104, 2003.

[5] *S.S. Ragimov, I.N. Askerzade.* Jurnal Texnicheskoy Fiziki, 2010,t.80, v.10, s.150-151. (in Russian)

[6] *A.P. Solovev, H.U. Habermeyer and T. Haage*. FNT, v.28, p.146-152, 2002. (in Russian)

[7] *S.S. Ragimov, A.A. Saddinova, V.M. Aliev, R.I. Selim-zade.* Materials Science Forum, v. 845, p. 17-20, 2016

[8] *L.G. Aslamazov and A.L. Larkin. Phys. Lett.* 26À, 238, 1968.

[9] *W.E. Lawrence and S. Doniach.* in: Proc. of the 12th Int. Conf. on Low Temp. Phys., Japan, Kioto, 1971, p. 361.

Recevied: 18.09.2017

PHOTOCONDUCTIVITY OF INDIUM MONOSELENIDE CRYSTALS IN STRONG ELECTRIC FIELDS

A.Sh. ABDINOV[1], R.F. BABAYEVA[2]
[1]Baku State University,
Az1145, Baku city, Z. Khalilov street, 23
[2]Azerbaijan State Economic University
Baku, Azerbaijan Republic
Tel.: (994 12) 5397373, e-mail: abdinov-axmed@yandex.ru,
Babaeva-rena@yandex.ru

The influence of an external constant electric field on the spectral distribution and lux-ampere characteristic of the photoconductivity of indium monoselenide crystals with different (from ~$2\cdot10^3$ to $2\cdot10^6$ Ohm·cm) initial resistivity (ρ_0) at 77K is studied in the temperature range of 77-350 K at the electric field intensities from the extremely weak up to ~$2.5\cdot10^3$ V/cm

It has been established that for the crystals of this semiconductor in the region T <250 K at electric fields corresponding to the superlinear portion of the static current-voltage characteristic the main parameters and characteristics of the photoconductivity depend on the electric field intensity. It is supposed that found out at that dependence of parameters and characteristics of the photoconductivity on electric field is connected with spatial heterogeneity of the studied crystals and an electric flattening of the potential relief of the fluctuation of free energy zones in them.

Keywords: photoconductivity, single crystal, contact material, electric field, spectrum, light characteristic, injection, current-voltage characteristic.
PACS: 71.20. Nr, 72.20-i

1. INTRODUCTION

Indium monoselenide (InSe) single crystals possesses high photosensitivity in a wide range of the optical spectrum (0.35÷1.45 μm) [1] up to 350K that makes it perspective material for optoelectronics [2]. Although this semiconductor photoconductivity is studied for a long time [3-6], but not paid due attention to its dependence on the electric field. Proceeding from this, in this work we experimentally investigated the photoconductivity of indium monoselenide crystals in strong electric fields.

2. SAMPLES AND EXPERIMENTAL PROCEDURE

Investigated samples in the form of a plane-parallel plate were cleaved from homogeneous large n-InSe single crystal ingots of rhombohedral structure, which were grown by a modified Bridgman method [7]. Their geometrical dimensions did not exceed 0.30mm and (5.00x3.00) mm^2 in directions along and perpendicular to "C" axes (perpendicular and along layers) of the crystal, accordingly. As a material for current contacts tin, indium, silver paste and aquadag were used. Samples with various structure (sandwich and planar) and geometry relative to direction of current flow (longitudinal and cross-section) were prepared.

Measurements were carried out at temperatures 77÷350K in the range of change of wavelength λ=0.30÷2.00 μm and intensity $\Phi \leq 5\cdot10^2$ Lx). Intensity of electric field was changed from extremely weak up to intensity of switching [8]. Curves of spectral distribution (spectrum) and light characteristics (LC) for studied samples with various initial (at 77 K in the dark) specific resistance (ρ_0=$2\cdot10^3$-$2\cdot10^6$ Ohm·cm). Before each measurement for the purpose of deleting the residual phenomena connected with prehistory of the samples, samples were exposed to special temperature procedure [9].

3. EXPERIMENTAL RESULTS

On the basis of the carried out by us measurements it is established that at weak electric fields a spectrum and LC of the intrinsic photoconductivity (a photoconductivity excited by light from fundamental absorption region), besides the temperature, appreciably depend also on ρ_{T0} value of studied sample. In the temperature region $T \leq 250$ K and weak light both the value of separate parameters and a course of characteristics (a spectrum and LC) of the intrinsic photoconductivity for samples with various ρ_{T0} differ. Based on values of these distinctions, it is possible conditionally to divide n-InSe crystals into two groups - low-resistance ($\rho_0 \leq 10^3$ Ohm·cm) and high-resistance ($\rho_0 \geq 10^4$ Ohm·cm). Low-resistance crystals relatively poorly photosensitive, processes of the photo-response relaxation (establishment of stationary value at application of light and disappearance after the termination light exposure) have fast character (it is characterised by time constant $\tau \leq 10^{-6}$ s), photoconductivity spectrum has no additional structure, LC obey to power law with an exponent $0 \leq \alpha \leq 1$, the parameters and characteristics of the intrinsic photoconductivity under the conditions considered by us do not depend on the electric field.

Contrary to low-resistance crystals, high-resistance ones possess considerably high photosensitivity, processes of a relaxation of the photoconductivity in them have slow character, after light termination high multiple residual photoconductivity is observed [9]. In initial part of the LC superlinear site (where α sometimes reaches up to 6÷7) exists, the maximum and threshold frequency of

131 H.Javid ave, AZ-1143, Baku
ANAS, G.M.Abdullayev Institute of Physics
E-mail: jophphysics@gmail.com

the spectrum shifts to longer waves, the spectrum is expanded also owing to displacement of short-wave border to shorter wavelengths. On both branches of the spectrum (both on short-wave, and on long-wave) additional peaks occur, with growth of ρ_{T0} all this specificity of intrinsic photoconductivity amplifies, and with rise of the temperature and intensity of light they gradually disappear (Fig. 1).

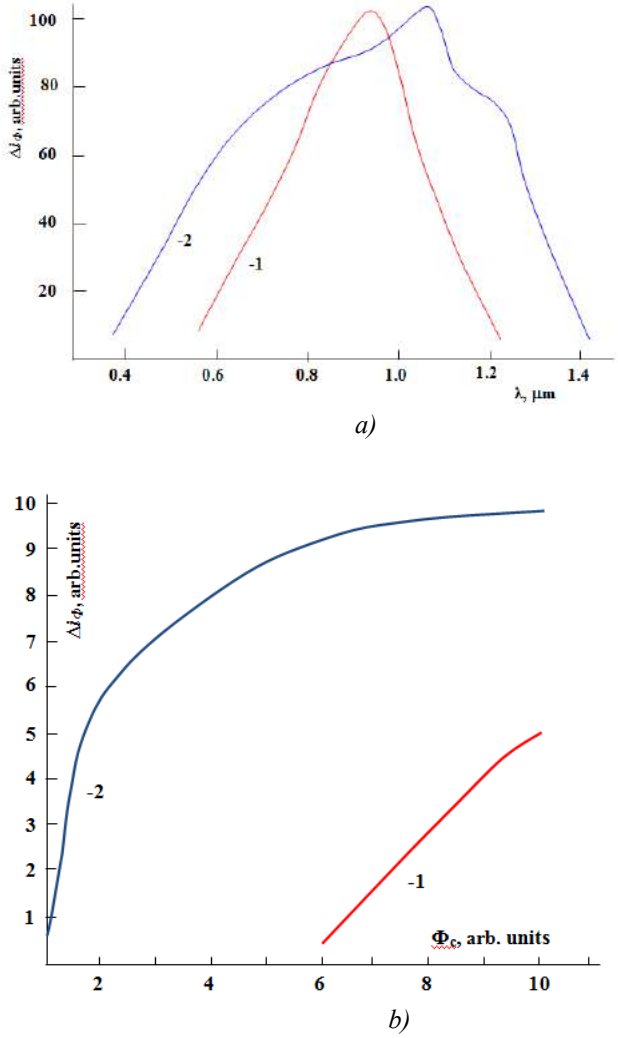

Fig. 1. Spectral distribution (a) and light (lux-ampere) characteristic (b) of the photoconductivity in n-InSe crystals with different initial specific resistance (ρ_O) at weak electric fields. ρ_O, Ohm·cm: 1 - $2\cdot10^3$; 2 - $2\cdot10^6$; T=77 K;б: λ= $\lambda_м$; E =50 V⁄cm; *a:* Φ=0.1$\Phi_м$, *b:* λ= $\lambda_м$.

However in high-resistance crystals in the region of low temperatures and weak illuminations at voltages (U), corresponding to non-linear part of the static the current-voltage characteristics (CVC) where appreciable injection through current contacts in the sample takes place, begins to appear dependence of parameters and characteristics of the intrinsic photoconductivity on electric field (E). With growth of ρ_0 effect of the electric field on photoconductivity becomes more appreciable, and with growth of Φ and increase of T it is weakened and at last wholly disappears.

On Fig.2 characteristic curves of spectral distribution (a) and lux-ampere characteristics (b) for n-InSe crystals with different initial specific resistances (ρ_O) at different E are shown.

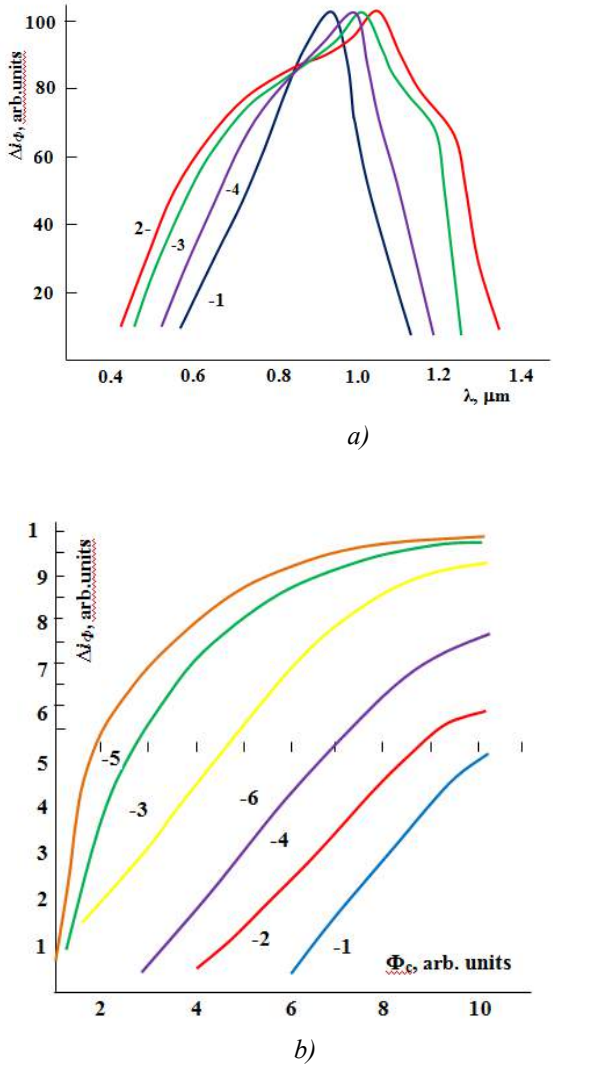

Fig. 2. Spectral distribution (a) and light (lux-ampere) characteristic (b) of the photoconductivity of n-InSe crystals with different initial specific resistance (ρ_O) at various intensities of the electric field. T=77 K; ρ_O, Ohm·cm: 1 - $2\cdot10^3$; 2, 3, 4 - $2\cdot10^6$; Φ=0.1;$\Phi_м$; E, V⁄cm: 1, 2 – 50; 3 – 800; 4 – 1500.

It is established that effect of the electric field on photoconductivity in n-InSe crystals more strongly manifests at $U \geq U_{TFL}$, where U_{TFL} – the value of electric voltage at which a full filling of traps in a mode of the space-charge limited currents (SCLC) [10] occurs. In addition, measurements carried out on samples with various current contacts, as well as with various structure and measurement geometry unequivocally testify that in the found out dependence of the intrinsic photoconductivity on external electric field in the investigated semiconductor defining role plays also an injection, since in a case non-galvanic effect of the external electric field on the sample dependence of the photoconductivity on electric field is not observed.

It has appeared that under optimal conditions depending on value of ρ_0, under the effect of the electric field the exponent of pre-linear part of LC changes in

7÷1 limits, the spectrum maximum shifts from 1.10 to 0.95μm, the photoconductivity spectrum narrows from 0.30÷1.45 to 0.35÷1.25 μm and additional maxima on it are not observed. Effect of the external electric field on intrinsic photoconductivity more strongly manifest itself in those crystals in which also effect of photo-memory is considerable [9].

4. DISCUSSION OF THE RESULTS

Going to discussion of the received experimental results, first of all, it is necessary to notice that the dependences of photoconductivity found out by us on the external electric voltage in n-InSe crystals are not connected with a warming up of free charge carriers by electric field [11] and/or other effects of strong electric field [12]. These dependences cannot be also consequence only changes of interaction of free charge carriers with any dot centers (capture centers, trapping levels, recombination centers, etc.) [13]. In favor of this conclusion unequivocally testify such weighty experimental facts as absence of dependence of photoconductivity on electric field at non-galvanic effect of the electric field with intensities up to ~10^4 V/cm, low (far from sufficient for warming up) values of mobility of free charge carriers ($\mu \leq 10$ cm^2/V·s) in high-resistance crystals (in which dependence of photoconductivity on external electric field is observed), memory character of the found out changes (after the termination of the effect of strong electric field sometimes duration of the time for restoration of the initial condition of parameters and characteristics reaches few seconds which considerably exceed time constant, characteristic for carrier-dot centre processes [13]).

Detection of the effect of external electric voltage on photoconductivity in materials just possessing photo-memory property (in those crystals which are partially-disordered [9] and non-equilibrium electronic properties are well described on the basis of two-barrier energy model of the semiconductor [14], having recombination and drift barriers in free bands), under conditions of high injection through current contacts, in the region of weak light intensity and low temperatures unequivocally testify that thus a principal cause of difference of the basic characteristics of photoconductivity for low-resistance and high-resistance crystals is partial disordering of the high-resistance crystals. Owing to what in them besides direct inter-band, under certain conditions takes place also inter-band excitation of the intrinsic photoconductivity assisted by tunneling through recombination barriers. Apparently it is this component of photoconductivity causes displacement of a maximum and long-wave limit of its spectrum to shorter wavelengths, and arisen in near-surface layer recombination barriers lead, first, to spectrum expansion to longer waves, secondly, to occurrence additional weak defined maximum on a short-wave branch of the spectrum. Within a framework of this model it is supposed that at higher galvanically applied external voltages where considerable injection through current contacts takes place, the injected carriers partially compensating volume charges on borders of recombination barriers, reduce their effect on photoconductivity and at such voltages high-resistance crystals on the photoelectric properties come nearer to low-resistance ones. Therefore with growth of U the exponent on pre-linear part of LC gradually decreases, the photoconductivity spectrum narrows, its maximum shifts to short-wave side, and additional peaks on its both shoulders disappear. In favor of the offered model testify also dependences of the spectrum and LC of photoconductivity on ρ_0, detecting their dependence on electric field intensity only at low T and Φ. Most likely, at high T and Φ an electric flattening of the free band potential fluctuation is replaced by a temperature or light flattening.

5. CONCLUSION

Thus, it is possible to conclude that effect of galvanically applied external electric field of high intensity on photoconductivity of high-resistance n-InSe crystals is not connected with electric warming up of the charge carriers and/or other effects of a strong field, but is directly due to the partial disorder of these crystals and an electric flattening of free band potential fluctuation at high injection levels through current contacts.

[1] *F.N. Kaziyev, M.K. Sheynkman, J.B. Yermolovich, G.A. Akhundov*. On photoconductivity of InSe single crystals. Phys. Stat. Solidi, 1969, 31, No 1, p. k59-k61.

[2] *A.M. Filachev, I.I. Taubkin, M.A. Trishenkov*. Solid state photoelectronics. Photodiodes. - M: Fizmatkniga, p. 2011-466 (in Russian). Contemporary state and the main direction of development of solid-state photoelectronics. M. Fizmatkniga. 2010. - 125 p. (in Russian).

[3] *B.T. Kolomiets, S.M. Ryvkin.* Photoelectric properties of indium sulphide and selenide. JTF, 1947, Vol. 17, No 9, p. 987-991 (in Russian).

[4] *A.Sh. Abdinov, Ya.G. Gasanov*. Electrically induced impurity photoconductivity in InSe single crystals with stimulated by electric field negative photoconductivity and residual conductivity. Fiz. i Tech. Poluprovodnikov. 1982. V.16. No 5. PP. 769-772 (in Russian).

[5] *A.Sh. Abdinov, A.G. Kyazymzadeh.* Negative residual photoconductivity and photocurrent quenching in n-InSe at impurity excitation. Fiz. i. Tech. Poluprovodnikov. 1976. V. 10. No1. PP. 81-84 (in Russian).

[6] *A.Sh. Abdinov, R.F. Babayeva, R.M. Rzayev.* Effect of electric field on photoconductivity kinetics of n-InSe single crystals. Neorgan. Material. 2012. V. 48. No 8. PP. 892-896 (in Russian).

[7] *A.M. Huseynov, T.I. Sadikhov.* Production of indium selenide single crystals doped with rare-earth elements. In: Electrophysical properties of semiconductors and gas discharge plasma. Baku. 1989 (Baku, ASU, 1989), p. 42-44 (in Russian).

[8] *A.Sh. Abdinov, R.F. Babayeva.* Effect of switching

in layered $A^{III}B^{VI}$ monoselenides and heterostructures on their basis. Bulletin of the Baku University, Ser. fiz.-math. nauk. 2009. No 3. PP. 139-147 (in Russian).

[9] *A.Sh. Abdinov, A.G. Kyazymzadeh.* The effect of photo- and electro-memory in high-resistance n-InSe single crystals. Fiz. i. Tech. Poluprovodnikov, 1975, V.9. No 9. PP. 1690-1693 (in Russian).

[10] *A.Sh. Abdinov, Ya.G. Gasanov, F.I. Mamedov.* High-resistance single crystals of layered $A^{III}B^{VI}$ compounds. Fiz. i. Tech. Poluprovodnikov., 1982, Vol. 16, No 6, p. 993-998 (in Russian).

[11] *G.A. Akhundov, A.Sh. Abdinov, N.M. Mekhtiyev, A.G. Kyazim-zadeh.* Hot carriers created by a strong electric microwave field in electronic indium selenide. Fiz. i. Tech. Poluprovodnikov., 1974, Vol. 8, No 1, p. 192-195 (in Russian).

[12] *R. Smith. Semiconductors*. (M. Mir, 1991) - 560 p. (in Russian).

[13] *S.M. Ryvkin.* Photoelectric phenomena in semiconductors. M. Science. 1963, 429 p. (in Russian).

[14] *M.K. Sheynkman, A.Ya. Shik.* Long-term relaxation and residual conductivity in semiconductors. Fiz. i. Tech. Poluprovodnikov. 1976, V. 10. No 2. PP. 209-232 (in Russian).

Received: 06.09.2017

INVESTIGATION OF FUNCTIONALIZED MULTIWALLED CARBON NANOTUBES BY DERIVATOGRAPHY METHOD

S.H. ABDULLAYEVA[1,2], S.A. MAMMADOVA[1,2], M.B. HUSEYNOVA[3], A.B.HUSEYNOV[1], A.D. QULIYEV[3], A.O. ISRAFILOV[1]

[1]G.M. Abdullayev Institute of Physics, Azerbaijan ANAS, H.Javid ave. 33, AZ-1143 Baku, Azerbaijan

[2]Research & Development Center for Hi-Technologies (RDCHT), MTCHT, İnşaatchılar ave. 2, Az-1073, Baku, Azerbaijan

[3]Institute of petrochemical processes named after Y. Mammadaliyev, Azerbaijan NAS, Khojaly ave. 30, AZ - 1025, Baku, Azerbaijan

E-mail: asker.huseynov@rambler.ru

The thermal stability characteristics of multiwalled carbon nanotubes (MWCNTs) functionalized via introduction of oxygen containing groups were investigated by derivatography method. MWCNTs were synthesized for the first time from the light gasoline fraction of the Azerbaijan oil. MWCNTs were chemically functionalized by using sulfuric and nitric acid. IR spectroscopy analysis has confirmed the presence of oxygen containing (COOH, COH, OH) and other functional groups on the surface of the MWCNTs. SEM analysis has displayed that the structure of MWCNTs has curved shapes and surface is covered with layers of non-tubular forms of carbon. According to Termogravitmetric (TGA) and Differential Scannic Calorimetry (DSC) analysis results, f-MWCNTs are thermally stable up to 350^{0}C. At the 350-600^{0}C temperature range was observed the cleavage of carbonyl and carboxyl groups, as well as the oxidation of amorphous carbon with the release of CO, CO2 ,water vapor and MWCNTs combusted at about 600^{0}C in air.

Keywords: Aerosol CVD, MWCNT, oxidative functionalization, thermal stability, TGA, DSC, FTIR, Mass Spectrometry, SEM.
PACS: 61.48.De, 81.65.Mq

1. INTRODUCTION

Carbon nanotubes (CNTs), discovered more than two and a half decades ago by the Japanese scientist Sumio Iijima [1]. Due to their unique structural (tubular structure with an hollow interior) and physicochemical (mechanical, electrical, optical, etc.) properties they are very essential nanomaterials and have a wide range of potential applications in various areas of science and technology [2,3], particularly in medicine, electronics, catalysis, materials science (sensitive elements of different types of sensors, new generation nanocomposites for various purposes, energy (the hydrogen storage, the solar battery elements) and etc [4,5].

Thermal stability of pristine and modified MWCNTs at high temperatures and oxidizing environments is crucial for high - temperature applications of materials based on carbon nanotubes, especially polymer composite materials, catalysts, etc. [6,7] In this regard, a number of research works were devoted to the study of thermal stability and thermodestruction of nanostructured carbon materials at high temperatures, in particular single-walled and multi-walled carbon nanotubes in air or in the inert gas environments (argon and others) [8-19].

In this paper, the thermal stability of the f- MWCNTs with oxygen containing groups has been studied by the derivatography method companied by FT-IR and Mass spectroscopy. TGA / DSC analysis were carried out in the temperature range of 30 - 1000 ^{0}Cin air at a furnace heating rate of 10 deg / min. The obtained results of thermal stability with declared methods showed a good agreement with each other.

2. EXPERIMENTAL

2.1. Synthesis of MWCNTs by ACVD method

The MWCNTs used in this work were synthesized by an Aerosol Chemical Vapor Deposition Technique (ACVD) on the experimental laboratory setup Scientific Instruments Dresden GMBH, SCIDRE, Germany.

The aerosol CVD set - up equipped with a gas flow regulator and flue gases lines consists of the following key modules: carrier gas supply units (Inlet 1-3), ultrasonic aerosol generator (2), high temperature reactor, electric furnace (heating up to 1200^{0}C) (3) and the vacuum system (leak test of the setup).The high - temperature reactor, in turn, consists of a quartz tube (4) placed in a tubular furnace. The tubular furnace is additionally equipped with a mechanism for moving along the quartz tube at a predetermined rate, which allows the thermolysis of the hydrocarbon mixture and the synthesis of carbon nanotubes along the entire length of the tube.

Synthesis process was carried out at a 900^{0}C temperature. A light gasoline fraction of the Azerbaijan oil was used as a raw material and ferrocene (Fc) as a catalyst precursor . A chemical quartz glass with a capacity of 200 ml containing a solution of ferrocene in gasoline with a quantitative ratio of 20 mg / ml was placed in the ultrasonic bath of the aerosol generator of the CVD equipment. A more detailed description of the experimental setup and the standard procedure of the ACVD are presented in the work [20].

The obtained MWCNTs were purified from by-products (impurity inclusions of the iron catalyst, resinous substances) by widely known methods [21].

131 H.Javid ave, AZ-1143, Baku
ANAS, G.M.Abdullayev Institute of Physics
E-mail: jophphysics@gmail.com

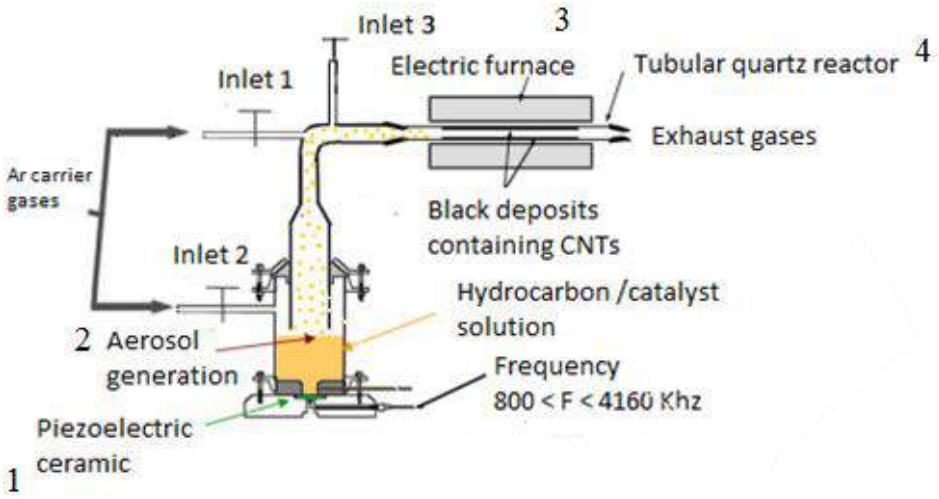

Fig.1. Schematic diagram of ACVD apparatus.

The purification process of MWCNTs from tarry compounds was carried out as a result of extraction using xylene and cyclohexane as solvents in a volume - weight ratio (ml / g) of 30: 1 by heating the nanotubes suspension to T = 80 ^{0}C and continuously mixing.During the heating process, the dispersion of carbon nanotubes acquired a yellowish color, which indicated the presence of tarry impurities. This procedure was repeated several times with small fresh portions of xylene until the solution was completely discolored and completeness removed the resinous products. Subsequently MWCNTs were purified from the catalytic iron (Fe) particles, with dilute nitric acid (28% HNO_3) treatment at a temperature 80 ^{0}C for 2 hours and with constant stirring followed by washing the carbon nanotubes with deionized water to remove the acid and formed nitrogen-containing iron salts.

2.2. Functionalization of the MWCNTs

Surface functionalization of synthesized MWCNTs with oxygen containing groups (COOH, COH, OH) were carried out involving a strong oxidative treatment using the mixture of concentrated sulfuric and nitric acids in a volume ratio (ml / ml) equal to 1: 3 [21].

Purified MWCNTs were placed into a 500 ml glass beaker and 13.5 ml of HNO_3 and 40 ml of H_2SO_4, were alternately poured and this mass was heated on a hot plate for 120 minutes at a 80^{0}C temperature with constant stirring. After treatmen tthe residual acid solution was filtered and repeatedly washed. The oxidized MWCNTs were rinsed with deionized water until stabilization of the filtrate pH. The resulting functionalized product (f-MWCNTs) was dried in an oven at 130 ^{0}C for an hour.

2.3. Scanning electron microscopy (SEM)

The morphology of the functionalized MWCNTs was investigated by scanning electron microscopy using a CarleZeiss device (SigmaVP). The image was obtained at an accelerating voltage of 5.00 kV.

2.4. Fourier Transform Infrared (FTIR) Spectroscopy

Fourier transform infrared (FTIR) studies were carried out in the range 450 - 4000 cm $^{-1}$ to study the attachment of oxygen containing groups on carbon nanotubes surface using Nicolet IS 10 FTIR spectrometr. Resolution - the error of the spectrophotometer according to the scale of wave numbers was - 0.4 cm $^{-1}$.

2.5. Thermal analysis of f-MWCNTs

The thermal decomposition behavior of the f- MWCNTs was studied by TGA/ DSC spectroscopy. Measurements were carried out in derivatograph of the Linseis Corporation company "STA Platinum Series" type - "LINSEIS STA PT1600" coupled with the FTIR Nicolet IS10 spectrometer and the ThermoStar TM GSD 320 T2 mass analyzer .The DTA study, which combines the use of TGA and DSCwas performed in air purging through the derivatograph chamber in the mode of dynamic programmable heating in a temperature range of 30-1000 ^{0}C with a continuous rate of temperature rise in the furnace 10 deg / min. The procedure involved weighing a sample with a mass of 16.6 mg in a cylindrical ceramic crucible, followed by annealing of o - MWCNTs in an oxidizing air atmosphere. The products produced with increasing temperature as a result of thermodestructive transformations of the sample were studied through curves of weight loss (TGA) and thermal effects (DSC), as well as on IR and mass spectra of the resulting compounds, simultaneously – "in situ" entering on appropriate devices.

3. RESULTS AND DISCUSSION

3.1. SEM characterization of f-MWCNTs

The SEM image of f-MWCNTs is presented in Fig. 2. It is determined that the diameter of carbon nanotubes varies within 120 - 288 nm.

SEM micrographs reveal that the tubular structures of nanotubes curved and also contain layers of other carbon phases which explain the excess of the diameter of the f-MWCNTs. The presence of a large number of impurities of non - tubular carbon forms are attributed to the raw material- a mixture of carbon compounds – a light gasoline fraction of Azerbaijan oil.

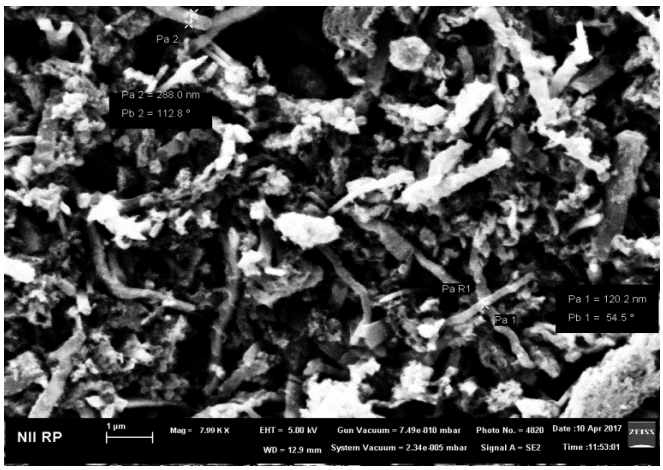

Fig. 2. SEM images of the f-MWCNTs.

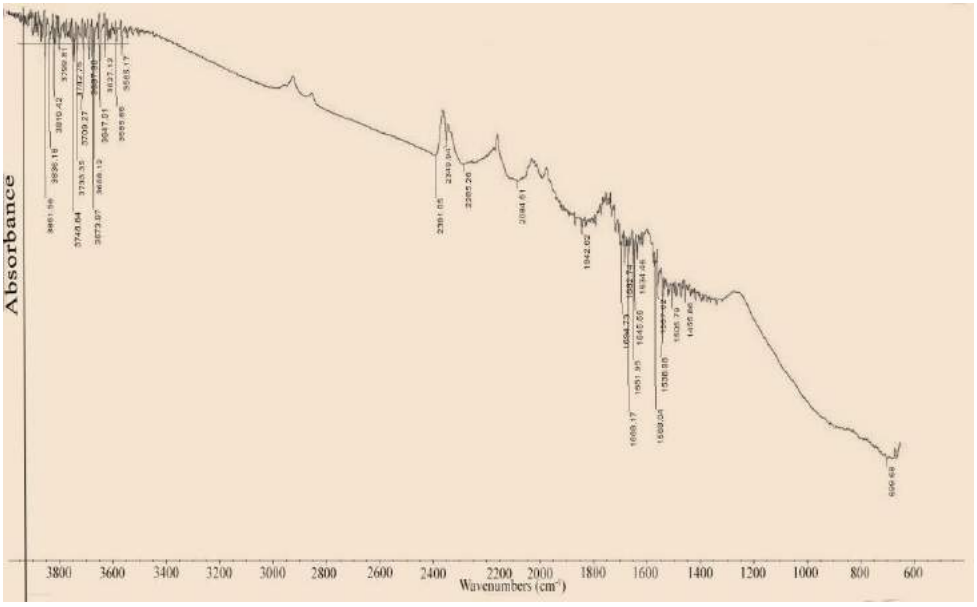

Fig 3. FTIR spectrum of f-MWCNTs

3.2. FTIR analysis of f-MWCNTs.

The FTIR spectra of the f- MWCNTs are shown in Fig.3. FTIR is used to characterize the functional elements absorbed by carbon nanotubes.

FTIR of the f-MWCNTs shows dominant peaks in the region 3946-3585cm^{-1} which can be related to the valence vibrations of the associated hydroxyl (OH) functional groups in carboxyl (O=C-OH).The absorption bands recorded in the 3565.17 - 3460.41 cm^{-1} regions are characterized as the possible presence of adsorbed atmospheric moisture (H_2O) and free (non - hydrogen-bonded) hydroxyl functional groups. The appearance of a narrow peak at a 2391.05 cm^{-1} is due to the stretching vibrations of O – H bonds in the carboxyl group of COOH is strongly bounded by hydrogen bonds, while the peak fixed at 2349.94 cm^{-1} is inherent in the carbon dioxide CO_2 molecule.

The presence of sharp adsorption peaks in the 1634.46 - 1694.73 cm $^{-1}$, range respectively, is explained by the stretching vibration of the C = O bond of the carbonyl group of carboxyl (COOH) or keto group of the quinone type.

In the IR spectrum of the f-MWCNTs also was observed a series of characteristic absorption bands in the frequency range 1455.86-1568.04 cm^{-1}, which correspond to the stretching vibrations of the conjugated C = C bonds of the skeleton of carbon nanotubes.

The FTIR results proved that treatment of MWCNTs with mixture of acid salution caused introduction of different number of oxygenated acidic groups on the carbon surface.

3.3. TGA/DSC analysis of f-MWCNTs.

The thermal decomposition of f – MWCNTs has been studied by TGA/DSC analysis. TG and DSC curves of MWCNTs conducted in air are depicted in Fig. 4.

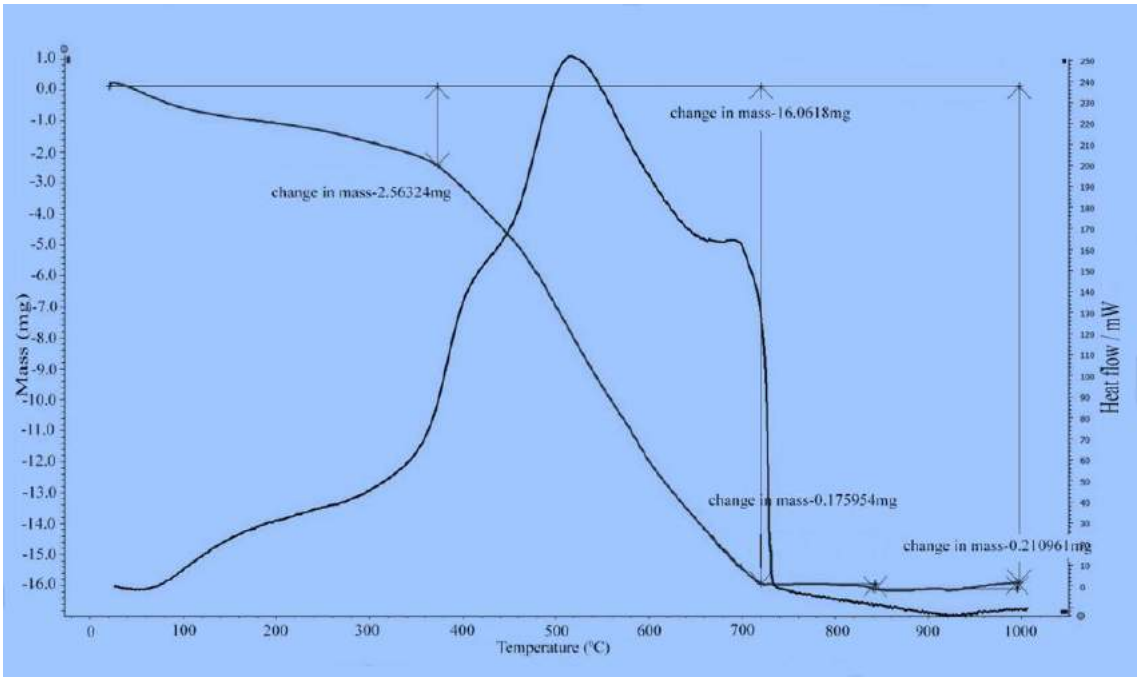

Fig. 4. TGA/DSC analysis of f-MWCNTs

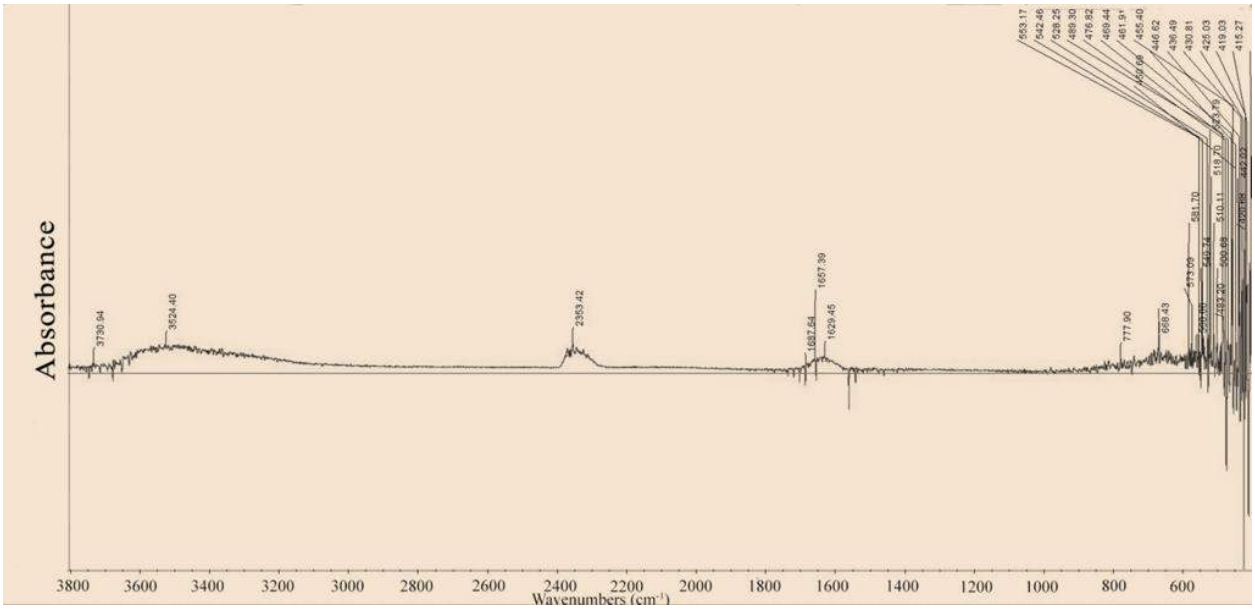

Fig.5. FTIR spectrum of gaseous products of the oxidation-thermal destruction process of f- MWCNTs at 370 ^{0}C.

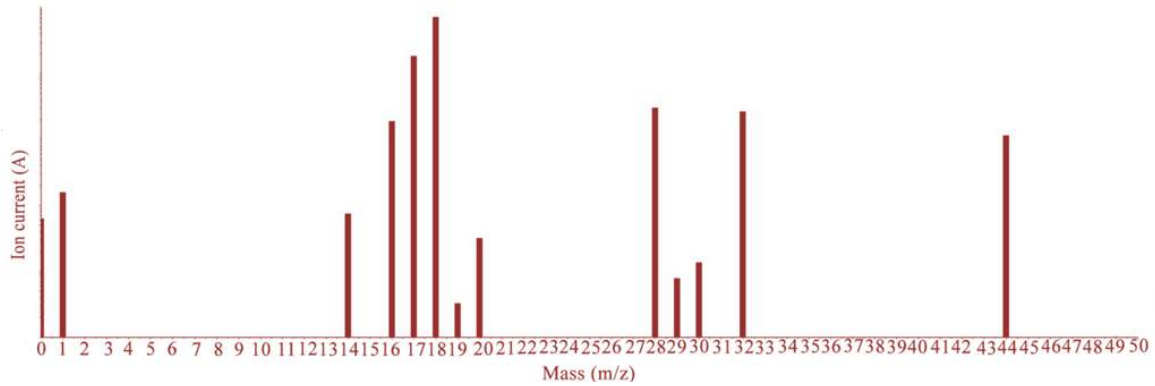

Fig . 6. Mass spectrum of gaseous products of the oxidation-thermal destruction process of the f - MWCNTs sample at 370 ^{0}C.

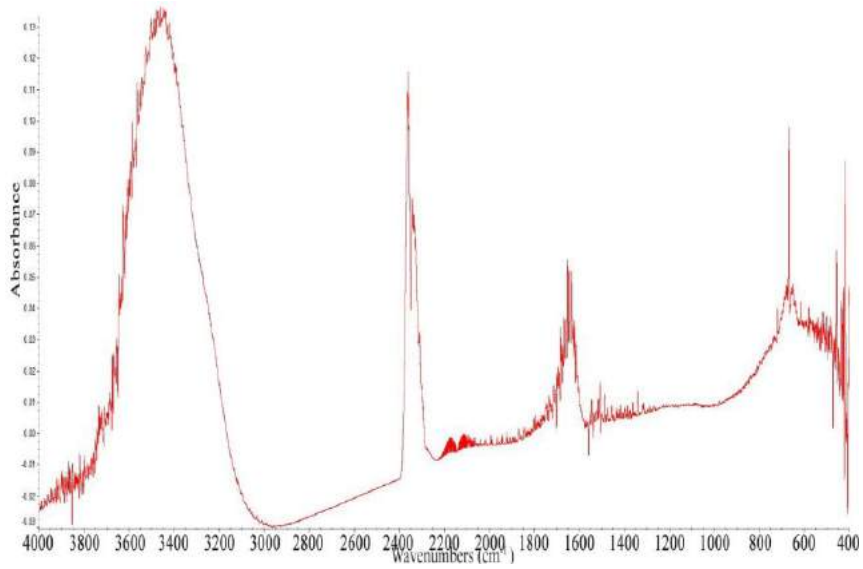

Fig.7. FTIR spectrum of gaseous products of the oxidation-thermal decomposition process of the f– MWCNTs at 500 ^{0}C.

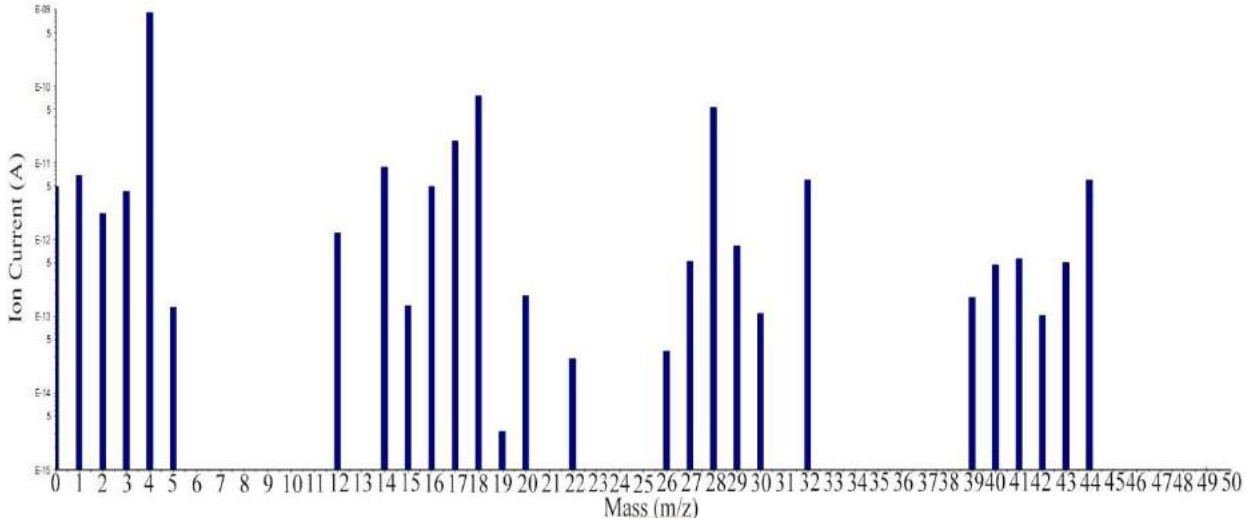

Fig.8. Mass spectrum of gaseous products of the oxidation-thermal decomposition process of the f- MWCNTs at 500 ^{0}C

Reduction in weight in the temperature range 470-600^{0}C is accompanied by a corresponding exothermic effect (T = 400-650^{0}C), which is clearly appeared in the form of a wide pronounced peak on the DSC curve with a maximum at 520^{0}C, indicating that weight loss is due not only by defunctionalization, as well as deep oxidation. At these temperatures both dehydration processes and oxidation of unstructured (amorphous) forms of carbon are taking place. This result is also confirmed by the infrared spectrum of the decay products of the f - MWCNTs at 500 ^{0}C, where very intense peaks at 3500 cm^{-1} and 2200 - 2440 cm^{-1} are distinctly registered, that respond to the existence of water molecules, monoxide and carbon dioxide, accordingly, generated owing to the thermo-oxidative destruction of carbonyl, carboxyl groups and destructive oxidation of carbon. In the mass spectrum, peaks with masses of 16, 28 and 44 amu are also observed, indicating the presence of $^-$OH anions and CO and CO_2 molecules (Fig. 7,8).

Finally, the weight loss in the (600 – 735)^{0}C temperature range and appropriate maximum at 700 ^{0}C in DSC curve can be explained by the oxidation of the more active phase (impurity inclusions of amorphous carbon), also the combustion of pristine carbon nanotubes, which is in good agreement with FTIR and MS analyzes. Thus, in the IR spectrum of the vapors at a temperature of 600^{0}C, adsorption bands were observed with wave numbers of 2250 and 2350 cm^{-1} which corresponds to decomposition of a large number of carbon oxides (CO and CO_2, respectively) and is consistent with the results of the mass spectroscopy. In addition, there is no peak in the IR spectrum responsible for the presence of C=C bonds of the structure of carbon nanotubes, which indicates the degradation of the skeleton of MWCNTs. The weight loss of the sample as a result of the oxidation - thermal reaction was 16.06 mg (Fig. 9, 10).

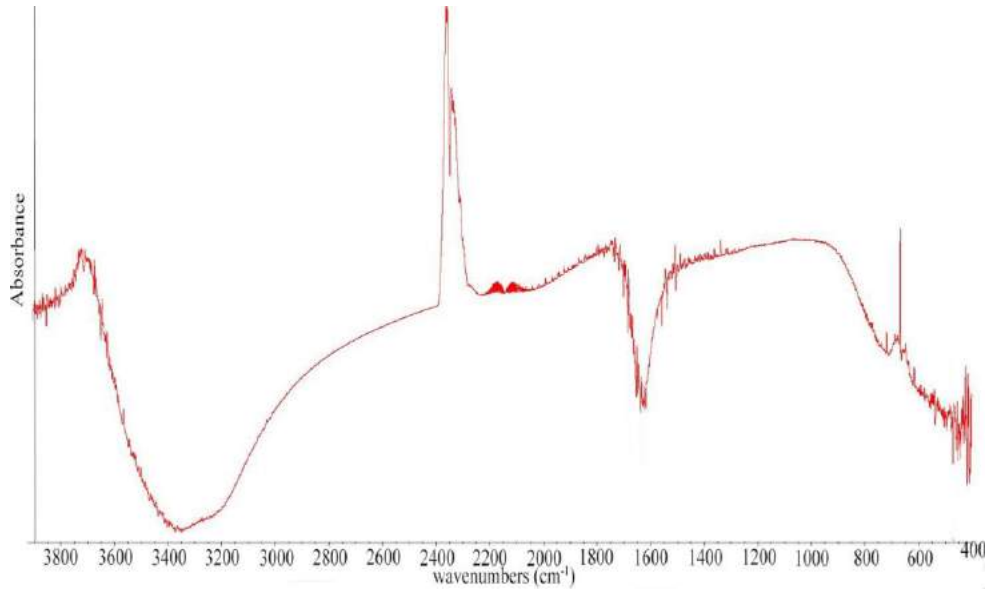

Fig. 9. FTIR spectrum of gaseous products of the oxidation-thermal decomposition process of the f - MWCNTs sample at 600 ^{0}C.

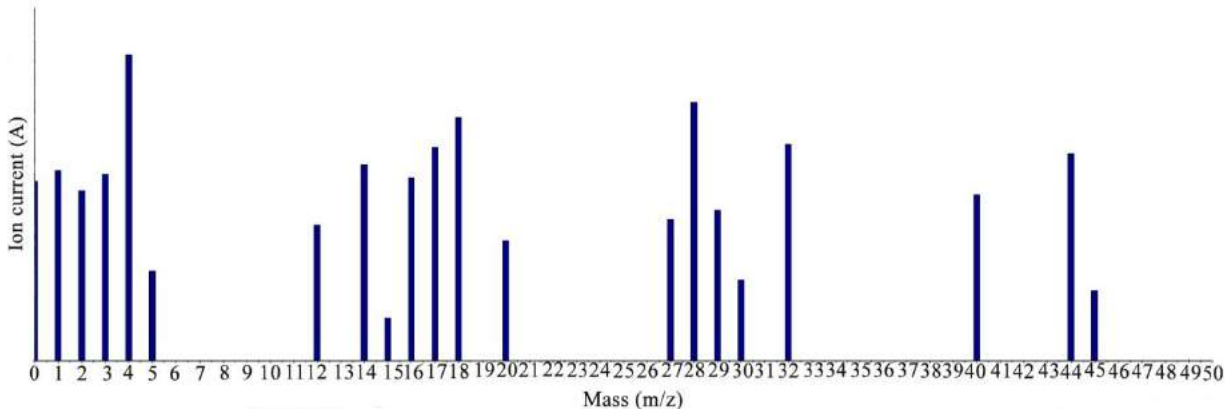

Fig.10. Mass spectrum of gaseous products of the oxidation-thermal decomposition process of the f - MWCNTs sample at 600^{0}C.

CONCLUSIONS

Multiwalled carbon nanotubes (MWCNTs) have been synthesized by ACVD method using for the first time as an inexpensive and affordable raw material – the light gasoline fraction of the Azerbaijan oil. Side-wall functionalization of MWCNTs with oxygen containing groups (COOH, COH, OH) was achieved by oxidative treatment. The IR spectra for the f-MWCNTs identified the characteristic stretching peaks for the successful linkage between MWCNTs and carbonyl, carboxyl and hydroxyl groups. The character of the thermal decomposition of f - MWCNTs in air was studied by derivatography method based on the indices of mass loss of samples and endo/exo effects in the temperature range from 350 to 735^{0}C. It was revealed that in the 350 - 470^{0}C temperature range decarboxylation and in the 470 - 600^{0}C region dehydration and the oxidation of unstructured forms of carbon were observed. FTIR analysis results confirmed that at 600^{0}C combustion of f - MWCNTs occurred as in 1650 - 1500 cm^{-1} region there weren't any peaks observed inherent in the C=C bond of the framework of carbon nanotubes.

[1] *M. Endo, S. Iijima.* Carbon nanotubes. Journal of Physics and Chemistry of Solids. Elsevier Science Limited. 1996, pp. 1.

[2] *D.M. Guldi, N. Martin.* Carbon Nanotubes and Related Structures. WILEY-VCH Verlag GmbH & CoKGaA. 2010, pp. 1- 3.

[3] *M. J. O'Connell.* Carbon Nanotubes Properties and Applications. Taylor & Francis Group. 2006, pp. 3-5.

[4] *J.R. Stetter, G.J. Maclay.* Carbon nanotubes and sensors: a Review. Advanced Micro and Nanosystems. 2004. Vol. 1, pp. 358-359.

[5] *Jun Zhang, Yan-Ling Luo, Feng Xu, Ya-Shao Chen.* Novel poly (N-vinylcarbazole) grafted multi - walled carbon nanotube nanocomposites based on a nucleophilic reaction: Synthesis, fabrication of thin films, and sensing properties. Chemical Engineering Journal. 2016, pp. 3 - 5.

[6] *F. Xu L, X. Sun, J. Zhang, Y. N. Qi, L. N. Yang et al.* Thermal stability of carbon nanotubes. J Therm Anal Calorim. 2010, 102:785 - 791, pp. 785 - 786.

[7] *Q. Wu, J. Bao, C. Zhang et al.* The effect of thermal stability of carbon nanotubes on the flame retardancy of epoxy and bismaleimide carbon fiber buckypaper composites. J Therm Anal Calorim. 2011, 103:237 – 242. pp. 237 - 241.

[8] *D.D. Ezekiel, B. Nolukhanyo.* Carbon Nanotubes Synthesis by Catalytic Decomposition of Ethyne Using Fe/Ni Catalyst on Aluminium Oxide Support. International Journal of Applied Chemistry. Vol. 9, № 1, pp. 35 - 42.

[9] *V. Datsyuk, M. Kalyva, K. Papagelis, J. Parthenios et al.* Chemical oxidation of multiwalled carbon nanotubes. Carbon. 2008, Vol. 46. pp. 833 – 840.

[10] *V. Likodimos, A.S. Theodore, K.P. Sergios, G.Em Romanos, R.R.N. Marques et al.* Controlled surface functionalization of multiwall carbon nanotubes by HNO_3 hydrothermal oxidation. Carbon. 2014, Vol. 69, pp. 311 - 326.

[11] *G.E. Romanos, V. Likodimos, R.R.N. Marques, A.S. Theodore, K.P. Sergios et al.* Controlling and Quantifying Oxygen Functionalities on Hydrothermally and Thermally Treated Single-Wall Carbon Nanotubes. J. Phys. Chem. 2011, Vol.115, pp. 8534 - 8546.

[12] *S. Sadia, I. Nadeem, M. Asghari et al*. Dielectric, electric and thermal properties of carboxylic functionalized multiwalled carbon nanotubes impregnated polydimethylsiloxane nanocomposites. 6th. Vacuum and Surface Sciences Conference of Asia and Australia (VASSCAA-6). Journal of Physics: Conference Series. 439 (2013) 012024.

[13] *T.P. Dyachkova, A.V. Melezhyk, S.Yu. Gorsky et.al.* Some aspects of functionalization and modification of carbon nanomaterials. Nanosystems: Physics, Chemistry, Mathematics. 2013, Vol. 4, № 5, pp. 605 - 621.

[14] *Chiang Yu-Chun, Lin Wei-Hsiang, Chang Yung-Chia.* The influence of treatment duration on multi-walled carbon nanotubes functionalized by H_2SO_4 / HNO_3 oxidation. Applied Surface Science. 2011, Vol. 257, pp. 2401 - 2410.

[15] *L.P. Desirée, M.R. Christopher, M.G. Philip.* Thermogravimetry − Mass Spectrometry for Carbon Nanotube Detection in Complex Mixtures. Environ. Sci. Technol. 2012, Vol. 46, pp. 12254 - 12261.

[16] *N.V. Glebova, A.A. Nechitailov.* The functionalization of the surface of multi - walled carbon nanotubes (In Russian). Pisma v JTF. 2010, Vol. 36, № 19, pp. 12 -15.

[17] *H.H. Salameh, V.P. Shelohvostov et al.* Investigation of products of pyrolytic synthesis of carbon materials (In Russian). Vestnik TQU. Vol. 15, № 1, pp. 238 - 239.

[18] *A. Mahajanetal, A.Kingon, A. Kukovecz et al.* Studies on the thermal decomposition of multiwall carbon nanotubes under different atmospheres. Materials Letters. Vol. 90, pp. 165 - 168.

[19] *Z. Luo, A. Oki, L. Carson, L. Adams, G.Neelgund, N. Soboyejo et al.* Thermal stability of functionalized carbon nanotubes studied by in situ transmission electron microscopy. Chemical Physics Letters. 2011, Vol. 513, pp. 88 – 93.

[20] *S. Abdullayeva, N. Musayeva, C. Frigeri, A. Huseynov et al.* Characterization of high quality carbon nanotubes synthesized via Aerosol – CVD. Journal of Advances in Physics. 2015. Vol .11, № 4, pp. 3229-3237.

[21] *S. G.M. Nicolas, R.F. Esteban, A.Y. S.G Suarez.et al.* Surface modification of multiwall carbon nanotubes by sulfonitric treatment. Applied Surface Science http://dx.doi.org/10.1016/j.apsusc.2016.04.065.2016.

Recevied: 14.06.2017

THE PEPTIDE CONFORMATION ANALYSES REGULATING THE CATECHOLAMINE SYNTHESIS PROCESSES

L.I. VELIYEVA, E.Z. ALIYEV
Baku State University
AZ-1148, Z. Khalilov str., 23, Baku, Azerbaijan

The spatial structure and mobility of side chains of proline-containing peptide are studied by the method of theoretical conformational analysis. The influence of side chains on formation of peptide spatial structure is analyzed on the calculation result.

Keywords: neuropeptides; structure; conformation analysis
PACS: 87.80.-y

INTRODUCTION

The proline-containing peptide (PR-peptide) is related to number of compounds regulating the processes of synthesis, secretion and reception of catecholamine, firstly isolated from neurosecretory granules of bull hypothesis [1]. It is known that many low-molecular peptide compounds containing the proline residuals along with ferment inhibition influence on central nervous system (CNS), increase the hormone concentration in blood, cause antibacterial action and other effects [2,4]. The peptide specific spatial organization in formation and stabilization of which the molecule chemical structure plays the important role, is on the base of wide range of such peptide biochemical properties. The spatial organization of PR-peptide, the chemical structure of which contains the proline four residuals is studied in the given work by the method of theoretical conformation analysis. The presence of proline in peptide chain causes the significant limits of frame conformation mobility [2]. That's why the mobility of side chains of amino-acid residuals is studied and their role in formation of PR-peptide spatial organization is revealed along with establishment of set of peptide low-energy conformation states. The investigations are carried out by the technique described in [4,5] and they include the step-by-step study of fragment conformation states and their overlapping sections (fig.1).

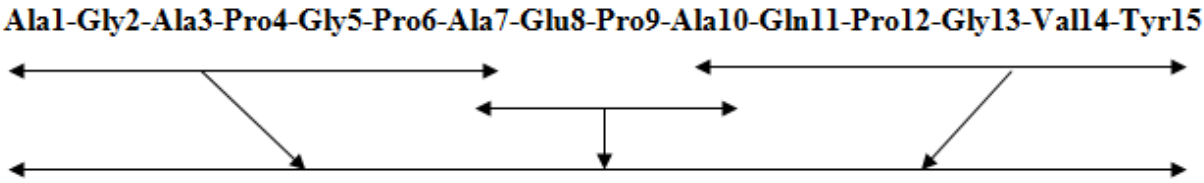

Fig.1. The calculation scheme of PR-peptide.

RESULTS AND CALCULATIONS

Ala1-Ala7 fragment

According to calculation results Ala1- Gly2-Ala3 fragment of PR-peptide of peptide chain is presented by big number of low-energy conformation states (~20). They are related to all admissible shapes of three-peptide frame with equal probability, i.e. can form the both wrapped and unwrapped forms of peptide chain. The summary contribution from energy of dipeptide interactions in first case is ~-3kkal/mol, in second case is ~2,2 kcal/mol. Pro4-Gly5-Pro6 section forms the identical conformation states belonging mainly to ff shape (90% of all admissible structures) in investigated fragment. In many low-energy conformations Pro4 is in R frame shape (83%) whereas Pro6 can be in both R and B shapes (43% and 57% correspondingly). The dipeptide interactions between Gly5 and Pro6 9-2,8 kcal/mol are the main stabilizing factor in the given section. The formation of β-bend in Ala3-Pro4-Gly5-Pro6 section is the character for Ala1-Ala7 fragment. The distance between C^{α} atoms of Ala3 and Pro6(≤6,2 Å) is the general criterion.

Ala7-Ala10 fragment

Only B and L forms of proline main chain are permitted for Glu8 because of steric collisions of ionized side chain of glutaminic acid with γ-methylene group of proline pyrrolidine ring. Alanine can be in R, B and L sections of conformation space. That's why the general number of initial variants for procedure of minimization of total conformation energy is 18. They describe the all possible forms and shapes of fragment peptide frame. The calculation results show on preference of two shape types fef and fee the each of which contains 9 conformations with relative energy ≤ 6 kcal/mol. The dipeptide interactions between Glu8 and Pro9 (on the average ~3,3 kcal/mol) make the big contribution in stabilization of all low-energy structures.

131 H.Javid ave, AZ-1143, Baku
ANAS, G.M.Abdullayev Institute of Physics
E-mail: jophphysics@gmail.com

Table 1.

Low-energy conformations of RP-peptide.

№	Ala1-Gly2-Ala3-Pro4-Gly5-Pro6-Ala7-Glu8-Pro9-Ala10-Gln11-Pro12-Gly13-Val14-Tyr15	Number of conformations in shape	Relative energy interval, kkal/mol	The distance between C^{α} atoms of amino-acid residuals, Å
1	eee / efe / fee / ffe → ff → efef → ee → fff	1	0	Ala1- Pro9 (5,2) Ala10-Tyr15 (6,7)
2		1	4,3	Ala1- Glu8 (5,8) Ala10-Tyr15 (6,7)
3		1	6,7	Ala1- Pro4 (4,5) Ala10-Tyr15 (6,7)
4		7	2,1-9,9	Ala1- Glu8 (5,2) Ala1-Tyr15 (6,7)
5	eee / ffe / fee / efe → ff → efee → ee → fff	4	5,7-8,9	Ala1- Pro9 (5,9) Ala10-Tyr15 (6,7)
6		11	6,3-10	Ala1- Glu8 (6,7) Pro9-Tyr15 (6,3)
7		1	9,5	Ala1-Tyr15 (6,7)
8		1	9,8	Ala1- Glu8 (5,8) Pro9-Tyr15 (6,4)
9	fee / eee → ff → ffef → ee → fff	2	7,1-7,5	Ala1-Tyr15 (6,3)
10		1	7,5	Ala1- Ala7 (6,5) Ala10-Tyr15 (6,7)

Ala10-Tyr15 fragment

Only L and B sections of conformation space are sterically permitted near proline residual as in the case of previous fragment Gln11. The general number of initial approximations for minimization procedure of conformation energy is 126 variants belonging to 8 shapes of peptide frames. As it follows from calculation results Pro12-Tyr15 section forms the totally wrapped structures (shape fff) for all admissible conformations on fragment (relative energy varies in interval 0-5kcal/mol). Pro12 realizes only R shape of peptide frame (in difference from Pro6 for which R and B frame shapes are practically similar) in all calculated conformations. The stabilizing contribution in formation of these structures make the influences between Gln11 and following residuals of peptide chain Pro12, Val14, Tyr15 (-3,5; -3,3 and -2,9 kcal/mol, correspondingly). The formation of β-bend on Gln11-Val14 section is character for fragment that is shown by the distance between C^{α} atoms Gln11 and Val14 (~6,5 Å). Gly13 is in the top of such bend.

Conformation states of PR-peptide.

The conformation calculations are carried out for 778 initial approximations on the base of combinations of low-energy fragment states (fig.1). According to investigation results (table 1) in spatial organization of PR-peptide we can emphasize the two conformationally elastic sections: Ala3-Pro4-Gly5-Pro6 and Ala10- Tyr15 fragments including β-bend conformations. Ala1-Pro9 section also forms the wrapped structure in which the closeness of C^{α} atoms of Ala1 and Gln8, Pro9 residuals varies in limit 5,2-6,7Å. As it is seen from the calculations the side chains of all amino-acid residuals are on the surface of compact structures and are oriented in environment.

CONCLUSION

Generalizing the investigation results we can form the following conclusions:

1. The native conformation of PR-peptide can be presented by the structure containing β-rotations on two tetrapeptide sections Ala3-Pro6 and Gln11-Val14 (all of them are satisfy to condition C_i^{α}-$_{Ci+1}^{\alpha}$, C_{i+2}^{α}, $C_{i+3}^{\alpha} \leq 60°$).
2. Ala7-Glu8-Pro9-Ala10 section is conformationally mobile and can realize the set of low-energy states. The side chain of Glu8 residual is oriented in environment and can participate in realization of intermolecular interaction.

[1] *M.F. Minocva et al.* Journal of Neurochemistry, 1999, vol.73, p.1154

[2] *E.M. Popov.* V kn. «Strukurnaya orqanizasiya belkov», M. «Nauka», 1989, 352 s. (In Russian).

[3] *G.I. Chipens, L.K. Polevaya, M. Veretennikova, A.Yu. Krikis.* Vkn. «Struktura i funkchii nizkomolekulyarnix peptidov», Riqa, Zinatie, 1980, 328 s. (In Russian).

[4] *I.N. Alieva, L.I. Veliyeva, D.I. Aliev, N.M. Godjaev.* Journal of Peptide Science, vol. 8, 2002, p.385-397.

[5] *L.I. Veliyeva, I.N. Alieva, M.A. Musayev, N.M. Godjaev.* Protein and Peptide Letters, 2006, vol.13, n.10, p.1007-1015.

Received: 12.06.2017

DIELECTRIC PROPERTIES OF HDPE-CdS/ZnS COMPOSITES

E.G. HAJIEVA, A.M. MAHARRAMOV, M.M. GULIYEV, R.S. ISMAYILOVA
Institute of Radiation Problems of Azerbaijan NAS
Str. B.Vagabzade 9, Baku, Azerbaijan

Ternary high density polyethylene/cadmium sulphide /zincsulphide (HDPE- CdS/ZnS) were fabricated using hot pressing the powder mixture technique. The dielectric behavior of such composites over a wide temperature (from 25 to 130^0C) and frequency (from 25 to $1{\cdot}10^6$Hz) ranges was studied using broadband dielectric spectroscopy.

Keywords: composite, dielectric permittivity, cadmium sulfide/zinc-sulfide, dielectric loses, filler, frequency.
PACS: 72.80.Tm, 77.22

1. INTRODUCTION

Semiconductor/polymer composites have been extensively investigated during the last four decade due to their improved performance and potential applications. Potential areas of application of composite materials include micro-and nanoelectronics, low voltage flat panel, sensors, photovoltaic devices, light emitting devices etc.[1-3]. Micro- and nanocomposite materials have attracted attention in both fundamental studies as well as technical applications. The polymers are widely used in the technology of preparation of composite materials in the quality of matrix that serves for assembling the micro- and nanoparticles into clusters and for avoiding the agglomeration, as a matrix in self-assembling materials that induce ordering and anisotropic orientation, as well as acting as a functional element [4]. The field of dispersing semiconducting micro-and nanoparticles within a polymer matrix is of sufficient interest because of the possibility of producing polymer composite based devices which can be processed in required geometries, morphologies and composition with consequent control over the different electro-optical properties.

Studies on synthesis and physical properties of different polymer based composite have been reported by many researchers such as polyvinylchloride (PVC)/CdS [5], LDPE/CdS [6], PVC/ZnO [7], copolymer of vinylidene fluoride and tetrafluoroethylene F42/CdS/ZnS and polyvinyldene floride F2/CdS/ZnS [8], polyamine (PANI)/CdS/ZnS [9,10], polyvinyl-alcohol (PVA)/CdS [11], poly(methyl methacrylate) PMMA/CdS [12], ect. It has been observed that the incorporation of micro-and nanoparticles into polymer improves the thermal stability, glass transition temperature, specific heat and mechanical properties. Several researches have shown that along with thermal stability electrical conductivity of the polymers plays important role to modify the polymer properties to be used for advanced applications [1].

Among the polymers, high density polyethylene (HDPE) is one of the most common and popular thermoplastic polymers having the characteristic like low price, excellent electric insulation and good reproducibility.

The quantum confinement of electrons and photons inorganic semiconductor particles used in the composites exhibit physical and chemical properties which are different from the properties of corresponding bulk materials. Among various inorganic semiconductors CdS/Zn Shave received great attention because of their attractive properties and potential for application in photonics and optoelectronics. Further investigation of the polymer-based composites are equally important for understanding the mechanism of transport and photoluminescence in the materials, developing of materials with advanced characteristics, as well as for possible minimizing the toxicity of Cd-based materials.

A.F.Gochuyeva et al. [8] was found a possible mexanism of photoelectret effect to be formed at the same time under the impact of strong electric field and lights is offered in the composites based on polar (fluoride-containing) and non-polar (polyolefins) polymers and inorganic semiconductors CdS/ZnS. It was found that the polarity of the polymer matrix is mainly dependent on the potential difference of photoelectret inorganic phase at predetermined volumetric content.

Studies on PANI-CdS and PANI-ZnS nanocomposites have been reported in [9,10]. In [9] authors report about details of comparative studies on electrical properties of PANI/ZnS nanocomposite at different weight % of ZnS. The increase conductivity in 25% nanocomposite is attributed to polymer chain mobility and activation of dopant. S.D.Bompilwar et al. [10] shows that as the weight percentage of CdS/ZnS nanoparticles increases in the polyanilene (PANI) matrix, half decomposition temperature increases gradually and activation energy also increases. These results indicate that the polymer composites are thermally more stable as compared to that of pure PANI. In [13] A.Shik et al. considers photoelectric phenomena in a composite medium in which inclusions from o type –II heterojunction with a host matrix. The model describes, in particular, polymer-based photosensitive structures with different types of semiconducting or inclusions. It was shown that the separation on no equilibrium carriers due to interface electric fields increases the hole component of photoconductivity, decreases the electron component, and results in a substantial increase of the total photoconductivity. In this work authors considered the theory of this effect in detail, elucidate its general features, and determine its influence on the properties of composite based photoconductors and photodiodes.

In this paper we report the study of a HDPE - CdS/ZnS composite system, were distributed at random in the continuous polymer phase to form a 0-3 type of connectivity.

131 H.Javid ave, AZ-1143, Baku
ANAS, G.M.Abdullayev Institute of Physics
E-mail: jophphysics@gmail.com

2. EXPERIMENTAL

1. Materials.

The matrix polymer used in this work is a commercial white powder high density polyethylene (HDPE) with particle sizes in the range of 150-200μm. The various physical parameters of HDPE are as follows: density 958kg/m^3, melting temperature =150^{0}C, dielectric constant at 1 kHz = 2.4, dissipation factor at 1kHz =0.0066 and volume resistivity = 5·10^{13}Ohm·sm. As the filler binary CdS/ZnS (50/50) with average particle size ranging from 50 to 63μm was used without treatment.

2. Composite sample preparation.

In the former case, CdS/ZnS powder in the desired amount was mixed thoroughly with the HDPE powder in an agate pestle mortar for 1h.This process coated the CdS/ZnS powder on the surface of the HDPE particles, so it is referred to as prelocalization of the conductive phase. Prolonged mixing improved the homogeneity of the spatial distribution of the conductive particles and their uniform coating thickness on the HDPE particles. The tumble mixed prelocalized powders was prepared for different graphite contents of 0-50vol.%. The resultant powder was further dried at 100^{0}C for 6h prior to compression molding. Then, the CdS/ZnS composites were prepared by hot - pressing the powder mixture technique of. The dried powder was filled in a tool steel die having diameter 26mm. The ponder was heated at an average heating rate of 6^{0}C/min under pressure of 15MPa to a maximum temperature of 150^{0}C. After soaking period of 10 minutes, the dick samples of 26mm diameter and thickness 12Om were punched from the plates and cooled down to 0^{0}C in a water-ice mixture (quenching mode) at atmospheric pressure to eliminate porosity, bubbles or blisters. This procedure improves the electrical properties, minimizes the after – shrinkage and enhances the quality and appearance of the samples. Thus, composites containing 0-50vol.% CdS/ZnS in the HDPE matrix were prepared. The specimens were sealed in air free polyethylene bags prior to measurements to avoid atmospheric and humidity effects that may induce same changes in the conductivity of the specimens.

The preparation mode of the composite makes it possible to obtain reproducible electrophysical parameters (electric resistance, capacitance, dielectric losses, Q quality) for most of some concentration. Some samples that had parameters differing from the parameters of the main group were not considered in the analysis (the number of these samples was not high).

3. Measurements.

To provide better contact with measuring probe surface, the disk specimens for the dielectric and resistivity measurements were coated with conducting silver paste at both sides as two electrodes. Samples were tested by two electrode scheme using a specially constructed sample holder shielded and grounded heated measuring cell of “sandwich” type, used for heating the samples, having system of measuring and potential electrodes with diameters of 15 and 20 mm, respectively. For measurement the samples were clamped firmly between the clamping stainless steel electrodes at a constant applied pressure of 5kq·sm^{-2}. The centering of the electrodes was provided by a special mandrel.

For studying the dielectric properties, the capacitance (C) and dissipation factor ($tan\delta$) of the samples were measured using a broadband precision immitanse meter (model E7-20, Belarus) from frequency 25 t0 10^{6}Hz at room temperature. The dielectric constant (ε') evaluated by the relation $\varepsilon'=CL/\varepsilon_0$ S where ε_0 is the permittivity of the free space (8,854x10^{-12}F/m). The dissipation factor was obtained directly from the instrument.

The properties of composites i.e. ε' and $tan\delta$ were estimated also at a constant frequency (1kHz) with varying temperature (from 20 to 150^{0}C). The heating rate of the samples was maintained at 3^{0}C/min. A calibrated copper –constantan thermocouple was used to measure the temperature of the specimen.

The samples were short circuited for one hour before taking any measurements to avoid any stray capacitance effects.

3. RESULT AND DISCUASION

The complex dielectric constant is usually defined as $\varepsilon=\varepsilon'- i\varepsilon''$, where ε′ is known as real part of permittivity. It is a measure of how much energy from an electric field is stored in a material. The ε'' is the imaginary part of permittivity and is also called as loss factor. It is a measure of how dissipative or lossy a material is to an external electric field. The ratio of imaginary to the real parts ($\varepsilon''/\varepsilon'$) is tanδ.

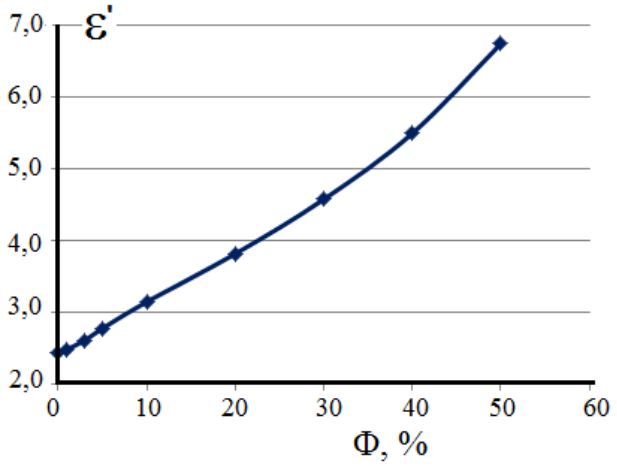

Fig. 1. Dielectric constant (ε′ at 10^{13}Hz) of HDPE – CdS/ZnS composites as a function of volume fraction of CdS/ZnS filler.

Fig. 1. shows the variation of ε′ with CdS/ZnS content at the room temperature for the HDPE- CdS/ZnS microcomposites tested at a frequency of 1kHz. It can be seen that the ε′ increases with increasing filler content. At 50vol.% CdS/ZnS, ε′ value reaches to 6,75, being ~2,8 times higher than that of neat HDPE (the measured at room temperature value of real part of complex dielectric

permittivity at frequency10^3Hz for a pure HDPE sample is equal to 2.4). Then increment in ε′ of composite with addition of CdS/ZnS content could be mainly ascribed to following two reasons [14]. One reason is Maxwell-Wagner (MW) interfacial polarization originating in the insulator filler (HDPE- CdS/ZnS) interfaces. MW effect arises when filler particles is dispersed within a non-conducting phase. The charge carries will be trapped at the boundaries of the fillers particles and matrix forming space charges. And when the electric field is applied these space charges will orient themselves along the applied field. Another reason is due to the formation of mini-capacitor networks in the HDPE- CdS/ZnS composites with increasing CdS/ZnS content. The minicapacitors consist of various CdS/ZnS microplatelets separated by a thin insulating polymer matrics. Such behavior of the ε' of the composite material with a semiconductor filler mainly depends on the MW polarization, the surface energy of the dielectric and the filler, the conductance of the system, and its proximity to the percolation threshold [15]. At a low concentration of the filler in the composite material, ε′ increases due to the VM polarization. However, as the concentration increases due to the difference in the surface energy of the components, the structure of the composite material becomes unstable, and CdS/ZnS particles form clusters whose surface is smaller than the total surface of the particles that form it. An increase in the number of clusters with an increase in the filler concentration is accompanied by a decrease in the dielectric layer between the particles and yields an increase in the capacity (and, as a result, in ε'). The lower magnitude of the experimental values for a higher CdS/ZnS content in comparison with the predicted result based on the Lichtenecker rule [16], may be due to the presence of isolated pores. Similar to ε', ε'' and $tan\delta$ values of the composites are also increases with CdS/ZnS content.

Fig. 2a shows the dielectric constant ε′ behavior for the HDPE and the composites with temperature measured at 1 kHz. As can be seen, the dielectric constant all composites first negligibly decrease up to 70^0C. A sharp decrease in dielectric constant for all the specimens is found when temperature reaches 70^0C and when the temperature approaches 100^0C ε′ tends to be independent of the temperature for pure HDPE. Figure 2a shows that the temperature dependence of ε′ does not depend on the CdS/ZnS content.

Fig. 2b shows the temperature dependence of loss tangent for neat HDPE and the HDPE-CdS/ZnS composites, respectively. It can be seen that an increase in the CdS/ZnS concentration in the matrix to 10vol% also yields a substantial increase in tanδ for all composites. The dielectric losses at the unital temperature of 20^0C was 0,0066±0,0009 for HDPE; for the composite materials with the filler particle concentration of 50vol.%, in increases to 0,069±0,0005. Large dielectric losses are related to the higher electric conductance as compared to pure HDPE. The electrical conductivity these specimens was monitored with respect to composition, i.e., CdS/ZnS concentration at the frequency of 1kHz showed that the introduction of about 50vol.% of CdS/ZnS into HDPE results in the electric conductance increase from for pure HDPE to for composite materials. This is over orders of magnitude higher than that of pure HDPE. The increase of conductivity with increasing of concentration of CdS/ZnS due to increases the charge carries which increasing filler contact where the CdS/ZnS particles at a low concentrations are represented by small darker regions and become large when the CdS/ZnS content increases and the network will be connected to each other containing the overlapping paths to allow the charge carries to pass through, where the charge carriers with routes through which the electrical resistance be less [17].

From the Figure 2b, it can be noted that the the dielectric losses becomes temperature dependent when the CdS/ZnS content approaches a value 10vol.%. The variation of tanδ with temperature becomes significant in the range of 50-130^0C. At low temperatures (up to 50^0C) tanδ attains rather constant values, while at temperatures higher than 50^0C increases rapidly with temperature and composition showing a maximum at 70^0C and then vanished. Pure HDPE and the composite system with 3 and 5vol.% filler content do not exhibit a peak.

In Figure 3 dielectric permittivity (ε') and loss tangent ($tan\delta$) as a function of frequency, at room temperature, for all the examined systems is presented. As expected, the dielectric constant of HDPE-CdS/ZnS micrrocomposites increases with the increase in CdS/ZnS content. From Fig. 3a, it can be seen that the dielectric constants of neat HDPE and its microcomposites with 3vol.% filler content are nearly independent of frequency. For the HDPE-10vol% CdS/ZnS microcomposite the dielectric constant decreases markedly with increasing frequency. The room temperature value of permittivity for HDPE-10vol% CdS/ZnS at frequency 25Hz is about 3,31, which decrease to about 2,90 at $5\cdot10^5$Hz. The frequency dependence of dielectric study indicates that introduction of CdS/ZnS increases the dielectric constant of the HDPE from about 2,5 to 3,31 at 10vol% of CdS/ZnS content. The ε′ values for 10vol% filler content are higher than both unfilled and with 3 and 5vol% filler content, probably due to a more important contribution of the interfacial polarization.

The variation of $tan\delta$ with the frequency for all tested filler concentrations at room temperature is shown in Figure 3b. The $tan\delta$ values of pure HDPE increases with increasing frequency from about 0,0027 to 0,0257 when the frequency reaches to $1\cdot10^6$Hz. A significant drop in $tg\delta$ occurs when the frequency reaches $5\cdot10^4$Hz. Pure HDPE do not exhibit a peak. Two relaxation processes are observed in both magnitudes in the frequency ranged studied. The peak located at around $1\cdot10^5$Hz is labeled as α - relaxation. It is then caused in the HDPE main chains by cooperative micro-Brownian motions within their amorphous regions [18]. The process at about 50Hz is ascribed to the molecular motions within the crystalline fraction of the HDPE material and it is named as α_c relaxation [19]. As seen in $tg\delta$ dependence, the location of α_c relaxation peak is shifted slightly toward higher frequencies (shorter times) with increasing filler content.

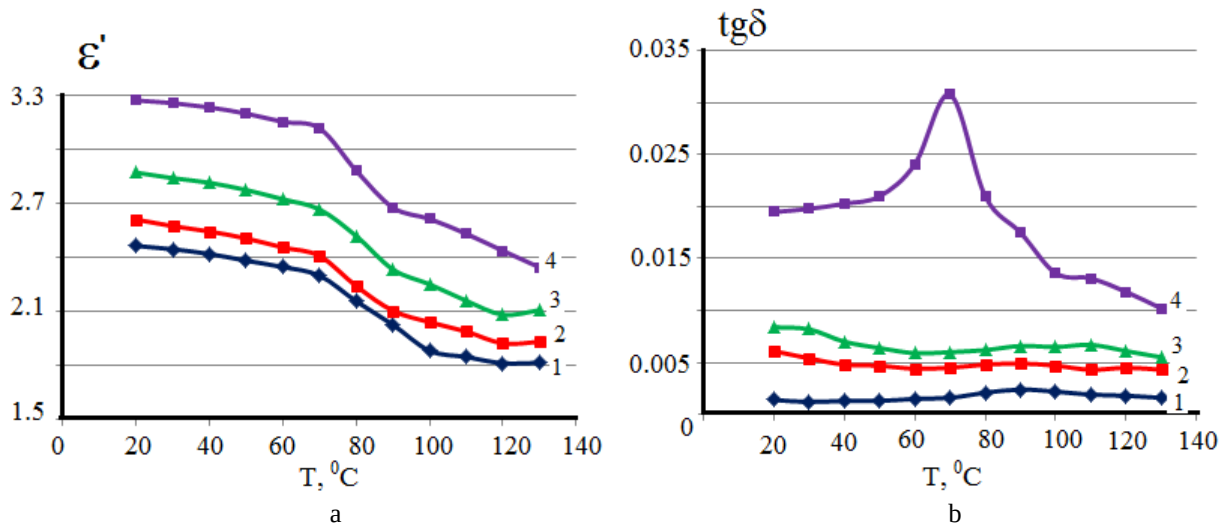

Fig. 2. Dielectric constant (ε') (a) and loss ($tan\delta$) (b) as a function of temperature.

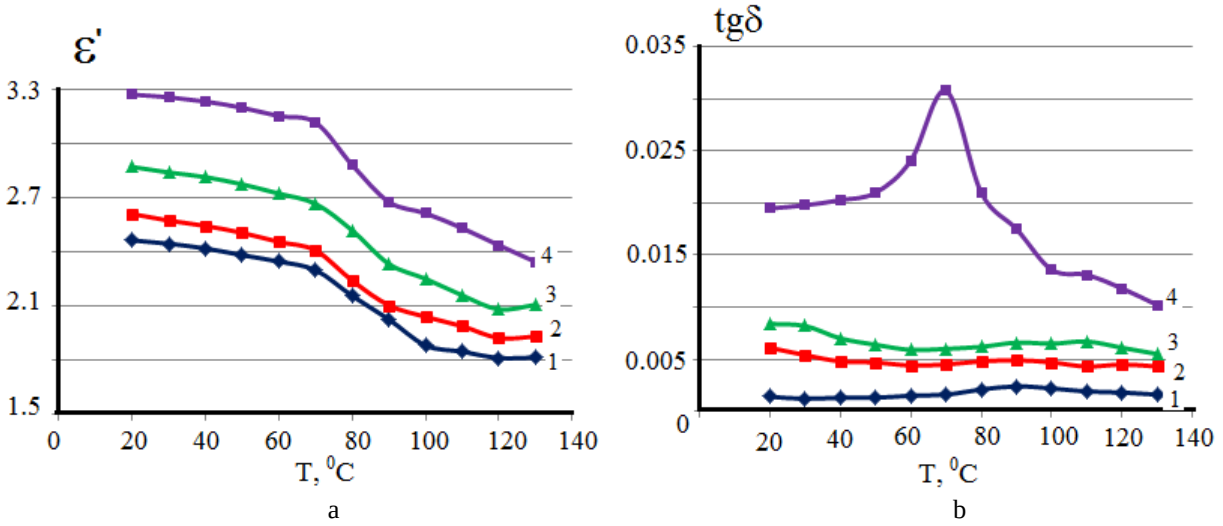

Fig. 3. Dielectric constant (ε') (a) and loss ($tan\delta$) (b) as a function of frequency.

CONCLUSIONS

In summary, ternary HDPE- CdS/ZnS microcomposites were fabricated using hot-pressing the powder mixture technique. Electrical measurements showed that the real part of permittivity of ternary HDPE/CdS/ZnS microcomposites increases with increasing CdS/ZnS content. The room temperature dielectric spectra show two relaxations process which is attributed to the MW relaxation. The peak shift to higher frequencies as the filler content is increased. In addition, both dielectric permittivity (ε') and dielectric loss ($tg\delta$) of the composites were found to be frequency and temperature dependent.

[1] *D.Y. Godovsky.* Device Applications of polymer nanocomposities. Advanced Polymer Science, 2000, v.153, 163-205.

[2] *V.L. Covlin, M.C. Schlamp and A.P. Alivisatos.* Light Emitting Diodes Made from Cadmium Selenide Nanochystals and a Semiconducting Polymer. Nature, 1994, v.370, No6488, 354-357.

[3] *F. Hussain, M. Nojati, M. Okomoto, R.E. Gorga.* Polymer-matrix Nanocomposites. Processing, Manufacturing, and Application: An Overwiev, J.Comp.Mat., 200b, pp.1511-1575.

[4] M. *Iovu, I. Tiginuanu, I. Culeac, S. Robu, Iu. Nistor, G. Dragalina, M. Enachi, and P. Petrenko.* Nanostructured Polymer/CdS Photoluminescent Thin Films. Journal of Nanoelectronics and Optoelectronics, 2013, v.7, pp.1-5.

[5] *V. Mathur, M. Dixit, K.S. Rathore, N.S. Saxena and K.B. Sharma.* Tensile Study of PVC-CdS Semiconducting Nanocomposite. Optoelectronic and Advanced Material: Rapid Communication, 2009, v.3, No7, pp.685-687.

[6] *M.A. Nuriyev, A.M. Maharramov, A.A. Shukurova, I.M. Nuriev.* Influence of heat treatment on the conductivity and radiothermoluminescence of nanocomposites LDPE/CdS obtained by the method of crazing in liquid media. International Journal of

Materials Science and Applications, 2014,3(6-1), p.7-10.

[7] *W.E. Mahmoud and A.A.A. Ghamdi.* The influence of Cd(ZnO) on the structure, Optical and Thermal Stabilities of Polyvinyl chloride Nanocomposites. Polymer Composites, 2011, v.32, No7, pp.1143-1147.

[8] 8.*A.F. Gochuyeva, G.Z. Suleymanov, M.A. Kurbanov, B.H. Khudayarov, Z.M. Mamedova.* Photoelectret. Effect in Polymer Composites Containing Photosensitive $A^{II}B^{VI}$ Semiconductors. Azerb.Journal of Physics, 2015, v.XXI, No2, Section Az, pp.6-10.

[9] *B.T. Kumbhare, S.P. Dongre, C.M. Dudhe.* Electrical Conductivity of Chemically Synthesized PANI/ZnS Composites. IOSR Jour. Of Appl.Physics (IOSR-JAP), 2016, v.8, Issue 3, Ver.1, pp.58-61

[10] *S.D. Bompilwar, S.B. Kondawar, V.A. Tabhane, S.R. Kargirwar.* Thermal stability of CdS/ZnS nanoparticles embedded conducting polyaniline Nanocomposites. Advances in Appl.Science Research, 2010, 1(1):166-173.

[11] *J. Yao, G. Zhao, D. Wang, G. Han.* Solve thermal synthesis and characterization of CdS nanowires/PVA composite films. Materials letters, 2005, 59, 3652-3655.

[12] *M. Dixit, S. Gupta, V. Mathur, K.S. Rathore, K.B. Sharma and N.S. Saxena.* Study of Glass Transition Temperature of PMMA and CdS-PMMA Composite. Chalcogenide Letters, 2009, v.6, No3, 131-136

[13] *A. Shik, H. Ruda, and E.H. Sargent.* Photoelectric phenomena in Polymer-based composites. Jour. of Appl. Physics, 2000, v.88, NO6, 3448-3453.

[14] *Y. Li, S.C. Tjong, R.K.Y. Li.* Dielectric properties of binary polyethylene fluoride/barium titanate nanocomposites and their nanographite doped hybrids. EXPRESS Polymer Letters, 2011, v.5, No6, 526-534.

[15] *M.M. Kuliyev, O.A. Samedov, R.S. Ismailova.* The temperature-Frequency Dispersion of the Dielectric Characteristics of Composite Materials Based on Polyethylene with $TlInS_2$ Inclusions. Surface Engineering and Applied Electrochemistry, 2013, v.49, N02, 91-96.

[16] *M. Olszowy.* Dielectric and Piezoelectric properties of the composites of ferroelectric ceramic and polyvinyl chloride. Condensed Matter Physics, 2003, v.6, No2, (34), 307-313.

[17] *S. Bhattacharya, V.K. Sacdev, Tandon.* Electrical properties of graphite filled Polymer composites, 2nd National Conference Mathematical Techniques: Emerging Paradigms for Electronics and IT Industries, 2008, 100-101.

[18] *A.Linares, A.Nogales, D.R.Rueda and T.A.Ezquerra.* Molecular dynamics in PVDF/PVA blends as revealed by dielectric loss spectroscopy. Jour.of Pol.Sci.- Part B: Polymer Physics, 2007, v.45, 1653-1661.

[19] *R.H. Royd*. Relaxation processes in crystalline. Polymers: Experimental behavior – A review. Polymer, 1985, v.26, 323-347.

Recevied: 04.07.2017

PRODUCTION OF SCALAR BOSON AND NEUTRINO PAIR IN LONGITUDINALLY POLARIZED ELECTRON-POSITRON COLLIDING BEAMS

S.K. ABDULLAYEV, M.Sh. GOJAYEV, N.E. NESIBOVA
Baku State University, Z. Khalilov str., 23,
AZ 1148, Baku, Azerbaijan, sabdullayev@bsu.edu.az, m_qocayev@mail.ru

Within the framework of the Minimal Supersymmetric Standard Model, the processes of the production of a scalar boson in longitudinally polarized electron-positron collisions are investigated: $e^-e^+ \to H\nu\bar{\nu}$, $e^-e^+ \to h\nu\bar{\nu}$, where $\nu\bar{\nu}$ is the neutrino-antineutrino pair. It is shown that each process is described by two spiral amplitudes F_{LR} and F_{RL} that describe the processes $e_L^-e_R^+ \to H(h)\nu\bar{\nu}$ and $e_R^-e_L^+ \to H(h)\nu\bar{\nu}$ accordingly. Two mechanisms for the creation of a scalar boson have been studied in detail: the radiation of a scalar boson by a vector Z^0-boson and the production of a scalar boson as a result of the fusion of W^+W^--bosons. An analytic expression of the effective cross sections is obtained, which describe the angular and energy distributions of the scalar boson.

Keywords: Scalar boson, Minimal Supersymmetric Standard Model, left and right coupling constants, helicity, Weinberg parameter.
PACS: 12.15-y; 12.15 Mm; 14.70 Hp.

1. INTRODUCTION

The Standard Model (SM), based on the local gauge symmetry group $SU_C(3)\times SU_L(2)\times U_4(1)$, has achieved great success in describing the strong, electromagnetic, and weak interactions between elementary particles [1-3]. With the recent discovery of the scalar Higgs boson at the Large Hadron Collider (LHC) by the ATLAS and CMS laboratories [4-5] (see also the reviews [6-8]) the CM of fundamental interactions has got a logical conclusion. We note that the SM contains one scalar doublet that provides a mass to $W^{\pm}$, Z^0-bosons, quarks, and leptons simultaneously. In this case, there is only one CP-even Higgs boson H_{CM}. The SM extension is the Minimal Supersymmetric Standard Model (MSSM), where, unlike SM, two doublets of scalar complex fields with hypercharges -1 and 1 are introduced [8-11]:

$$H_1 = \begin{pmatrix} H_1^0 \\ H_1^- \end{pmatrix}, \qquad H_2 = \begin{pmatrix} H_2^+ \\ H_2^0 \end{pmatrix}.$$

Scalar fields are written as:

$$H_1 = \frac{1}{\sqrt{2}}\begin{pmatrix} \vec{\upsilon}_1 + H_1^0 + iP_1^0 \\ H_1^- \end{pmatrix}, \quad H_2 = \frac{1}{\sqrt{2}}\begin{pmatrix} H_2^+ \\ \vec{\upsilon}_2 + H_2^0 + iP_2^0 \end{pmatrix},$$

where H_1^0, P_1^0, H_2^0 and P_2^0 are real scalar fields, υ_1 and υ_2 are the vacuum values of the fields $< H_1 >= \frac{1}{\sqrt{2}}\upsilon_1$ and $< H_2 >= \frac{1}{\sqrt{2}}\upsilon_2$.

CP-even *H* and *h*-bosons are obtained by mixing the fields H_1^0 и H_2^0 (α the mixing angle):

$$\begin{pmatrix} H \\ h \end{pmatrix} = \begin{pmatrix} \cos\alpha & \sin\alpha \\ -\sin\alpha & \cos\alpha \end{pmatrix}\begin{pmatrix} H_1^0 \\ H_2^0 \end{pmatrix}.$$

Similarly, we get Goldstone's $G^0, G^{\pm}, CP$ odd *A* and charged $H^{\pm}$-bosons (β mixing angle):

$$\begin{pmatrix} G^0 \\ A \end{pmatrix} = \begin{pmatrix} \cos\beta & \sin\beta \\ -\sin\beta & \cos\beta \end{pmatrix}\begin{pmatrix} P_1^0 \\ P_2^0 \end{pmatrix}, \quad \begin{pmatrix} G^{\pm} \\ H^{\pm} \end{pmatrix} = \begin{pmatrix} \cos\beta & \sin\beta \\ -\sin\beta & \cos\beta \end{pmatrix}\begin{pmatrix} H_1^{\pm} \\ H_2^{\pm} \end{pmatrix}.$$

131 H.Javid ave, AZ-1143, Baku
ANAS, G.M.Abdullayev Institute of Physics
E-mail: jophphysics@gmail.com

Thus, there are five Higgs bosons in the MSSM: two CP-even bosons h, H,, one CP-odd *A*-boson and two charged $H^{\pm}$ bosons. Here the Higgs boson sector is characterized by six parameters: M_H, M_h, M_A, $M_{H^{\pm}}$, α and β. Of these, only two parameters are free: M_A and $tg\beta$. The masses of the CP-even *h*- and *H*-bosons are expressed in terms of the masses M_A and M_Z:

$$M^2_{h(H)} = \frac{1}{2}\left[M_A^2 + M_Z^2 \mp \sqrt{\left(M_A^2 + M_Z^2\right)^2 - 4M_A^2 M_Z^2 \cos^2 2\beta} \right],$$

and the value $\cos^2(\beta-\alpha)$ is given by the relation:

$$\cos^2(\beta-\alpha) = \frac{M_h^2(M_Z^2 - M_h^2)}{M_A^2(M_H^2 - M_h^2)}\ .$$

The parameter $tg\beta$ is equal to the ratio of the vacuum values of the fields H_2^0 and H_1^0 $(tg\beta = \upsilon_2/\upsilon_1)$ varies within the limits $1 \le tg\beta \le m_t/m_b$, where m_t and m_b is the mass of t - and b -quarks.

In the present paper we have studied the processes of the production of a scalar *H* (or *h*) boson and a neutrino pair on longitudinally polarized electron-positron colliding beams:

$$e^- + e^+ \to H + \nu + \bar{\nu}\,, \tag{1}$$

$$e^- + e^+ \to h + \nu + \bar{\nu} \tag{2}$$

where $\nu\bar{\nu}$ is a pair of muon, tau-lepton or electron neutrinos ($\nu\bar{\nu} \Rightarrow \nu_\mu\bar{\nu}_\mu,\ \nu_\tau\bar{\nu}_\tau, \nu_e\bar{\nu}_e$).

2. THE MECHANISM OF EMISSION OF A SCALAR BOSON

The Feynman diagrams of the reaction (1) are shown in Fig. 1. In brackets are written 4-particle momentum, electron and positron helicity. We note that diagram a) corresponds to the emission of a scalar boson by a vector Z^0-boson.

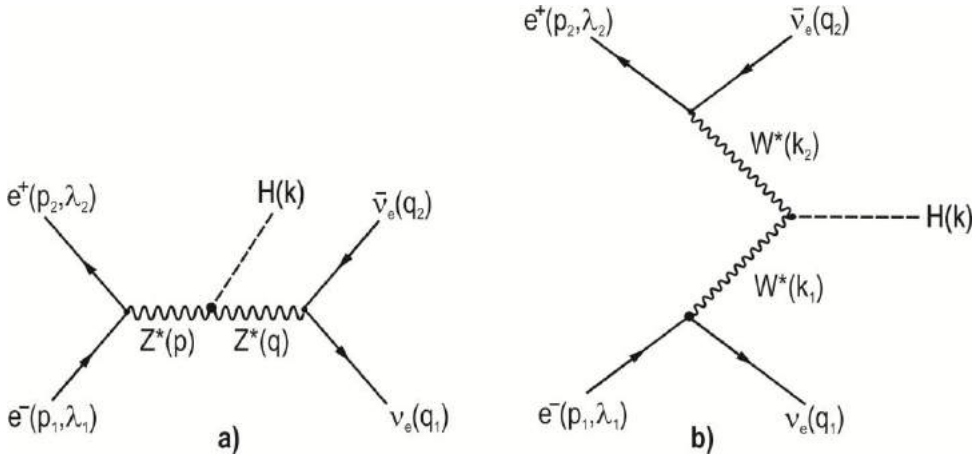

Fig. 1. Feynman diagrams of the reaction $e^-e^+ \to H\nu_e\bar{\nu}_e$.

Diagram a) corresponds to the following matrix element (here, the conservation of electron and neutrino currents is taken into account, and also $p^2 = (p_1 + p_2)^2 > M_Z^2$):

$$M_a(e^-e^+ \to H\nu\bar{\nu}) = i\left(\frac{e}{2\sin\theta_W \cdot \cos\theta_W}\right)^3 \cdot M_Z \cos(\beta-\alpha)\ D_Z(s)\, D_Z(xs) \times$$
$$\times \vec{\upsilon}(p_2,\lambda_2)\gamma_\mu[g_L(1+\gamma_5) + g_R(1-\gamma_5)]u(p_1,\lambda_1)\cdot\bar{u}(q_1)\gamma_\mu(1+\gamma_5)\upsilon(q_2), \tag{3}$$

where θ_W is the Weinberg angle,

$$D_Z(s) = (s - M_Z^2)^{-1}, \quad D_Z(xs) = (xs - M_Z^2 + iM_Z\Gamma_Z)^{-1},$$

M_Z and Γ_Z the mass and total width of the Z^0-boson, $s = p^2$ the square of the total energy of the e^-e^+-pair in the center-of-mass system, g_L and g_R the left and right coupling constants of the electron with the Z^0-boson

$$g_L = -\frac{1}{2} + x_W, \quad g_R = x_W, \tag{4}$$

$x_W = \sin^2\theta_W$ – the Weinberg parameter, x – the invariant mass of the neutrino pair in units s:

$$x = \frac{q^2}{s} = \frac{(q_1 + q_2)^2}{s} = 1 - \frac{2E_H}{\sqrt{s}} + \frac{M_H^2}{s}, \tag{5}$$

E_H and M_H is the energy and mass of the scalar boson *H*.

At high energies in weak interactions the helicity of the particles is conserved. Preservation of helicity requires that the colliding electron and positron have opposite helicities: $e_L^- e_R^+$ or $e_R^- e_L^+$. Here e_L^- – the left-polarized electron ($\lambda_1 = -1$), and e_R^+ – the right-handed positron ($\lambda_2 = +1$). Thus, the process (1) has two spiral amplitudes: F_{LR} and F_{RL} (the first and second indices correspond to the helicities of the electron and the positron, respectively). These spiral amplitudes describe the processes $e_L^- + e_R^+ \to H + \nu + \bar{\nu}$ and $e_R^- + e_L^+ \to H + \nu + \bar{\nu}$ are given by the expressions: $F_{LR} = D_Z(s)D_Z(xs)g_L, \quad F_{RL} = D_Z(s)D_Z(xs)g_R$.

First we consider the matrix element of the process $e_L^- + e_R^+ \to H + \nu + \bar{\nu}$:

$$M_a(e_L^- e_R^+ \to H\nu\bar{\nu}) = i\left(\frac{e}{2\sin\theta_w \cdot \cos\theta_w}\right)^3 \cdot M_Z \cos(\beta - \alpha) \cdot F_{LR} \times$$

$$\times[\vec{\upsilon}(p_2, \lambda_2 = 1)\gamma_\mu(1 + \gamma_5)u(p_1, \lambda = -1_1)] \cdot [\bar{u}(q_1)\gamma_\mu(1 + \gamma_5)\upsilon(q_2)] \tag{7}$$

and draw it square:

$$\left|M_a(e_L^- e_R^+ \to H\nu\bar{\nu})\right|^2 = \left(\frac{e^2}{4x_w(1 - x_w)}\right)^3 M_Z^2 \cos^2(\beta - \alpha)\left|F_{LR}\right|^2 T_{\mu\nu}^{(1)} T_{\mu\nu}^{(2)}. \tag{8}$$

Here

$$\begin{aligned} T_{\mu\nu}^{(1)} &= 8[p_{1\mu}p_{2\nu} + p_{2\mu}p_{1\nu} - (p_1 \cdot p_2)g_{\mu\nu} - i\varepsilon_{\mu\nu\rho\sigma}p_{1\rho}p_{2\sigma}], \\ T_{\mu\nu}^{(2)} &= 8[q_{1\mu}q_{2\nu} + q_{2\mu}q_{1\nu} - (q_1 \cdot q_2)g_{\mu\nu} + i\varepsilon_{\mu\nu\alpha\beta}q_{1\alpha}q_{2\beta}] \end{aligned} \tag{9}$$

– tensors of electron-positron and neutrino pairs. The product of these tensors gives a simple expression:

$$T_{\mu\nu}^{(1)} \cdot T_{\mu\nu}^{(2)} = 2^8(p_1 \cdot q_2)(p_2 \cdot q_1) = 2^8\, p_{1\alpha}p_{2\beta}\; q_{2\alpha}q_{1\beta}. \tag{10}$$

We integrate over momentum of neutrino and antineutrino pair by the invariant methods [12-15]:

$$I_{\alpha\beta} = \int q_{2\alpha}q_{1\beta} \cdot \frac{d\vec{q}_1}{\omega_1} \cdot \frac{d\vec{q}_2}{\omega_2}\, \delta(q_1 + q_2 - q) = A \cdot q^2\, g_{\alpha\beta} + Bq_\alpha q_\beta, \tag{11}$$

where A and B are scalar functions, and a $q = p - k$ is the total 4-momentum of the neutrino pair. To find the scalar functions A and B, we first multiply the integral $I_{\alpha\beta}$ by the tensor $g_{\alpha\beta}$, and then by $q_\alpha q_\beta$. The result is a system of equations

$$\begin{aligned} g_{\alpha\beta} I_{\alpha\beta} &= \frac{1}{2} q^2 I = 4Aq^2 + Bq^2, \\ q_\alpha q_\beta I_{\alpha\beta} &= \frac{1}{4} q^4 I = 4Aq^4 + Bq^4, \end{aligned} \tag{12}$$

where the integral

$$I = \int \frac{d\vec{q}_1}{\omega_1} \cdot \frac{d\vec{q}_2}{\omega_2} \, \delta(q_1 + q_2 - q)$$

it is easily calculated in the center of mass system of neutrinos and antineutrinos, and is equal to 2π. From the system of equations (12) we obtain:

$$A = \frac{\pi}{6}, \quad B = \frac{\pi}{3}.$$

Thus, for the integral $I_{\alpha\beta}$ we have the expression:

$$I_{\alpha\beta} = \frac{\pi}{6}(q^2 g_{\alpha\beta} + 2q_\alpha q_\beta). \tag{13}$$

As a result of integrating the neutrinos and antineutrinos momentum for the differential cross section of the process $e_L^- + e_R^+ \Rightarrow H + \nu + \bar{\nu}$ in the center-of-mass system we obtain:

$$\frac{d\sigma_a(e_L^- e_R^+ \Rightarrow H\nu\bar{\nu})}{dE_H d(\cos\theta)} = \frac{1}{12}\left(\frac{\alpha_{КЭД}}{x_w(1-x_w)}\right)^3 M_Z^2 s k_H \cos^2(\beta-\alpha)\left|F_{LR}\right|^2\left(2x + \frac{1}{s}k_H^2 \sin^2\theta\right). \tag{14}$$

Here $k_H = \sqrt{E_H^2 - M_H^2}$ is the momentum modulus of the scalar boson H, θ is the angle of emission of the H boson with respect to the momentum of the electron.

Similarly, we obtain the expression for the cross section of the reaction $e_R^- + e_L^+ \Rightarrow H + \nu + \bar{\nu}$:

$$\frac{d\sigma_a(e_R^- e_L^+ \to H\nu\bar{\nu})}{dE_H d(\cos\theta)} = \frac{1}{12}\left(\frac{\alpha_{KED}}{x_W(1-x_W)}\right)^3 M_Z^2 s k_H \cos^2(\beta-\alpha)\left|F_{RL}\right|^2\left(2x + \frac{1}{s}k_H^2 \sin^2\theta\right). \tag{15}$$

In the case of annihilation of a longitudinally polarized $e^- e^+$-pair, the contribution of diagram a) to the differential cross section of the reaction $e^- + e^+ \to H + \nu + \bar{\nu}$ is given by:

$$\begin{aligned} \frac{d\sigma_a(\lambda_1,\lambda_2)}{dE_H d(\cos\theta)} &= \frac{1}{96}\left(\frac{\alpha_{KED}}{x_W(1-x_W)}\right)^3 M_Z^2 s k_H \cos^2(\beta-\alpha)\times \\ \times[\left|F_{RL}\right|^2(1-\lambda_1)(1+\lambda_2) &+ \left|F_{RL}\right|^2(1+\lambda_1)(1-\lambda_2)]\left(2x + \frac{1}{s}k_H^2 \sin^2\theta\right). \end{aligned}$$

3. MECHANISM OF FUSION OF W^+W^--BOSONS

Now consider the diagram b) corresponding to the fusion mechanism of charged vector bosons. The matrix ele-

ment corresponding to this diagram is written as follows:

$$M_b(e^-e^+ \to Hv_e\bar{v}_e) = i\frac{e^3 M_W}{8\sin^3\theta_W}\cdot\cos(\beta-\alpha)D_1\cdot D_2\times$$

$$[\bar{u}(q_1)\gamma_\mu(1+\gamma_5)u(p_1,\lambda_1)]\cdot[\bar{\upsilon}(p_2,\lambda_2)\gamma_\mu(1+\gamma_5)\upsilon(q_2)]. \tag{18}$$

Here

$$\begin{aligned} &D_1 = (k_1^2 - M_W^2)^{-1}, \quad D_2 = (k_2^2 - M_W^2)^{-1}, \\ &k_1 = p_1 - q_1, \quad k_2 = p_2 - q_2, \end{aligned} \tag{19}$$

M_W – mass of a charged *W*-boson.

The square of the matrix element (18) is equal to:

$$\left|M_b(e^-e^+ \to Hv_e\bar{v}_e)\right|^2 = \left(\frac{e^3 M_W}{\sin^3\theta_W}\right)^2 \cos^2(\beta-\alpha)(D_1\cdot D_2)^2(1-\lambda_1)(1+\lambda_2)(p_2\cdot q_1)(p_1\cdot q_2). \tag{20}$$

The integration over momentum of neutrinos and antineutrinos is carried out in the center of mass system of this pair $\vec{q}_1 + \vec{q}_2 = 0$ (see Fig. 2). In this system we have [14, 15]:

$$\int |M_b|^2 \cdot \frac{d\vec{q}_1}{\omega_1}\cdot\frac{d\vec{q}_2}{\omega_2}\delta(p_1+p_2-k-q_1-q_2) = \int |M_b|^2 d\omega_1 d(\cos\theta_1)d\varphi_1\,\delta(E_1+E_2-E_H-2\omega_1) =$$

$$= \frac{1}{2}\int_{-1}^{1} d(\cos\theta_1)\int_0^{2\pi}|M_b|^2 d\varphi_1 \tag{21}$$

The square of the amplitude $|M_b|^2$ can be represented in the form (here it is taken into account that $q_2 = p_1 + p_2 - k - q_1$):

$$|M_b|^2 = \frac{1}{2}\left(\frac{e^3 M_W}{\sin^3\theta_W}\right)\cdot\cos^2(\beta-\alpha)\frac{(1-\lambda_1)(1-\lambda_2)\cdot[s-2(k\cdot p_1)-2(p_1\cdot q_1)]\,(p_2\cdot q_1)}{[2(p_1\cdot q_1)+M_W^2]^2\,[s+M_W^2-2(k\cdot p_2)-2(p_2\cdot q_1)]^2}. \tag{22}$$

We note that in the expression $|M_b|^2$ the dependence on the azimuth angle φ_1 appears only in the scalar product $(p_2\cdot q_1)$. In the coordinate system under consideration, we have:

$$\begin{aligned} (p_1\cdot q_1) &= \frac{1}{4}[s-2(k\cdot p_1)](1-\cos\theta_1), \\ (p_2\cdot q_1) &= \frac{1}{4}[s-2(k\cdot p_2)](1-\cos\theta_1\cos\chi-\sin\theta_1\sin\chi\cos\varphi_1), \end{aligned}$$

but $\cos\chi$ is expressed by invariant variables:

$$\cos\chi = 1 - \frac{2s[s+M_H^2-2(k\cdot p_1)-2(k\cdot p_2)]}{[s-2(k\cdot p_1)[s-2(k\cdot p_2)]}. \tag{23}$$

The integration over the azimuth angle φ_1 is easily carried out:

$$\int_0^{2\pi}|M_b|^2 d\varphi_1 \sim \frac{1}{s_1 s_2(h_1-\cos\theta_1)^2}\Big[2(h_2+\cos\theta_1\cos\chi)\cdot(1+\cos\theta_1)\times$$

$$\times\left(1+\frac{M_W^2}{s_2}\right)\cdot\frac{1}{R\sqrt{R}}-(1+\cos\theta_1)\cdot\frac{1}{R}\Bigg], \tag{24}$$

the notations are given by

$$\begin{aligned} &s_1 = s-2(k\cdot p_1), && s_2 = s-2(k\cdot p_2),\\ &h_1 = 1+\frac{2M_W^2}{s_1}, && h_2 = 1+\frac{2M_W^2}{s_2},\\ &R = \cos^2\theta_1 + 2h_2\cos\theta_1\cos\chi + h_2^2 - \sin^2\chi. \end{aligned} \tag{25}$$

The integrals over the polar angle θ_1 are easily calculated.

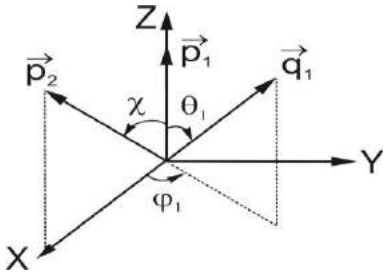

Fig. 2. The center of mass $\nu\bar{\nu}$ -pair system.

After integrating over the angles θ_1 and φ_1, for the differential cross section the following expression was obtained:

$$\frac{d\sigma_b(e^-e^+ \Rightarrow H\nu_e\bar{\nu}_e)}{dE_H\,d(\cos\theta)} = \frac{M_Z^2}{4}\left(\frac{\alpha_{KED}}{x_W(1-x_W)}\right)^3\cdot\frac{k_H}{s}\cos^2(\beta-\alpha)(1-\lambda_1)(1+\lambda_2)\cdot F_W. \tag{26}$$

Here

$$F_W = \frac{(1-x_W)^4}{s_1 s_2 r}\Bigg\{(1+h_1)(1+h_2)\left[\frac{2}{h_1^2-1}+\frac{2}{h_2^2-1}-\frac{6\sin^2\chi}{r}+\left(\frac{3t_1t_2}{r}-\cos\chi\right)\frac{L}{\sqrt{r}}\right]-$$

$$-\left[\frac{2t_1}{h_2-1}+\frac{2t_2}{h_1-1}+(t_1+t_2+\sin^2\chi)\frac{L}{\sqrt{r}}\right]\Bigg\} \tag{27}$$

$$s_1 = \sqrt{s}(\sqrt{s}-E_H+k_H\cos\theta), \quad s_2 = \sqrt{s}(\sqrt{s}-E_H-k_H\cos\theta),$$

$$\cos\chi = 1-\frac{2xs}{xs+k_H^2\sin^2\theta}, \quad \sin^2\chi = 1-\cos^2\chi,$$

$$t_1 = h_1+h_2\cos\chi, \quad t_2 = h_2+h_1\cos\chi, \quad r = h_1^2+h_2^2+2h_1h_2\cos\chi-\sin^2\chi,$$

$$L = \ln\frac{h_1h_2+\cos\chi+\sqrt{r}}{h_1h_2+\cos\chi-\sqrt{r}}$$

In the process of production of a neutrino pair $\nu_e\bar{\nu}_e$ between diagrams a) and b), there is an interference. The interference contribution to the cross section is given by:

$$\frac{d\sigma(e^-e^+ \Rightarrow Hv_e\bar{v}_e)}{dE_H d(\cos\theta)} = \frac{M_Z^2}{4}\left(\frac{\alpha_{КЭД}}{x_W(1-x_W)}\right)^3 \cdot \frac{k_H}{s}\cos^2(\beta-\alpha)(1-\lambda_1)(1+\lambda_2)g_L F_I, \quad (28)$$

where

$$F_I = \frac{1}{2}(1-x_W)^2 \frac{xs - M_Z^2}{(s-M_Z^2)[(xs-M_Z^2)+M_Z^2\Gamma_Z^2]} \times$$

$$\times\left[2-(h_1+1)\ln\frac{h_1+1}{h_1-1} - (h_2+1)\ln\frac{h_2+1}{h_2-1} + (h_1+1)(h_2+1)\frac{L}{\sqrt{r}}\right]. \quad (29)$$

4. DISCUSSION OF THE RESULTS

The differential cross section of the reaction $e^- + e^+ \to H + \nu_e + \bar{\nu}_e$ measured in the experiments consists of three parts: the contribution of diagram a), the contribution of diagram b), and the interference contribution. At the energies of a e^-e^+-pair $\sqrt{s} > M_Z$, the differential cross section has the form:

$$\frac{d\sigma(e^-e^+ \Rightarrow Hv_e\bar{v}_e)}{dxd(\cos\theta)} = \frac{M_Z^2}{8}\left(\frac{\alpha_{KED}}{x_w(1-x_w)}\right)^3 \frac{k_H}{\sqrt{s}}\cos^2(\beta-\alpha)\times$$
$$\times\{3[g_L^2(1-\lambda_1)(1+\lambda_2)+g_R^2(1+\lambda_1)(1-\lambda_2)]F_s + (1-\lambda_1)(1+\lambda_2)(g_L F_I + F_W)\}. \quad (30)$$

Here the function F_s corresponds to the contribution of diagram a) (the scalar boson *H* is emitted by the vector boson Z^0):

$$F_s = \frac{1}{12}\cdot\frac{s(2xs + k_H^2\sin^2\theta)}{(s-M_Z^2)^2[(xs-M_Z^2)^2+M_Z^2\Gamma_Z^2]}. \quad (31)$$

The factor 3 in the first term (30) is associated with the possibility of decay of the Z^0-boson into three types of neutrino pair $(\nu_e\bar{\nu}_e,\ \nu_\mu\bar{\nu}_\mu,\ \nu_\tau\bar{\nu}_\tau)$. In the annihilation of a left-handed polarized electron and a right-polarized positron, we have a cross section:

$$\frac{d\sigma(e_L^-e_R^+ \Rightarrow Hv_e\bar{v}_e)}{dxd(\cos\theta)} = \left(\frac{\alpha_{KED}}{x_W(1-x_W)}\right)^3 \cdot \frac{M_Z^2}{2}\cdot\frac{k_H}{\sqrt{s}}\cos^2(\beta-\alpha)[3g_L^2F_s + g_L F_I + F_W]. \quad (32)$$

If the electron (positron) is polarized right (left), then the contribution of diagram b) vanishes and the differential cross section takes the form:

$$\frac{d\sigma(e_R^-e_L^+ \to Hv_e\bar{v}_e)}{dxd(\cos\theta)} = \left(\frac{\alpha_{KED}}{x_W(1-x_W)}\right)^3 \frac{M_Z^2}{2}\cdot\frac{k_H}{\sqrt{s}}\cos^2(\beta-\alpha)\cdot 3g_L^2F_s. \quad (33)$$

In the case of unpolarized colliding electron-positron beams, the differential cross section of the reaction $e^- + e^+ \to H + \nu + \bar{\nu}$ is expressed by the formula:

$$\frac{d\sigma(e^-e^+ \to Hv_e\bar{v}_e)}{dxd(\cos\theta)} = \frac{M_Z^2}{8}\left(\frac{\alpha_{KED}}{x_W(1-x_W)}\right)^3 \cdot\frac{k_H}{\sqrt{s}}\cdot\cos^2(\beta-\alpha)\cdot[3(g_L^2+g_R^2)F_s + g_L F_I + F_W]. \quad (34)$$

On the fig. 3 shown the angular dependence of the h-boson in the reaction, at an energy of $\sqrt{s}$ =1000 GeV, a mass of $M_h = 67.533$ GeV, energy $E_h = 2M_h$ and the Weinberg parameter $x_W = 0.232$. As can be seen from the

figure, with increasing boson emission angle, the contribution of the diagram *a*) increases and reaches a maximum at an angle of $\theta = 90°$, and a further increase in the angle leads to a decrease in the cross section. But the contribution of diagram *b*) decreases with increasing angle θ and reaches a minimum at $\theta = 90°$. The contribution to the cross section from the interference of diagrams a) and b) is negative. The dependence of the total cross section of the process $e^- + e^+ \to h + \nu_e + \bar{\nu}_e$ on the angle θ in the fig. 3 is shown by the dotted line

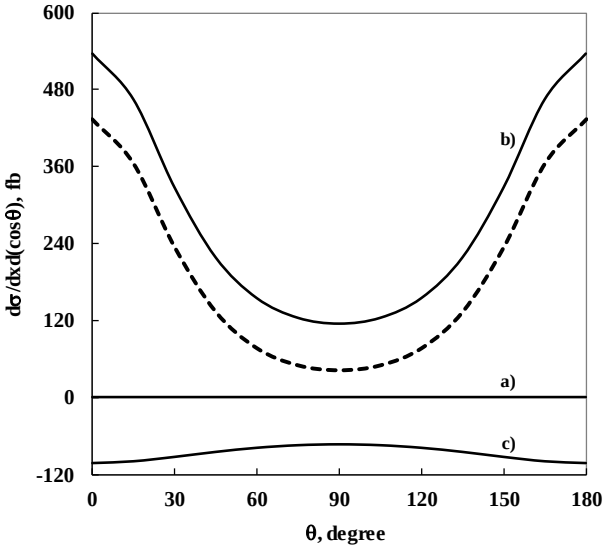

Fig. 3. Angular dependence of the effective cross section of the process $e^- + e^+ \to h + \nu_e + \bar{\nu}_e$.

Similar results were obtained for the reaction $e^- + e^+ \to H + \nu_e + \bar{\nu}_e$.

[1] *S.Q. Abdullayev.* Lepton-lepton və lepton-hadron qarşılıqlı təsirlərində zəif cərəyan effektləri (I hissə), Bakı, «AM 965 MMC», 2012, 484 s.

[2] *A. Djouadi.* The Anatomy of Electro-Weak Symmetry Breaking. Tome I: The Higgs boson in the Standard Model. arXiv: hep-ph/0503172v2, 3 May, 2005.

[3] *P. Langacker.* The Standard Model and Beyond. CRC Press, 2010, 635p.

[4] ATLAS Collaboration. Observation of a new particle in the search for the Standard Model Higgs boson with the ATLAS detector at the LHC. Phys. Letters, 2012, B 716, p. 1-29.

[5] CMS Collaboration. Observation of a new bozon at mass of 125 GeV with the CMS experiment at the LHC. Phys. Letters, 2012, B 716, p.30-60.

[6] *V.A. Rubakov.* Uspexi fizicheskix nauk, 2012, tom 182, №10, s. 1017-1025. (In Russian).

[7] *A.V. Lanev.* UFN, 2014, t.184, №9, s. 996-1004. (In Russian).

[8] *D.I. Kazakov.* UFN, 2014, t.184, №9, s.1004-1017. (In Russian).

[9] *A. Djouadi.* The Anatomy of Electro-Weak Symmetry Breaking. Tome II: The Higgs in Minimal Supersymmetric Model. arXiv: hep-ph/0503173v2, 2003.

[10] *H. Baer, X. Tata.* Weak Scale Supersymmetry: from Super fields to Scattering Events. Cambridge Univ. Press, 2006.

[11] *D.I. Kazakov.* Beyond the Standard Model (In search of supersymmetry), hep-ph/0012288; in 2000 European Schall of High Energy Physics, Caramulo, Portugal, 20 August – 2 September 2000.

[12] *S.K. Abdullayev, M.Sh. Gojayev, F.A. Saddigh.* Higgs boson production in electron-positron annihilation. Azerbaijan Journal of Physics, Fizika, 2014, N 2, p.29-35.

[13] *S.K. Abdullayev, L.A. Agamaliyeva, M.Sh. Gojayev, F.A. Saddigh.* The investigation of production Higgs bosons in lepton-antilepton collisions. GESJ: Physics, 2015, N 1(13), p.36-55 (in Russian).

[14] *S.K. Abdullayev, M.Sh. Gojayev, F.A. Saddigh.* Journal of Qafqaz University: Physics, 2015, N 1, p.73-79.

[15] *S.K. Abdullayev, M.Sh. Gojayev, F.A. Saddigh.* Azerbaijan Journal of Physics, Fizika, 2015, N 3, p.21-30.

Recevied: 07.06.2017

FABRICATION AND INVESTIGATION OF CONDUCTIVE POLYMERIC NANOCARBON COMPOSITES BASED ON IODINE - FUNCTIONALIZED MULTI - WALLED CARBON NANOTUBES

S.H. ABDULLAYEVA[1,2], A.B. HUSEYNOV[1], I.G. NAZAROV[3], A.O. ISRAFILOV[1], N.M. MADATLY[3]

[1]Research & Development Center for Hi-Technologies (RDCHT), MCHT, İnşaatçılar ave. 2, Az - 1073, Baku, Azerbaijan

[2]G.M. Abdullayev Institute of Physics, Azerbaijan NAS, H.Javid ave. 33, AZ-1143 Baku, Azerbaijan

[3]Baku branch of the Moscow State University named after M.V. Lomonosov (MSU), F.Agayev str 9., AZ - 1141, Baku, Azerbaijan

e-mail: asker.huseynov@rambler.ru

The present article is dedicated to the synthesis of multiwalled carbon nanotubes (MWNTs) by aerosol - assisted chemical vapour deposition method, the functionalization of their surface by crystalline iodine, and the preparation on the basis of the latest new electrically conductive polymeric nanocomposites. For this purpose, 3 polymers were chosen as polymer matrices: silicone, polyurethane and epoxy resin. For the final nanocomposites, the current-voltage characteristics were measured and on the basis of the obtained data the electrical conductivity of polymer composites were determined. Moreover, in this paper, the influence of the functionalization process as well as the type of used polymers on the electrical properties of composites is also discussed.

Keywords: MWCNTs, Aerosol-assisted chemical vapour deposition (AACVD), ferrocene,cyclohexane, xylene, polymers, silicone, epoxy, polyurethane, conductive polymer nanocomposites, functionalization, iodine, volt-ampere characteristics, Raman spectroscopy, SEM; IR spectroscopy.

PACS: 61.48.De

1. INTRODUCTION

One of the actual and progressive trends of nanoindustry, in particular, modern materials science is the creation of new functional and structural materials with specified properties [1]. Among them, the most promising and in great demand nanomaterials over the past two decades that has attracted tremendous attention of the researches from both an academic and industrial point of view are novel conductive polymer composite materials with fundamentally and specified new properties by means of the nanometer-scale components addition [2, 3].The electrical conductivity of polymers - dielectrics can be imparted by incorporating conductive fillers, provided retaining their polymeric characteristics. Outstanding characteristics of innovative high-tech material – carbon nanotubes such as excellent electrical and thermal conductivity, high stiffness and tensile strength, an extremely large surface area, miniscule size, unique atomic structure etc. make them perfect candidates as nanofillers i.e., as a reinforcement instead of other conventional materials in resulting polymer composites to improve their chemical and physical properties [4-6].

However there are two significant limitations in developing high performance polymer /CNTs composites: homogeneous dispersion of carbon nanotubes in the matrices and low interfacial interaction between nanotubes and polymers [7]. In this connection the chemical modification of the graphitic sidewalls and tips of CNT have key roles to prevent nanotubes aggregation owing to strong intermolecular Van der Waals forces between them, which helps to better disperse and stabilize the CNTs and enhance their chemical affinity to engineering polymer matrices [8,9].

Conductive polymer nanocomposites open wide prospects for their potential practical application in many different areas such as transistors [10], sensing materials [11],energy storage and energy conversion devices [12], biomedical applications (biosensors, drug delivery systems, biomedical implants and tissue engineering) [13] and so on. In the literature [14-19] there are scanty data on the research in the field of iodination of MWCNTs, and there is practically no information [20] on nanocomposites based on them. In this connection the aim of our present work is to produce new conducting polymers – nanocarbon composites based on iodine - functionalized multi-walled carbon nanotubes and epoxy, silicone and polyurethane polymers and to study the effect of the functionalization of CNTs on the electrochemical characteristics of the final materials.

2. EXPERIMENTAL PROCEDURES DETAILS

2.1. Aerosol - assisted chemical vapour deposition (AACVD) synthesis process of MWCNTs and its purification

The AACVD synthesis setup and the standard procedure are described in detail in the work [21]. Briefly, experiments on the synthesis of multiwalled carbon nanotubes were carried out in the laboratory setup using ferrocene (Fc) as the precursor of the catalyst, and cyclohexane (CyH) as the raw carbon material.

A chemical quartz beaker (200 ml volume) containing a solution of ferrocene in cyclohexane with a quantitative ratio of 20 mg / ml was placed in an aerosol generator (nebulizer) where it was ultrasonically exposed. As a carrier (diluting) gas and a reducing agent were used high purity argon and hydrogen with a space velocity of

131 H.Javid ave, AZ-1143, Baku
ANAS, G.M.Abdullayev Institute of Physics
E-mail: jophphysics@gmail.com

1.1 l / min and 0.1 l / min, respectively. The generated aerosol by the flow of argon gas is transported to the reactor, where in the hot zone of the tubular furnace occurs thermolysis of the organometallic precursor and the growth of multi-walled carbon nanotubes. The synthesis temperature was 900 °C. For uniform deposition of carbon nanotubes during the AACVD process, the electric furnace was automatically moved along the length of the reactor at a rate 10 mm / min. The principal scheme of the experimental setup is illustrated in Fig. 1.

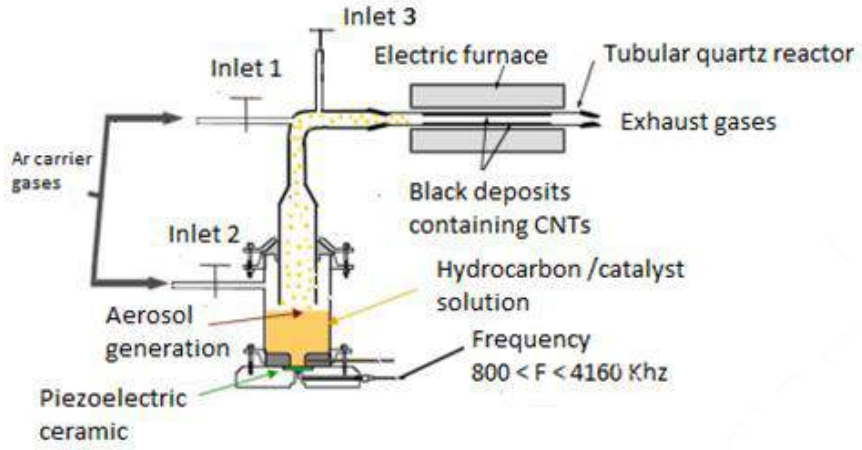

Fig. 1. Schematic illustration of the experimental device used for the aerosol-assisted CCVD process.

a) b)

Fig. 2. The stage of purification of MWCNTs from tarry substances by extraction method: a) MWCNTs suspension with solvent during extraction; b) MWCNTs suspension with solvent after extraction.

The purification process of multiwalled carbon nanotubes from by-products was carried out by two well-known methods.

The purification process of MWCNTs from tarry impurities was carried out as a result of extraction using xylene and cyclohexane as solvents in volume - weight ratio (ml / g) of 30: 1 heated to 80 °C. Herewith the transparent xylene painted in yellowish color. Purification was carried out until the color disappears completely (Fig. 2). Then, to remove the catalytic iron (Fe) particles, the carbon nanotubes released from the tarries were treated with dilute nitric acid (28% HNO_3) at a moderate temperature (T = 80 °C) for 2 hours and constant stirring.

2.2. Obtaining of functionalized MWCNTs by direct iodination the surface of carbon nanotubes (I - MWCNTs)

2.2.1. The method of direct iodination of MWCNTs

The required amount of a sample of synthesized MWCNTs and commercial crystalline iodine was weighed to the accuracy 0.1 mg and placed in a thick-walled quartz reactor, the open end of which was sealed.

The reactor was placed in a tubular muffle furnace in which it was at 350 °C for 3 hours. As the temperature was raised, the crystalline iodine passed to the vapor state and reacted with multiwalled carbon nanotubes to form the C-I bond. At the end of the reaction time, the reactor was cooled, after which the end of the quartz tube was cut and the obtained target product was recovered from the reactor. As a test experiment, a small amount of the formed modified nanotubes was washed with ethanol, as a result of which ethanol acquired a red color. This indicated that during the reaction, not all of the iodine reacted with the MWCNTs, and some of it was absorbed into the pores of the carbon nanotubes.

Two samples were prepared from the final product. The first sample was a functionalized MWCNTs, in which both chemically (covalently) bound iodine and adsorbed iodine were present (Ch + ads. I – MWCNTs) .In the second sample, iodine was bound to MWNTs only by covalent bonds (Ch I – MWCNTs). It was obtained as a result of repeated washing of the first sample with alcohol until the color of iodine completely disappears. The final samples were placed in a drying cabinet and kept until the alcohol was completely evaporated at a temperature of 1200 °C.

In particular, when preparing first sample for 1 gram of initial nanotubes, 3 grams of crystalline iodine was consumed, and thus the concentration of the latter in the sample was 75 wt % or 23.6 mmol / g. By weighing the sample after washing it with alcohol and drying, it was determined that in the second sample the iodine concentration was 57.6 % by weight or 10.7 mmol / g.

The iodinated MWCNTs were characterized by Scanning electron microscopy (SEM), Raman spectroscopy, Fourier transform infrared spectroscopy (FTIR).

2.3. Preparation of polymers (epoxy, silicone and polyurethane) / I - MWCNTs nanocomposites

As a starting materials for the preparation of polymer nanocomposites – multi-walled carbon nanotubes were used several polymeric resins – polyurethane, silicone and epoxy and various types of MWCNTs samples such as impurity-free (resin, iron catalyst particles) MWNCNTs, MWNCNTs sample with a chemically bound iodine (Ch I – MWCNTs) and a sample containing simultaneously chemically bound and adsorbed iodine (Ch + ads. I – MWCNTs).

Dispersing of carbon nanotubes was carried out in liquid resins and as a result of their subsequent polymerization a solid nanocomposites (MWCNTs / polymer) was obtained.

A required amount of polymer resin (in the case of an epoxy resin, also a hardener) and dispersible samples of carbon nanotubes were weighed in a beaker. The contents of the chemical glass with a spatula were carefully transferred to the lower plate of the mixer. Further, above the lower plate, an upper plate with a clearance of 200 micrometers was mounted, connected to an electric motor with a rotation speed of 450 rpm. The dispersion time was 10 minutes and the temperature was 20 °C. The resulting mixture of components was transferred to metal rectangular shapes with dimensions (length = 15 mm, width = 10 mm, thickness = 4 mm) and placed in a thermostat at a temperature of 100 °C where a polymerization process was carried out for 8 hours. Then, the electrical characteristics and surface morphology of the solid samples of the composites were examined. Figure 3 displays a laboratory made dispersing device for the preparation of polymer - carbon nanotubes composite [22].

Fig. 3. Dispersing device for the preparation of polymer-carbon nanotubes composite.

3. RESULS AND DISCUSSION

3.1. The results of purification of synthesized MWCNTs from tarry impurities

Weighing of sample of obtained MWCNTs before and after washing with solvents (xylene, cyclohexane) showed that the amount of tarries in the pristine sample was 8.5 wt %.

3.2. The results of purification of MWCNs from the iron content

The processing of the MWCNTs sample with dilute nitric acid in accordance with the procedure described in the experimental section 2.1 reduced the initial iron content from 7.2 mass% to 3.5 mass%.

3.3. Scanning electron microscopy (SEM)

SEM photographs of synthesized MWCNTs and its elemental analysis are presented in Figure 4.

From the photograph of the synthesized carbon nanotubes a) it is observed that the average diameter of the obtained nanotubes is 37 nm, and the result of its elemental analysis b) showed that the weight percentage of carbon is 99.5 % and the residual amounts of the iron catalyst are 0.5 %.

As can be seen from the above photographs, carbon nanotubes were not severely degraded in the process of functionalization, but, as expected, their elemental composition changed.

According to elemental analysis, iodine was fixed on the surface of iodinated samples. In the sample (Ch I – MWCNTs) in which both the chemically bound and adsorbed forms are present, the amount of iodine is 4.9 weight.%, and in the sample (Ch + ads. I – MWCNTs) from which loosely bound iodine was washed – only 0.2 weight.%, which obviously corresponded to the chemically bound iodine on the MWCNTs surface.

3.4. Fourier transform infrared (FTIR) spectroscopy

The initial synthesized (pristine) MWCNTs and the iodine modified samples prepared on their basis were studied by IR spectroscopy (Figures 8 -10).

The IR spectrum of the initial (non-functionalized) MWCNTs sample demonstrate the presence of absorption bands in the 3430 and 1652 cm^{-1} regions related to the stretching vibrations OH and C = O, respectively.

The presence of these groups can be explained by the treatment of carbon nanotubes sample with nitric acid (28% HNO_3) in the process of purification from iron impurities.

In the IR spectrum of the sample (Ch I – MWCNTs) with chemically modified iodine, in contrast to the pristine sample, an intense peak of C-I appears in the range of absorption regions of 550-570 cm^{-1}, corresponding to chemically bound iodine. A similar band is also observed in the IR spectrum of the sample (Ch + ads. I – MWCNTs) which indicates the presence of chemically bound iodine in both samples.

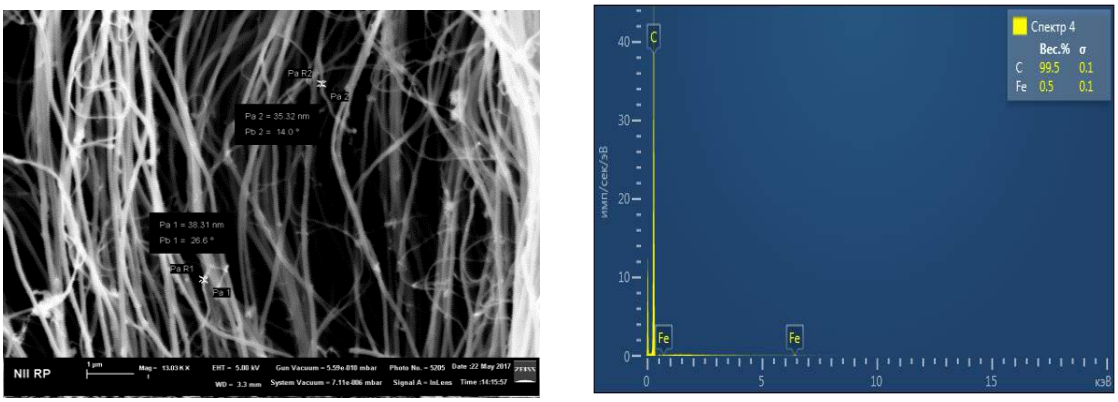

a) b)

Fig. 4. a) SEM micrographs of synthesized MWNTs (T = 900°C, Fc:CyH = 20 mg / ml).

SEM photographs of functionalized MWCNTs and their elemental analysis are presented in Figures 5-6.

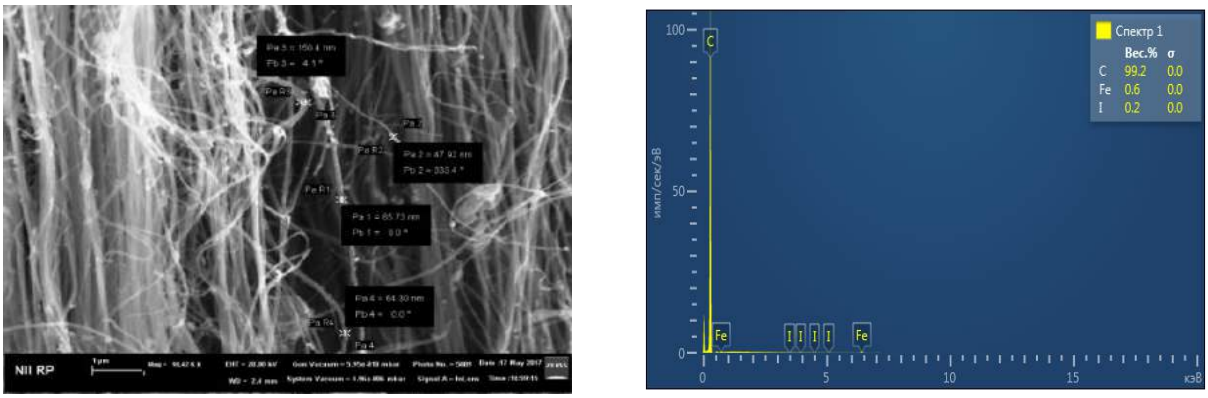

a) b)

Fig. 5. a) SEM photograph and b) elemental analysis of Ch I – MWCNTs sample.

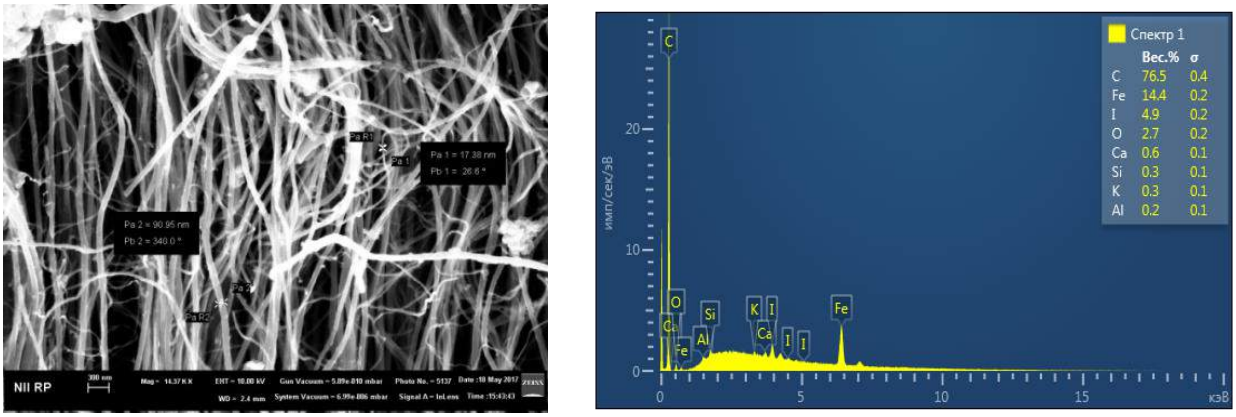

a) b)

Fig 6. a) SEM photograph and b) elemental analysis of Ch + ads. I – MWCNTs sample.

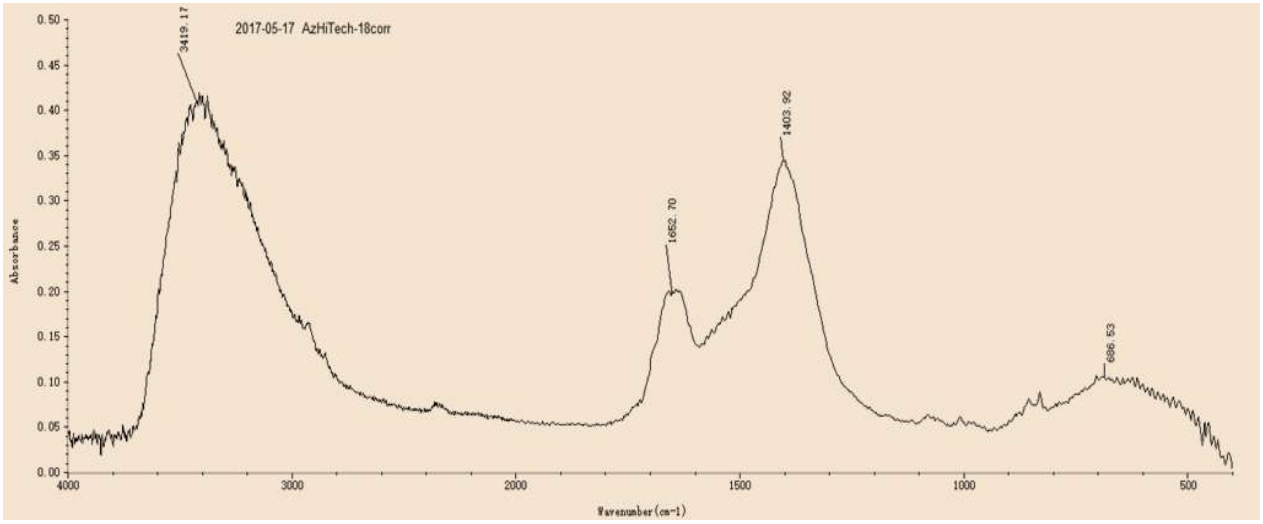

Fig. 7. The IR spectrum of the pristine sample of MWCNTs.

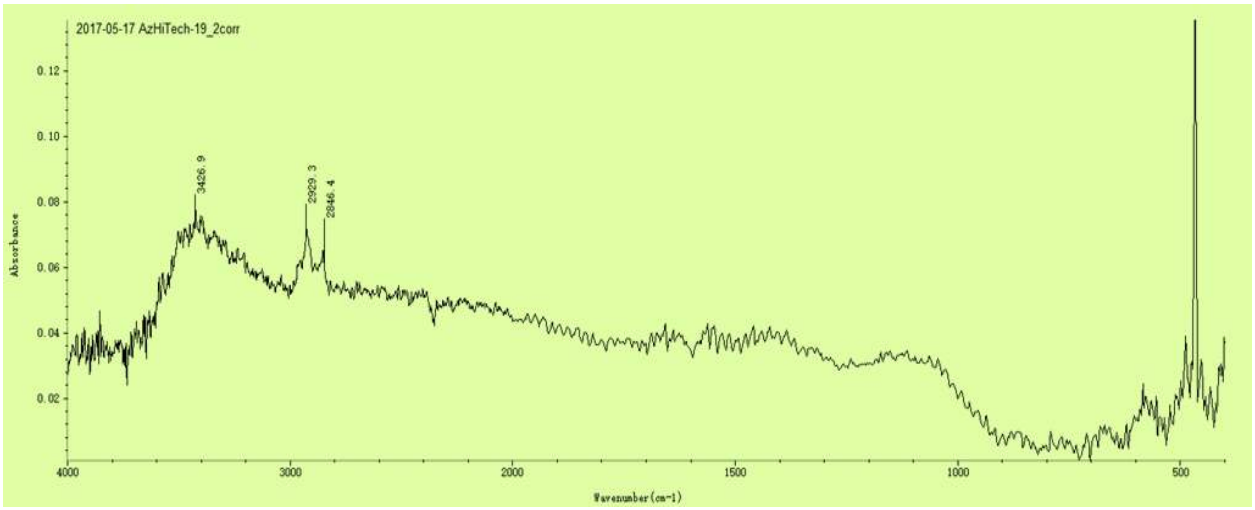

Fig. 8. The IR spectrum of the Ch I – MWCNTs sample.

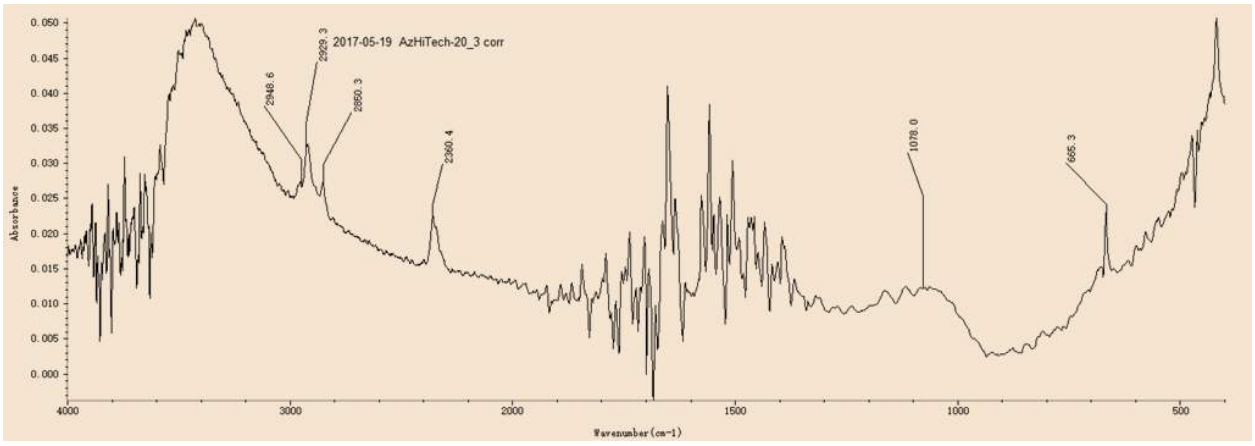

Fig. 9. The IR spectrum of the Ch + ads. I – MWCNTs sample.

3.5. Investigation of manufactured nanocarbon – polymer composites

On the basis of 3 samples of carbon nanotubes (pristine and 2 types of iodine -modified MWCNTs) and also based on 3 polymers: polyurethane, silicone and epoxy, 9 samples of nanocarbon – polymer composites were prepared for which their current-voltage characteristics were measured (Figures 10-14).

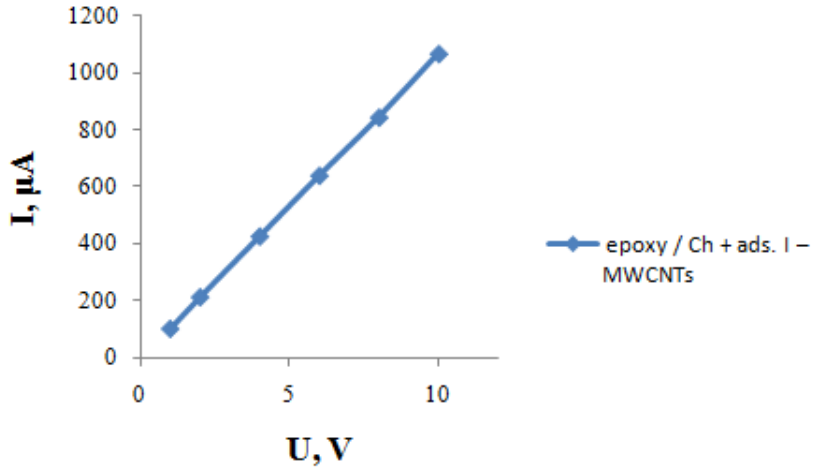

Fig. 10. Volt – ampere characteristics of polymeric nanocomposites based on epoxy / (Ch + ads.I – MWCNTs).

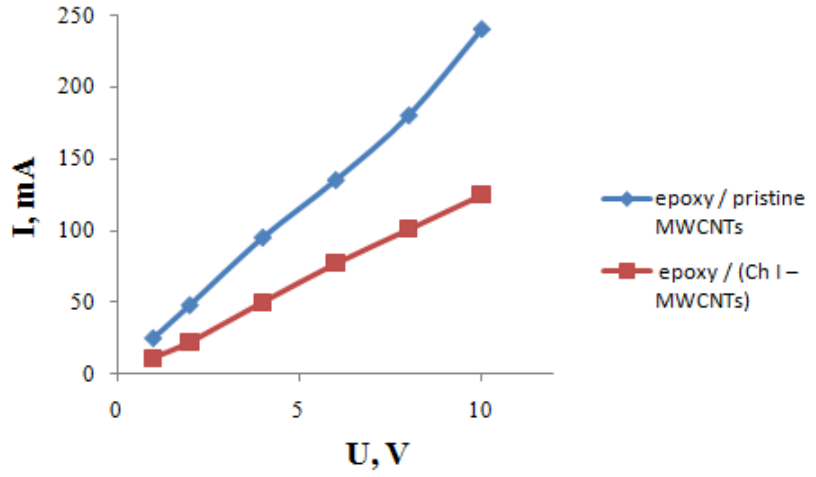

Fig. 11. Volt – ampere characteristics of polymeric nanocomposites based on epoxy / pristine MWCNTs and epoxy / (Ch I – MWCNTs).

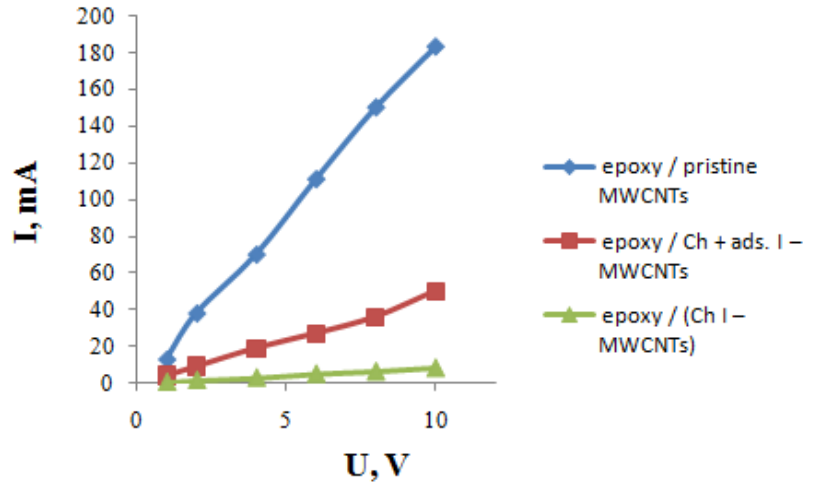

Fig. 12. Volt – ampere characteristics of polymeric nanocomposites based on epoxy / pristine MWCNTs, epoxy / Ch + ads. I – MWCNTs and epoxy / (Ch I – MWCNTs).

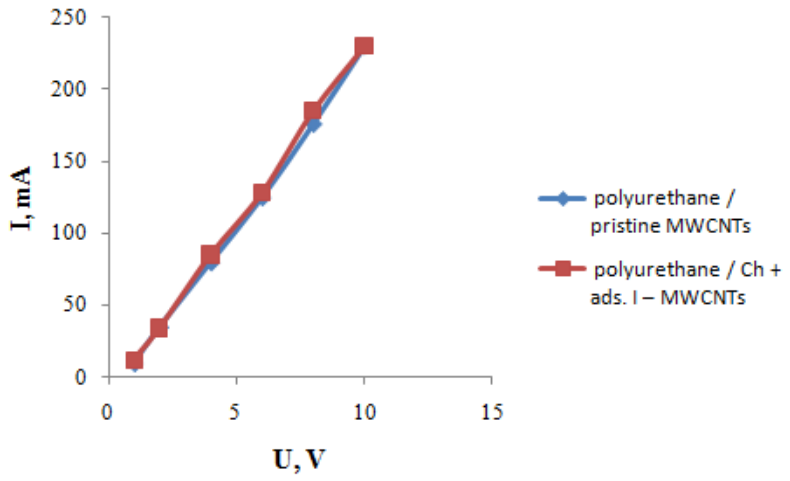

Fig. 13. Volt – ampere characteristics of polymeric nanocomposites based on polyurethane / pristine MWCNTs and polyurethane / (Ch + ads.I – MWCNTs).

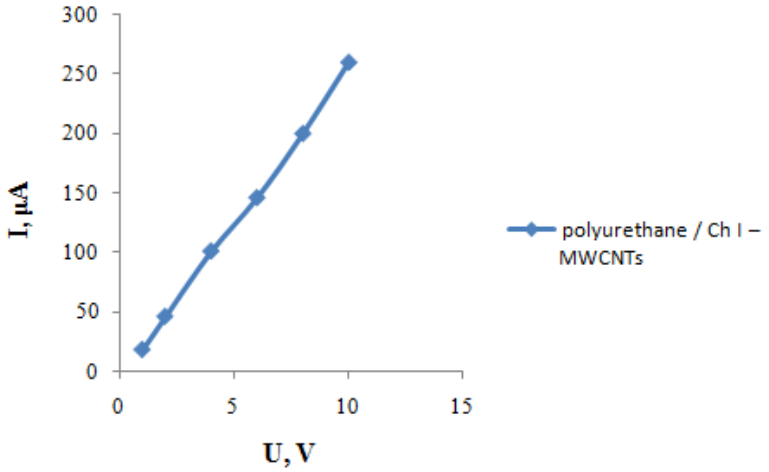

Fig. 14. Volt – ampere characteristics of polymeric nanocomposites based on polyurethane / Ch I – MWCNTs.

Based on these volt – ampere characteristics by the formulas:
R = U / I, where R is the resistance {Om}, U is the potential difference {V}, I is the current {A};
ρ = R * L / S, where ρ is the resistivity {Om * m}, L is the distance between the measured faces, {m}, S is the cross-sectional area of the sample; {m^2};
σ= 1 / ρ, {S / m}, where σ is the conductivity;
The electrical resistance, specific resistance and conductivity were calculated (Table 1).

Table 1.

Electrical properties of polymer-nanocomposite materials based on volt – ampere measurements.

№ of samples	Sample composition	*R*, Om	*ρ*, Om·m	σ', cm·m^{-1}
1	PY + 5weight. % pristine MWCNTs	49	0,1225	8,2
2	PY + 5 weight. %Ch I – MWCNTs	36625	109,9	$9{,}1\cdot10^{-3}$
3	PY + 5 weight. %Ch + ads. I – MWCNTs	49	0,1225	8,2
4	Silicone+ 5 weight. % pristine MWCNTs	58	0,179	5,57
5	Silicone +5 weight. %Ch I – MWCNTs	221	0,51	1,95
6	Silicone +5 weight. %Ch + ads. I – MWCNTs	1300	3,91	0,26
7	Epoxy + 5 weight. % pristine MWCNTs	42	0,065	15,3
8	Epoxy + 5 weight. %Ch I – MWCNTs	83	0,1	10,0
9	Epoxy + 5 weight. %Ch + ads. I – MWCNTs	9400	30,14	$33{,}1\cdot10^{-3}$

As can be seen from the table, the composite with the highest specific electrical conductivity consists of epoxy resin and pristine multiwalled carbon nanotubes.

From the table also shows the influence of the nature of the polymer matrix on the electrical conductivity of composites. Thus, in 3 samples with the same nanocarbon additive (5 weight.% pristine MWCNTs), during the transition from an epoxy resin matrix to a polyurethane specific conductivity decreased from 15.3 to 8.2 Sm / m, and in the case of a silicone polymer, even lower – 5.57 Sm / m. At the same time, when changing to iodine - containing carbon nanoadditives (№ 2, 5, 8), the nature of the matrix effect is changing. In this case, the composite with an epoxy matrix also has the highest electrical conductivity, but the least is a silicone one.

It also follows from the data of the table 1 that the type of bonding of iodine (chemical, adsorption) with carbon nanotubes also affects the electrical conductivity of the composites. Thus, for composites based on epoxide and silicone in the case of MWCTs functionalized with covalently bound iodine (samples № 8, 5), the electrical conductivity is much higher than when iodine is present in the composite simultaneously in two forms, both chemically bound and adsorbed iodine (samples № 9, 6).For polyurethane composites (samples № 8, 5), the electrical conductivity also differed greatly, but in the case of covalently bound iodine it was lower.

CONCLUSIONS

1. Multi-walled carbon nanotubes were synthesized by using of Aerosol-assisted chemical vapour deposition method (AACVD), their purification and functionalization with iodine-containing groups was carried out. The composition and structure of synthesized and modified CNTs are determined by elemental analysis, IR, SEM and AFM microscopy.

2. Based on the obtained MWCNTs and polymeric materials including polyurethane, silicone and polyepoxide, new CNT / polymer composites have been developed. For the fabricated nanostructured composites, volt–ampere characteristics are recorded and the resistivity and conductivity values are determined. It is shown that the electrophysical properties of nanocomposites based on iodine-modified MWCNTs are influenced both by the type of bonding of iodine with a carbon nanotubes (chemical bonding or physical adsorption) and by the nature of the polymer matrix in the composite.

[1] *S. Nikam et al.* Advanced Nanomaterials and Nanotechnology. Proceedings of the 2nd International Conference on Advanced Nanomaterials and Nanotechnology. 2013. Vol. 143. pp. 2-21.

[2] *G. Lota et al.* Carbon nanotubes and their composites in electrochemical applications. Energy Environ. Sci. 2011. Vol. 4, n. 5, pp. 1592-1605.

[3] *J. Dimitrioset al.* Carbon Nanotubes Enhanced Aerospace Composite Materials. 2013. pp. 155-183.

[4] *D. Untereker, S. Lyu, J. Schley, G. Martinez , L. Lohstreter.* Maximum Conductivity of Packed Nanoparticles and Their Polymer Composites. ACS Appl. Mater. Interfaces. 2009, Vol. 1, n.1, pp. 97-101.

[5] *S. Yengejeh et al.* A Primer on the Geometry of Carbon Nanotubes and Their Modifications. Applied Sciences and Technology. 2015. pp. 17-29.

[6] *K. Grabowski, P. Zbyrad, T. Uhl, W. Staszewski, P. Packo.* Multiscale electro-mechanical modeling of carbon nanotube composites. Computational Materials Science. 2017. 135. pp. 169-180.

[7] *S. Bose, R. Khare, P. Moldenaers.* Assessing the strengths and weaknesses of various types of pre-treatments of carbon nanotubes on the properties of polymer / carbon nanotubes composites: A critical review. Polymer. 2010. pp. 975 -993.

[8] *S. Rana, R. Prasanth, L. Tan.* Handbook of Polymer Nanocomposites. Processing, Performance and Application . 2015. Vol. B. pp. 104-117.

[9] *Swain et al.* Polymer Carbon Nanotube Nanocomposites: A Novel Material Asian J. Chem. 2010. Vol. 22, n.1, pp. 1-15.

[10] *S. Bal, S Samal.* Carbon nanotube reinforced polymer composites – A state of the art. Indian Academy of Sciences. 2007. Vol 30, n. 4, pp. 379-386. Insight into the Broad Field of Polymer Nanocomposites: From Carbon Nanotubes. to Clay Nanoplatelets, via Metal Nanoparticles. E. Stefanescuto. Materials. 2009. Vol. 2. pp. 2095-2153.

[11] *K. Shehzad et al.* Effect of the carbon nanotube size dispersity on the electrical properties and pressure sensing of the polymer composites. J Mater Sci. 2016. 51. pp 11014-11020.

[12] *S. Swain et al.* Polymer Carbon Nanotube Nanocomposites: A Novel Material. Asian Journal of Chemistry. 2010. Vol. 22, № 1, pp 1-15.

[13] *G. Kaur et al.* Electrically conductive polymers and composites for biomedical applications. The Royal Society of Chemistry. 2013. pp. 2-17

[14] *T. Michel et al.* EXAFS investigations of iodine-doped carbon nanotubes. The American Physical Society. 2006. Vol. B, n.73. p. 195419-1-195419-4.

[15] *Z. Qian et al.* Facile synthesis of halogenated multi-walled carbon nanotubes and their unusual photoluminescence. J. Mater. Chem. 2012. Vol. 22, pp. 22113 -22119.

[16] *D. Janas et al.* Iodine monochloride as a powerful enhancer of electrical conductivity of carbon nanotube wires. Carbon. 2014. Vol 73, pp. 225-233.

[17] *N. Zainal.* Preparation and Characterization of Iodine-doped Multi-wall Carbon Nanotubes. AIP Conference Proceedings 1017. 2008. Vol. 159, pp. 159 -163. doi: 10.1063/1.2940618.

[18] *W. Zhou et al.* Raman scattering and thermogravimetric analysis of iodine-doped multiwall carbon nanotubes. Applied Physics Letters. 2002. Vol. 80, n.4, pp. 2553-2555.

[19] *T. Michel et al.* Structural selective charge transfer in iodine-doped carbon nanotubes. Journal of

Physics and Chemistry of Solids.Vol. 67. 2006, pp. 1190-1192.

[20] *Fan L-n, Xu X-c.* A stable iodine-doped multi-walled carbon nanotube-polypyrrole composite with improved electrical property. Composites Science and Technology. 2015. doi: 10.1016/j.compscitech.2015.09.014.

[21] *S. Abdullayeva et al.* Characterization of high quality carbon nanotubes synthesized via Aerosol - CVD. Journal of Advances in Physics. 2015. Vol .11, n.4, pp 3229-3237.

[22] *S. Abdullayeva.* Carbon Nanotubes Dispersion in Polymers by Two-Factor Mechanical Method. Advances in Materials Physics and Chemistry. 2016. Vol. 6. pp 29 -304. DOI: 10.4236/ampc.2016.611028.

Recevied: 05.09.2017

ISSN 1028-8546

2017, Vol. XXIII, № 3
Section: En

CONTENTS